University of Pennsylvania
ScholarlyCommons

Publicly Accessible Penn Dissertations

1-1-2013

Modulating Nanoparticle Film Assembly Using Amphiphiles

Kwadwo Tettey
University of Pennsylvania, kwadwo.tettey@gmail.com

Follow this and additional works at: http://repository.upenn.edu/edissertations

 Part of the Chemical Engineering Commons

Recommended Citation
Tettey, Kwadwo, "Modulating Nanoparticle Film Assembly Using Amphiphiles" (2013). *Publicly Accessible Penn Dissertations*. 809.
http://repository.upenn.edu/edissertations/809

This paper is posted at ScholarlyCommons. http://repository.upenn.edu/edissertations/809
For more information, please contact libraryrepository@pobox.upenn.edu.

Modulating Nanoparticle Film Assembly Using Amphiphiles

Abstract
Nanocomposite thin films comprised of nanoparticles have shown great promise for use in electronics, photonics, biomedical as well as energy storage and conversion devices. One versatile method for fabricating such thin films is layer-by-layer (LbL) assembly, a process that involves sequential deposition of oppositely charged species to create conformal thin films. The advantage of LbL assembly lies in the fact that the properties and structure of films can be tuned by varying assembly conditions such as pH and ionic strength. Furthermore, a variety of nanomaterials with useful properties can be incorporated within LbL assembled thin films. Despite these advantages, there are a few limitations to using LbL assembly to fabricate nanoparticle films: (1) Favorable film growth of all-nanoparticle LbL assembly in aqueous phase occurs within a narrow processing window thus limiting the versatility of LbL assembly. (2) nanoparticle LbL assembly has generally been limited to aqueous phase due to the ease of charging nanomaterials in water. (3) The fabrication of nanoparticle films via LbL assembly is slow and typically takes several hours to complete. In this thesis, amphiphiles will be used to address these three limitations of nanoparticle LbL assembly. The first limitation is addressed by using a small amphiphilic molecule, hexylamine to broaden the narrow nanoparticle LbL assembly window. In addition, an array of experimental techniques is used to reveal the mechanism leading to a broad processing window. It will be demonstrated that the second limitation of nanoparticle LbL assembly to aqueous phase can be overcome by using a surfactant Aerosol-OT (AOT) to charge stabilize particles in toluene for non-polar LbL assembly. Furthermore, the effect of the surface chemistry of particles and dispersion moisture content on the charge of particles in non-polar media is probed along with the role of relative humidity on the LbL assembly process in non-polar media. Lastly, electrophoretic deposition (EPD) of surfactant-charged particles in a non-polar solvent is used to rapidly assemble nanocomposite films, thus overcoming the third limitation of nanoparticle LbL assembly.

Degree Type
Dissertation

Degree Name
Doctor of Philosophy (PhD)

Graduate Group
Chemical and Biomolecular Engineering

First Advisor
Daeyeon Lee

Subject Categories
Chemical Engineering

This dissertation is available at ScholarlyCommons: http://repository.upenn.edu/edissertations/809

MODULATING NANOPARTICLE FILM ASSEMBLY USING AMPHIPHILES

Kwadwo E. Tettey

A DISSERTATION

in

Chemical and Biomolecular Engineering

Presented to the Faculties of the University of Pennsylvania

in

Partial Fulfillment of the Requirements for the

Degree of Doctor of Philosophy

2013

Supervisor of Dissertation

_____

Daeyeon Lee, Associate Professor, Chemical and Biomolecular Engineering

Graduate Group Chairperson

_____

Raymond Gorte, Professor, Chemical and Biomolecular Engineering

Dissertation Committee

John C. Crocker, Associate Professor, Chemical and Biomolecular Engineering

Christopher B. Murray, Professor, Chemistry and Materials Science and Engineering

Karen I. Winey, Professor, Materials Science and Engineering, and Chemical and Biomolecular Engineering

MODULATING NANOPARTICLE FILM ASSEMBLY USING AMPHIPHILES

COPYRIGHT

2013

Kwadwo E. Tettey

To my parents

Acknowledgements

The completion of this thesis would have been impossible without the support of numerous individuals to whom I am very grateful for. Firstly, I would like to thank my advisor Professor Daeyeon Lee for all his guidance over the past five years. I consider it a privilege to have been his first Ph.D. student. His enthusiasm and dedication for science rubbed off over the years and has constantly kept me motivated. I also appreciate his willingness to spend time discussing my research, as these discussions have certainly helped me to sharpen my scientific acumen.

I would also like to thank my thesis committee members Professor Crocker, Professor Murray and Professor Winey. I appreciate Professor Murray and Winey's generosity with using their lab equipment, which have been very helpful for my research.

I am also very grateful for all the students I have worked with in the Lee group over the years, Ankit Kumar, David Kim, Diya Li, Fuquan Tu, Iris Yi, Jacob Prosser, Kyoung Wan Kim, Majemite Dafinone, Sarah Hann, Teresa Brugarolas and Weifeng Wang. I especially thank Teresa, my "sister from another mister", for her friendship, energy and continuous support over the years. I am very grateful for the post–docs in our group Bum Jun Park, Lei Zhang, Myung Han Lee and Sang–Wook Lee who have helped me to resolve difficulties encountered in my research on numerous occasions. I have particularly enjoyed supervising some exceptional undergraduate students, Anjali Khetan,

Jeanne Ho, Michael Yee, Peter Forzaglia and Rohan Nagrath. These students have played an instrumental role in accelerating the pace of my research.

I would also like to express my gratitude to my SEAS companions, Rainer Kungas, Chinwendu Enyioha, Philip Asare, Nisha Sosale, Lawrence Adaijanto and Lu Yao for spurring me on during the course of my program. In addition, I appreciate the friendships formed with the wonderful Graduate Associates and undergraduate residents at the W.E.B Du Bois College House and I am very thankful for the free room and board offered over the past four years.

I thank my brothers and sisters at Grace Covenant Church (GCC), University City for their spiritual support and growing my faith in Christ. It has been a privilege partnering up with them for the gospel and I truly appreciate their unconditional love and prayers.

Finally, I want to thank my parents for their patience and for encouraging me to pursue my dreams. I am extremely thankful for all of their support since beginning my studies here in the USA and for always believing in me. My siblings and in–laws have been exceptional in checking up on me and for which I am very thankful.

Funding was provided by Penn MRSEC, Nano/Bio Interface Center through the National Science Foundation NSEC and National Science Foundation CAREER Award.

ABSTRACT

MODULATING NANOPARTICLE FILM ASSEMBLY USING AMPHIPHILES

Kwadwo E. Tettey

Daeyeon Lee

Nanocomposite thin films comprised of nanoparticles have shown great promise for use in electronics, photonics, biomedical as well as energy storage and conversion devices. One versatile method for fabricating such thin films is layer–by–layer (LbL) assembly, a process that involves sequential deposition of oppositely charged species to create conformal thin films. The advantage of LbL assembly lies in the fact that the properties and structure of films can be tuned by varying assembly conditions such as pH and ionic strength. Furthermore, a variety of nanomaterials with useful properties can be incorporated within LbL assembled thin films. Despite these advantages, there are a few limitations to using LbL assembly to fabricate nanoparticle films: (1) Favorable film growth of all–nanoparticle LbL assembly in aqueous phase occurs within a narrow processing window thus limiting the versatility of LbL assembly. (2) nanoparticle LbL assembly has generally been limited to aqueous phase due to the ease of charging nanomaterials in water. (3) The fabrication of nanoparticle films via LbL assembly is slow and typically takes several hours to complete. In this thesis, amphiphiles will be used to address these three limitations of nanoparticle LbL assembly. The first limitation is addressed by using a small amphiphilic molecule, hexylamine to broaden the narrow nanoparticle LbL assembly window. In addition, an array of experimental techniques is

used to reveal the mechanism leading to a broad processing window. It will be demonstrated that the second limitation of nanoparticle LbL assembly to aqueous phase can be overcome by using a surfactant Aerosol–OT (AOT) to charge stabilize particles in toluene for non–polar LbL assembly. Furthermore, the effect of the surface chemistry of particles and dispersion moisture content on the charge of particles in non–polar media is probed along with the role of relative humidity on the LbL assembly process in non–polar media. Lastly, electrophoretic deposition (EPD) of surfactant–charged particles in a non–polar solvent is used to rapidly assemble nanocomposite films, thus overcoming the third limitation of nanoparticle LbL assembly.

Table of Contents

List of Tables

List of Figures

Chapter 1. Introduction

1.1 Background

1.1.1 Thin Films

Thin films are layers, a few nanometers to several microns in thickness, composed of one or more materials such as nanoparticles and polymers. Recently, nanocomposite thin films have gained considerable attention since the selected nanomaterials often have distinct properties, giving rise to functional films useful for numerous applications such as advanced electronics,[1] catalysis,[2] and life sciences.[3] A few examples of common techniques used to fabricate thin films include drop–casting, doctor–blading, electrophoretic deposition, the Langmuir–Blodgett technique and spin–casting. Although these methods are well utilized, their use in fabricating nanocomposite thin films is nevertheless limited. For example, over the last two decades, chemists and materials scientists have synthesized an array of nanoparticles with unique properties, but the use of the aforementioned techniques for fabricating nanocomposite films comprised of two or more nanoparticles has been limited. Furthermore, in most applications, the structure and composition of nanocomposite thin films influences their properties and performance; however, precise control over the structure and composition is difficult with these assembly methods. Lastly, these fabrication methods are often not scalable over large areas (~ m^2), severely limiting the commercial adaptation of these thin film assembly methods. One method that overcomes many of these challenges is layer–by–layer (LbL) assembly, which will be discussed in the next section of this chapter.

1.1.2 Layer–by–layer (LbL) Assembly

Layer–by–layer (LbL) assembly is a versatile technique for creating nanocomposite thin films. In the LbL assembly method, adsorption of materials containing complementary charged or functional groups is used to build up films.[4] For example, electrostatic attraction between two oppositely charged polymers or nanoparticles, or between a charged nanoparticle and oppositely charged polymer can be used to assemble nanocomposite films as summarized in Figure 1.1.

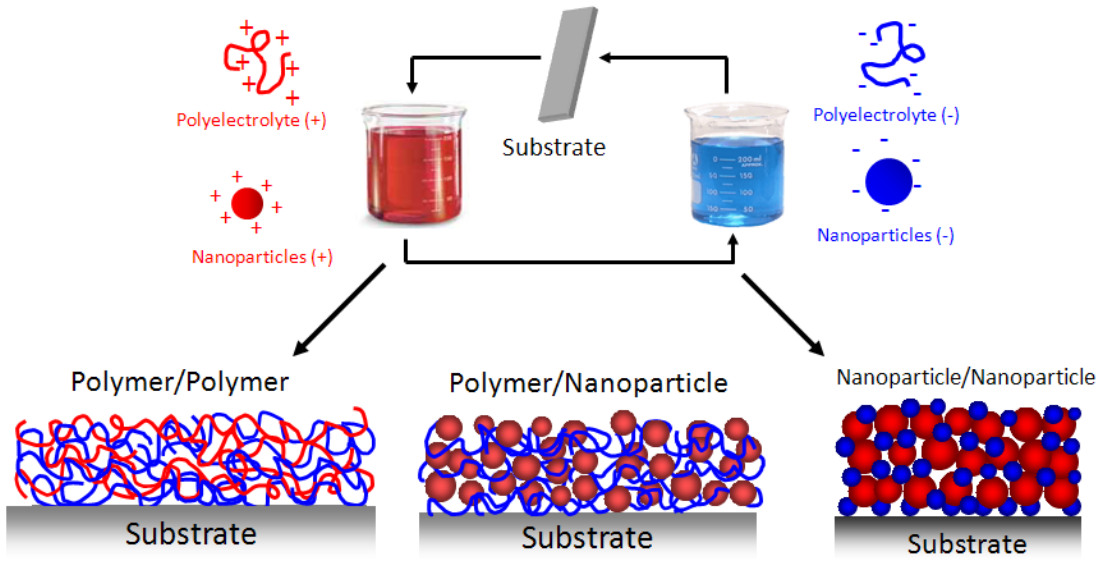

Figure 1.1. Schematic showing layer–by–layer assembly of oppositely charged polymers and nanoparticles.

During electrostatic LbL assembly, the adsorption of charged material followed by charge neutralization, and resaturation eventually leads to surface charge reversal.[5] Alternation of the surface charge is therefore used to continuously deposit positively and negatively charged material, thus offering control over the layering sequence and

thickness of films.[5] Planar supports such as glass slides are typically used for LbL assembly since they are charged in water. However, the versatility of LbL assembly lies in the fact that conformal thin films can be fabricated on various substrates such as porous supports, colloids and even cells.[6-16] Furthermore, a broad range of charged nanoparticles, polymers and even biomolecules can be incorporated into LbL assembled thin films,[12, 17-23] yielding films with unique sensing,[15, 24] mechanical,[25, 26] optical,[27,28] wetting,[22, 29 30, 31] and catalytic[14, 32] properties. The nanomaterial concentration, size, type, and even surface charge often need to be optimized to ensure the growth of LbL assembled films, therefore, variation of these assembly parameters can be used to tune properties such as structure and composition of thin films.[12]

Iler in 1966 demonstrated the multilayer assembly of oppositely charged colloidal particles to yield particle/particle films,[33] however, this comprehensive study did not receive considerable attention over the next 25 years. In the early 1990s', Decher and co–workers demonstrated the multi–layer assembly of polyelectrolytes, effectively establishing the LbL assembly field. [34-36] Since then, researchers primarily focused on polymer/polymer and polymer/nanoparticle LbL assembly systems, but Lee *et. al.* in 2006 re–examined Iler's early work, and demonstrated LbL assembly of oppositely charged TiO_2 and SiO_2 nanoparticles for all–nanoparticle thin films.[22] These multi–functional films were found to have superhydrophilic, anti–reflection and self–cleaning properties, making them potentially useful for numerous industrial and consumer applications involving transparent coatings on windows and lenses.[22] Since then, nanoparticle/nanoparticle LbL assembly has been used to create all–nanoparticle films

with useful properties ranging from flame retardant coatings to energy storage and conversion devices.[37-39]

1.2 Motivation

Despite the numerous advantages associated with LbL assembly and the significant progress made in using LbL assembly to fabricate all–nanoparticle thin films, a few major challenges limits the versatility of this method for nanoparticle thin film assembly. These limitations are outlined as follows:

1.2.1 Limitation of Nanoparticle LbL Assembly to a Narrow Processing Window

In the study by Lee *et. al.*, the growth behavior of TiO_2/SiO_2 nanoparticle LbL assembled films was found to sensitively depend on the pH of each nanoparticle suspension.[40] Specifically, favorable film growth (i.e. the bilayer thickness becomes commensurate with the size of the two nanoparticles – TiO_2 7 nm and SiO_2 22 nm) only occurred within a narrow pH range (TiO_2 and pH 4.0 and SiO_2 at pH 3.0). Outside this pH window, the average bilayer thickness was found to be typically less than 10 nm as shown below in Figure 1.2.

The origin of the narrow processing window is attributed to incomplete charge reversal of the LbL assembled film after deposition of each nanoparticle layer. This effect is closely related to the charge of adsorbing nanoparticles as well as to that of previously adsorbed nanoparticle layers.[40] The narrow processing window acts as a severe limitation

of nanoparticle LbL assembly. As previously mentioned, one of the advantages of LbL assembly is in the ability to use pH to tune the structure and composition of LbL assembled films; however, the narrow processing window of nanoparticle LbL assembly prevents the use of pH for controlling film properties. Furthermore, those nanomaterials or substrates unstable within the processing window cannot be used for LbL assembly.

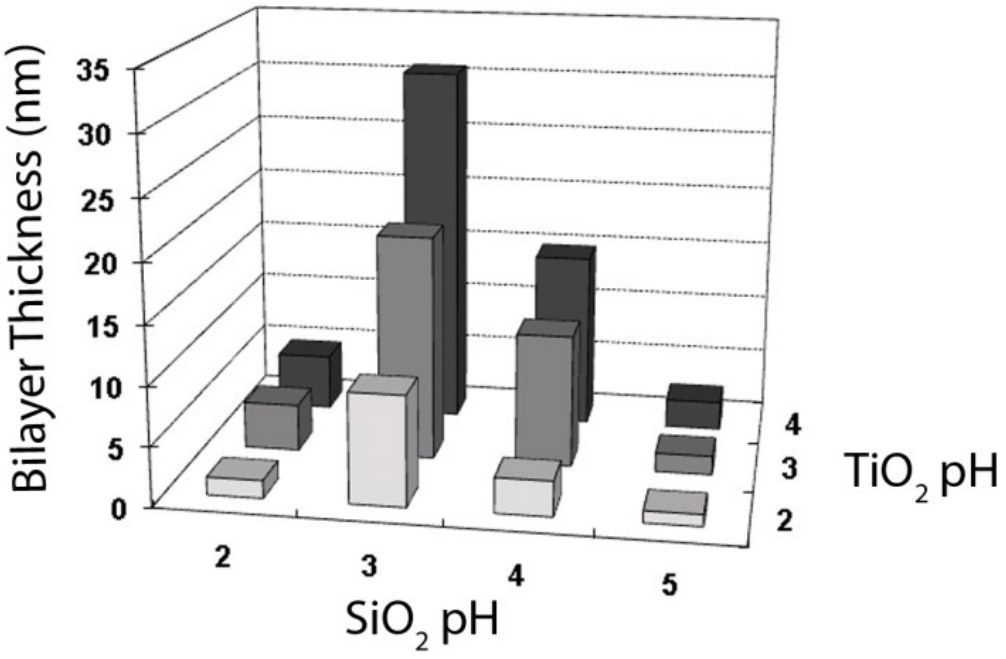

Figure 1.2. pH matrix for TiO_2/SiO_2 thin films composed of 22 nm SiO_2 and 7 nm TiO_2 nanoparticles. Figure reproduced from reference 40.

1.2.2 Limitation of Nanoparticle to Polar Solvents

LbL assembled thin films are typically generated in solvents in which materials readily acquire charge such as water or high polar media (e.g. alcohol[41] and formamides).[42,43] Conversely, LbL assembly in non–polar solvents (i.e. $\varepsilon \sim 2 - 5$)[44] is challenging since

materials dispersed in such solvents do not readily acquire charge. The Bjerrum length (Equation 1–1) describes a characteristic ion–ion separation length at which the thermal energy of the system (k_BT) becomes comparable to the electrostatic energy between two oppositely charged ions. In high polar media such as water (ε ~ 80) at room temperature, the Bjerrum length is 0.7 nm, therefore, a solvation layer around oppositely charged ions is sufficient for charge separation. The result of this is spontaneous charging of particles in polar media. Non–polar media, on the other hand, have much lower dielectric constants (e.g. toluene ε ~ 2.4), resulting in a Bjerrum length of 24 nm. At this length, a 12 nm solvation layer has to form around each ion pair for charge separation to occur. This process is energetically expensive, making spontaneous charging of materials difficult in non–polar media.

$$\lambda_B = \frac{e^2}{4\pi\varepsilon_o\varepsilon k_B T}$$

Equation 1–1. The Bjerrum length in a solvent.

Materials scientists and chemists have recently developed unique nanoparticles such as quantum dots and magnetic nanoparticles with desirable catalytic, optical and electrical properties.[45-48] Incorporating such nanomaterials into nanoparticle thin films would give rise to films with properties for advanced applications. These nanomaterials, however, are typically synthesized and dispersed in non–polar solvents and are therefore not used for LbL assembly since they do not spontaneously acquire charge. Such materials also have poor solubility and stability in water, and making them water–soluble for LbL assembly in aqueous phase would involve additional steps such as surface treatment or ligand

exchange, which, in many cases, is not trivial to accomplish. In addition, these steps are time consuming and can lead to loss of functionality of the nanomaterials. Furthermore, the choice of water as a solvent for LbL assembly limits the use of nanomaterials, which are water sensitive. For example, some polymers and nanoparticles lose their unique properties in water, while substrates could even dissolve in water.[42, 49]

1.2.3 Limitation of Nanoparticle LbL Assembly Rate

A key challenge to the practical application of nanoparticle LbL assembly is in the slow processing speed for assembly of thin films.[50] Conventional nanoparticle LbL assembly is typically performed as a solution–dipping method in which a substrate is immersed in nanoparticle suspensions for ~10–15 minutes after which saturation is reached, followed by ~5 minute immersion in rinse baths.[50] In turn, it can take several hours or days to fabricate nanoparticle films with a targeted thickness. Several approaches such as spin– and spray–assisted deposition have been used to accelerate the LbL assembly process, however, the spray–assisted method is limited by waste and drainage of solutions while the spin–assisted method is limited to small surface areas.[51]

1.3 Thesis Objectives and Outline

1.3.1 Objectives

The main goal of this thesis is to address the three limitations of LbL assembly for creating all–nanoparticle films; in particular, this thesis will use amphiphilic molecules to fulfill the following objectives:

1. Widening the narrow processing window of nanoparticle LbL assembly
2. Demonstrating nanoparticle LbL assembly in non–polar media
3. Rapidly assembling all–nanoparticle films

1.3.2 The Role of Amphiphiles

Amphiphiles, by definition are molecules with two different moieties, a hydrophilic (polar) head group and hydrophobic (non–polar) tail group. The hydrophobic tail groups are typically hydrocarbon chains while a host of functional groups such as alcohols, amines, sulfates, phosphates or carboxylates could form the head group.[52] The polar head group tends to show a strong affinity for polar solvents such as water while the non–polar tail portion prefers oils. The polar head group of conventional amphiphiles can be further classified as charged (ionic) or neutral (non–ionic). Surface–active agents, commonly known as surfactants form a major part of the amphiphile family. These amphiphiles tend to adsorb at various surfaces and interfaces (e.g. oil–water and air–water). Adsorption of surfactants at a surface or interface results in a reduction of the interfacial tension between two fluids or a solid–liquid interface. Many types of surfactants in bulk solution tend to form molecular aggregates termed micelles. Micellization takes place above a

narrow concentration range, the critical micelle concentration (CMC). In polar media such as water, micellization involves the arrangement of the polar head group in contact with the surrounding solvent, while the non–polar tail remains in the micelle center (normal phase micelles). In oil however, this process involves the arrangement of the polar head group in the micelle center, while the non–polar tail extends out (inverse/reverse micelles).

Prior studies have shown that surface modification of nanoparticles using an oppositely charged polymer[53] or a covalently–bonded ligand[54] enhances the growth of polyelectrolyte/nanoparticle LbL assembled films. Low molecular weight amphiphiles have also been shown to facilitate efficient attachment of various metal oxide nanoparticles to air–water[55] and oil–water[56] interfaces. Furthermore, adsorbed amphiphiles have been shown to change surface properties such as charge and hydrophobicity more than standard electrolytes and do not react with solids unlike some elctrolytes.[57] These findings suggest that the adsorption of amphiphiles at the nanoparticle interface can be used as an effective means of changing the surface properties of nanoparticles, thus making the use of amphiphiles beneficial for addressing the three limitations of nanoparticle LbL assembly outlined in the *Objectives* section.

1.3.3 Thesis Outline

Chapter 2 addresses the limitation of nanoparticle LbL assembly to a narrow processing window. It will be shown that a small amphiphilic molecule can be used to broaden the narrow nanoparticle LbL assembly processing window. The TiO_2/SiO_2 nanoparticle LbL

assembly employed by Lee *et. al.* is used as a model system and an array of experimental techniques will be used to reveal the mechanism leading to a broad processing window.

Chapter 3 addresses the limitation of nanoparticle LbL assembly to aqueous phase. In this chapter, it will be demonstrated that nanoparticle LbL assembly can be performed in non–polar solvents. This is achieved by using an anionic amphiphile to charge stabilize common particles in a non–polar solvent. The effect of the surface chemistry of particles and dispersion moisture content on the charge of surfactant–stabilized particles in non–polar solvents is probed in *Chapter 4* while *Chapter 5* examines the role of moisture content (as controlled by relative humidity) on the LbL assembly process in non–polar solvents. It will be shown in *Chapter 6* that this new LbL assembly process in non–polar solvents can be used to create functional photocatalytic and conductive nanocomposite thin films.

Chapter 7 addresses the third limitation of LbL assembly for nanoparticle thin film fabrication by showing that surfactant– and polymer–stabilized particles in non–polar solvents can be used to assemble thin films via electrophoretic deposition (EPD), which is a rapid film fabrication method. This chapter will show that nanoparticle/nanoparticle or even polymer/nanoparticle films can be assembled in relatively short times compared to LbL assembly. In addition, the shortcomings to performing EPD in non–polar solvents will be addressed. Lastly, this dissertation concludes with *Chapter 8*, which gives a brief summary on the new role of the amphiphiles on the assembly of nanoparticle films and gives recommendations for future studies.

Chapter 2. Modulating Layer–by–Layer Assembly of Oppositely Charged Nanoparticles Using a Short Amphiphilic Molecule

Reprinted (adapted) with permission from K. E. Tettey, J. W. C. Ho, D. Lee. Modulating Layer–by–Layer Assembly of Oppositely Charged Nanoparticles Using a Short Amphiphilic Molecule. Journal of Physical Chemistry C, 2011, 115, 6297–6304. Copyright (2011) American Chemical Society.

2.1 Introduction

Recently, LbL assembly has been used to create all–nanoparticle thin film coatings with useful properties.[22, 38, 39, 58] A report by Lee *et al*., for example, describes all–nanoparticle thin films consisting of titania (TiO_2) and silica (SiO_2) nanoparticles that have superhydrophilic, anti–reflection and self–cleaning properties, making them useful for numerous industrial and consumer applications involving transparent windows and lenses.[22] However, the growth of nanoparticle LbL assembled films was found to occur within a narrow processing window in that study, which limits the versatility of LbL assembly for fabricating nanoparticle thin films. The goal of this chapter's study is to widen the processing window for the fabrication of all–nanoparticle LbL assembly thin films. To achieve this goal, the nanoparticles used by Lee *et. al.* (TiO_2/SiO_2) will be used as a model system. The expansion of the processing window will be achieved by introducing a short amphiphilic molecule, hexylamine,[56] into SiO_2 nanoparticle suspensions. Hexylamine (Figure 2.1) has a six–carbon long hydrophobic tail group and a hydrophilic head group which becomes positively charged below its p*K*a of 10.56.[59] The adsorption of short amphiphilic molecules such as hexylamine on charged particles has

been shown to strongly reduce their zeta potential compared to standard electrolytes.[57] The high solubility and high critical micelle concentration of small amphiphiles also make them favorable for surface modification of nanoparticles.[55] It is expected that by modifying SiO_2 nanoparticles with an amphiphilic molecule, hexylamine, the processing window for LbL assembly of all–nanoparticle films could be widened over the same pH range previously reported by Lee *et. al*.[40] This new approach could prove to be a convenient way of generating all–nanoparticle LbL assembly films over a wide processing window.

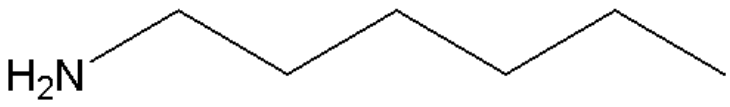

Figure 2.1. Chemical structure of hexylamine

2.2 Experimental Section

2.2.1 Materials

Titania (TiO_2) nanoparticle suspensions (STS–100, 7 nm diameter, 18 wt% solution) was generously provided by Ishihara Sangyo Kaisha, Ltd. Silica (SiO_2) nanoparticle suspensions (Ludox TM–40, 22 nm diameter, 40 wt% solution) is purchased from Sigma–Aldrich. Hexylamine (99% solution), propianic acid and sodium dodecyl sulfate is also purchased from Sigma–Aldrich. Silicon wafers with <100> crystalline orientation is obtained from University Wafer.

2.2.2 TiO_2/SiO_2 Thin Film Assembly

Nanoparticle suspensions of TiO_2 at 0.03 wt % and of SiO_2 at 0.03 wt % are prepared in deionized (DI) water (18 MΩ cm, purified by a Barnstead Nanopure System). Nanoparticle suspensions are titrated to the appropriate pH with 1.0 M HCl or 1.0 M NaOH. Si wafers for LbL are used as received. An HMS dipper (Carl Zeiss) is programmed to expose substrates to TiO_2 nanoparticle suspension for 10 min followed by 2, 1 and 1 min of rinse steps in DI water, then SiO_2 nanoparticle suspension for 10 min followed by 2, 1 and 1 min of rinse steps in DI water. A bilayer represents the LbL film layer that is obtained after one cycle of this procedure. Films with 3, 6, 9 and 12 bilayers are assembled on silicon wafers. The pH of each nanoparticle solution is checked every three bilayers and re–adjusted to the appropriate pH if necessary. Modified nanoparticles are prepared by adding appropriate volume of either hexylamine, propianic acid or sodium dodecyl sulfate to 0.03 wt % nanoparticle suspension followed by stirring and titration to the desired pH.

2.2.3 Characterization of Nanoparticle Suspensions and LbL Thin Films

Particle size and zeta potential measurements are performed with a Delsa Nano C (Beckman Coulter). Film thickness measurements are performed with an Alpha–SE ellipsometer (J.A. Woollam). Measurements are taken at an incidence angle of 70° and at wavelengths from 380 to 900 nm. Zeta potential measurements of LbL films assembled on Si wafers are also performed with the Delsa Nano C (Beckman Coulter). Measurements are made with a flat surface cell in which the LbL film is the upper cell

surface. Standard latex particles are used as probe particles to characterize the surface charge state of the LbL films. The velocity profile of the latex particles undergoing electrophoresis through the cell are fitted to the Mori and Okamoto equation[60] from which the zeta potential of the film is calculated by using the Smoluchowski equation shown below in Equation 2–1.

$$\zeta = \frac{\mu\eta}{\varepsilon_r \varepsilon_o}$$

Equation 2–1. Smoluchowski equation

Here, ζ represents the zeta potential, μ the electrophoretic mobility, η the viscosity of water and $\varepsilon_{\_}$, ε are the dielectric constants of vacuum and water, respectively. For the first sample, a 6.5 bilayer film is assembled at TiO_2 3.0/SiO_2 5.0.* Measurements are made with the probe particles at pH 5.0. The second sample is assembled at TiO_2 3.0/SiO_2 5.0 with 10 mM hexylamine in SiO_2 nanoparticle suspensions used for LbL assembly and with 10 mM hexylamine in the probe particle suspension.

The fate of hexylamine within TiO_2/SiO_2 LbL thin films is probed with Fourier transform infrared (FTIR) spectroscopy. A 5–bilayer film is assembled on a CaF_2 FTIR window (Thorlabs Inc.). FTIR spectra are taken before and after the final rinse steps in DI water. The last three DI water rinse baths are changed to ensure that the rinse baths are

* pH assembly conditions are represented as: pH of TiO_2 nanoparticle suspensions / pH of SiO_2 nanoparticle suspensions. E.g. TiO_2 3.0/ SiO_2 5.0 represents TiO_2 suspensions at pH 3.0 and SiO_2 suspensions at 5.0

not contaminated with hexylamine. A Nicolet 8700 FTIR spectrometer (Thermo Scientific) is used for data acquisition.

2.2.4 QCM Measurements

SiO_2–coated QCM crystals (Q–Sense) are cleaned by immersing in 2 wt % sodium dodecyl sulfate (SDS) solution for 30 min followed by rinsing with DI water, drying with nitrogen, and 10 min oxygen plasma treatment. Frequency shift measurements are performed with an E4 quartz crystal microbalance with dissipation monitoring (QCM–D by Q–Sense). For LbL film assembly on QCM crystals, the frequency shift is monitored in air for ~ 5 min after which DI water is flowed through the QCM–D measuring module. Once a steady baseline in water is obtained, nanoparticle suspensions are flowed into the module for 10 min. Within this time, the adsorption of nanoparticles reaches saturation. Following this, water is flowed for 5 min as the rinse step. Hexylamine adsorption studies are performed by assembling the appropriate number of bilayers on QCM crystals followed by drying the crystal with nitrogen. The crystal is re–loaded into the QCM module and a baseline in water is obtained before introducing the desired concentration of hexylamine into the module. Hexylamine solutions are prepared in DI water with no pH adjustments. A flowrate of 100 μL/min is used for all measurements. All frequency shift data presented are from the third overtone.

2.3 Results and Discussion

2.3.1 Widening the Processing Window of TiO_2/SiO_2 LbL Thin Film Assembly

The growth behavior of LbL films is well known to depend on solution properties such as pH and ionic strength.[12] Prior knowledge of the growth behavior of LbL films is beneficial for selecting assembly conditions that lead to the fabrication of films with properties necessary for the desired applications. As covered in the *Introduction* of this thesis, a previous report by Lee *et al.*, mapped out the growth behavior of TiO_2/SiO_2 all–nanoparticle LbL thin films for different pH conditions as shown in Figure 1.2.[40] In that study, the pH range examined was 2.0 – 4.0 for TiO_2 nanoparticles and 2.0 – 5.0 for SiO_2 nanoparticles. In order to create the pH matrix, the incremental thickness after each cycle of exposing substrates to TiO_2 and SiO_2 nanoparticle suspensions (which is referred to as the average bilayer thickness) was determined for TiO_2/SiO_2 LbL films assembled at each pH condition. Figure 1.2 shows that the growth behavior of LbL nanoparticle films is strongly dependent on the pH of SiO_2 and TiO_2 nanoparticle suspensions. More importantly, favorable film growth (i.e. an average bilayer thickness commensurate with the size of the two nanoparticles) is found to occur within a narrow processing window (pH 3.0 – 4.0 for both SiO_2 and TiO_2 nanoparticle suspensions) and maximum growth occurrs at pH 4.0 and 3.0 for TiO_2 and SiO_2 nanoparticle suspensions, respectively. Outside this range, the average bilayer thickness is much smaller than the size of the two nanoparticles, indicating that dense layers of nanoparticles are not formed during each deposition step. This result suggests that the surface charge of SiO_2 and TiO_2

nanoparticles, which depends on the solution pH, plays a significant role in the assembly of all–nanoparticle thin films.

In the study presented in this chapter, widening the processing window (i.e. significant film growth over a wide pH range), is achieved by adding a small amphiphilic molecule, hexylamine (HA), to SiO_2 nanoparticle suspensions. At pH values below the p*K*a of HA (10.56),[59] the amine group ($–NH_2$) of HA protonates to $–NH_3^+$. This protonation yields a positively charged molecule which interacts with negatively charged SiO_2 nanoparticles, thus, HA is only added to SiO_2 nanoparticle suspensions and not to TiO_2 nanoparticle suspensions. Figure 2.2 shows the change in average bilayer thickness with respect to the concentration of HA in SiO_2 nanoparticle suspensions for various assembly conditions. This result demonstrates that the growth behavior of films can be systematically changed by varying the concentration of HA; specifically, the average bilayer thickness for assembly conditions with small growth (e.g. SiO_2 at pH 5.0) can be increased by raising the concentration of HA present in SiO_2 nanoparticle suspensions (Figure 2.2c). Conversely, the assembly condition for good film growth (e.g. TiO_2 4.0/SiO_2 3.0) shows an initial increase in the average bilayer thickness followed by a decrease in average bilayer thickness as the concentration of HA exceeds 1 mM (Figure 2.2b). The result presented in Figure 2.2 suggests that there is an optimal concentration of HA required to maximize film growth.

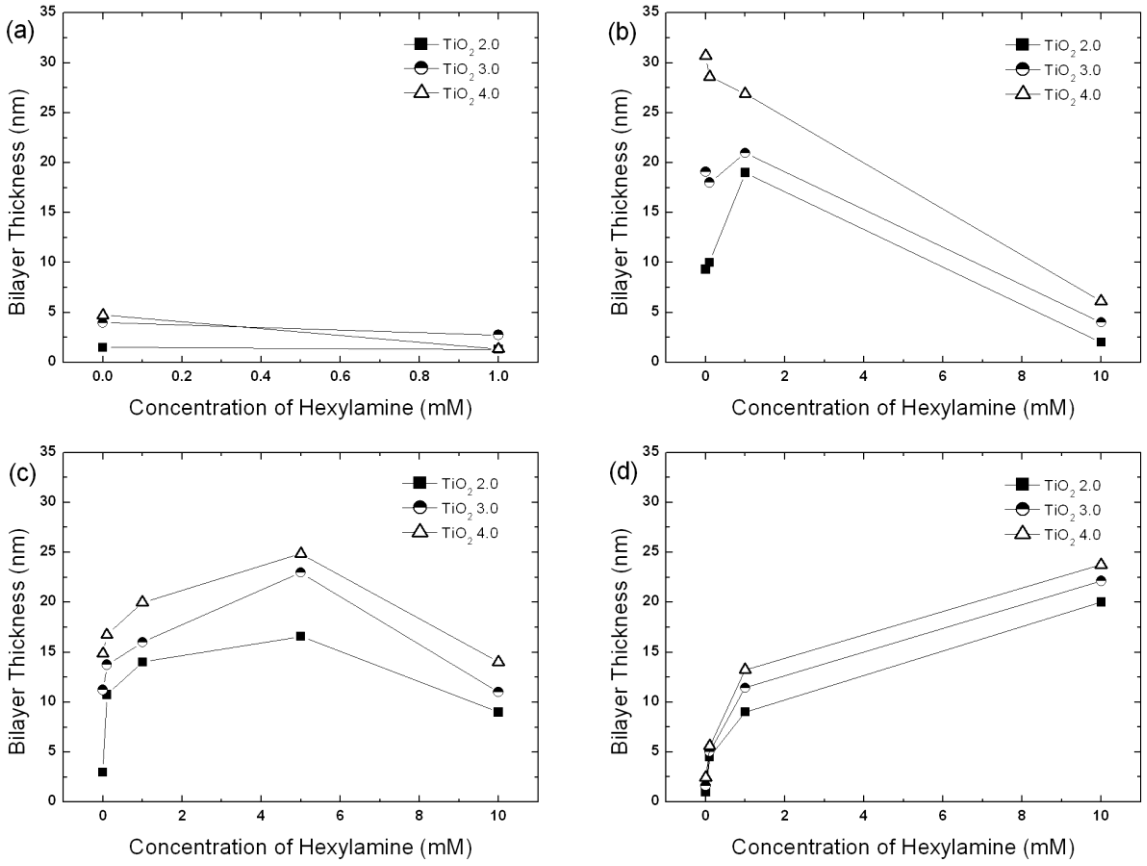

Figure 2.2. Average bilayer thickness for TiO_2/SiO_2 films assembled at different TiO_2 and SiO_2 pH at (a) 2.0, (b) 3.0, (c) 4.0 and (d) 5.0 and with increasing concentrations of hexylamine in SiO_2 nanoparticle suspensions

The pH matrix shown in Figure 2.3a shows the film thickness per bilayer for each assembly condition with 1 mM of hexylamine (HA) present in SiO_2 nanoparticle suspensions. From this result, it is clear that the processing window widens upon adding HA into SiO_2 nanoparticle suspensions. For the majority of assembly conditions, the film thickness per bilayer substantially increases after adding 1 mM HA into the SiO_2 nanoparticle suspension (Figure 2.3a) compared with films assembled without HA in SiO_2 nanoparticle suspensions (Figure 1.2). The all–nanoparticle films assembled with HA in SiO_2 nanoparticle suspensions are uniform and transparent when the assembly pH

of SiO_2 nanoparticles is between 2.0 and 5.0 and that of TiO_2 nanoparticles is between 2.0 and 4.0. Figure 2.3b demonstrates that the film growth for each pH condition can be further enhanced by varying the concentration of HA present in SiO_2 nanoparticle suspensions.

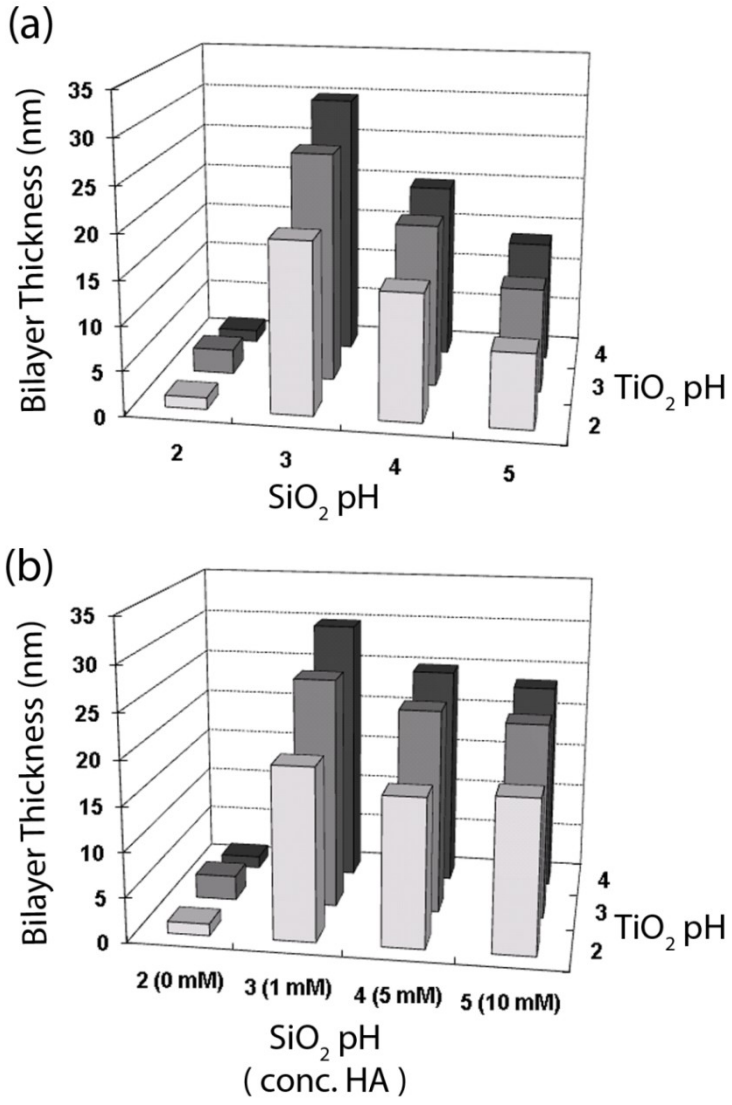

Figure 2.3. pH matrix for TiO_2/SiO_2 LbL thin films with (a) 1 mM hexylamine in SiO_2 nanoparticle suspensions and (b) different concentrations of hexylamine in SiO_2 nanoparticle suspensions.

2.3.2 Zeta Potential and Stability of Nanoparticle Suspensions

To understand the mechanism contributing to the increased growth of TiO_2/SiO_2 LbL films upon adding hexylamine (HA), the effect of HA on the zeta potential and size of SiO_2 nanoparticles is investigated. Figure 2.4a compares the zeta potential of SiO_2 nanoparticles with 1 mM HA in SiO_2 nanoparticle suspensions to the case with no HA in SiO_2 nanoparticle suspension for different pH values. Below pH 2.0, the charge of SiO_2 nanoparticles is near neutral, thus, weak electrostatic interactions between the surface of films and SiO_2 nanoparticles is expected. This likely leads to negligible film growth for this assembly condition as shown in Figure 1.2 and Figure 2.3. From these zeta potential measurements, it is evident that HA suppresses the surface charge of SiO_2 nanoparticles in solution. Under acidic conditions, HA becomes positively charged through protonation – an equilibrium reaction. The adsorption of these positively charged species on negatively charged SiO_2 nanoparticles results in the suppression of the surface charge of SiO_2 nanoparticles as observed in Figure 2.4a. The suppression of SiO_2 nanoparticle charge is also found to depend on the concentration of HA as demonstrated by the case of SiO_2 nanoparticle suspensions at pH 5.0 (Figure 2.4b). As the concentration of HA is increased, more positively charged HA molecules adsorb on the surface of SiO_2 nanoparticles and reduce the surface charge as reflected by the observed decrease in the magnitude of zeta potential (Figure 2.4b). The suppression of surface charge of SiO_2 nanoparticles leads to the formation of dense SiO_2 nanoparticle layers on the surface since the electrostatic repulsion between SiO_2 nanoparticles is diminished. The modification of SiO_2 nanoparticle surface charge in suspension is one of the important

mechanisms by which the growth of TiO_2/SiO_2 LbL film is significantly enhanced. This mechanism will be thoroughly discussed in a subsequent section of Results and Discussion. For high concentrations of HA (50 mM), however, the surface charge of SiO_2 nanoparticles at pH 5.0 is near neutral and at such assembly conditions the average bilayer thickness begins to decrease (Figure 2.2) due to weak electrostatic interactions between SiO_2 nanoparticles and the surface of the LbL film. Similarly, the surface charge of unmodified SiO_2 nanoparticles at pH 3.0 is relatively low so that upon adding 10 mM HA into SiO_2 nanoparticle suspensions, the bilayer thickness drastically drops as observed for a TiO_2 4.0/SiO_2 3.0 assembly condition (Figure 2.2). Previous studies have demonstrated a similar effect in which particle adsorption density was found to depend on the charge density of nanoparticles.[61, 62]

Since HA effectively reduces the surface charge of SiO_2 nanoparticles, the stability of the particles in suspension is of concern. To probe the stability of SiO_2 nanoparticles, the size of nanoparticles is measured using dynamic light scattering (DLS). An increase in measured particle size typically indicates that particles are aggregating in solution. Surprisingly, there is little change in SiO_2 nanoparticle size with pH (Figure 2.5a) in the absence of HA as well as in the presence of 1 mM HA. Furthermore, SiO_2 nanoparticles are stable close to its isoelectric point of pH 2.0. The peculiar behavior of stable SiO_2 nanoparticles near its isoelectric point has previously been observed[63, 64] and is believed to be a result of a hydration layer around SiO_2 nanoparticles which retards the flocculation of the nanoparticles.[65] The size dependence of SiO_2 nanoparticles with increasing concentration of HA is also measured (Figure 2.5b) at pH 3.0 and 5.0. The

results again show that the particle size does not vary significantly with increasing concentration of HA and that SiO_2 nanoparticles remain colloidally stable within the pH and HA concentration ranges tested in this study. The excellent colloidal stability of SiO_2 nanoparticles as well as their reduced surface charge in the presence of HA at different pH conditions leads to the enhanced growth of uniform LbL films.

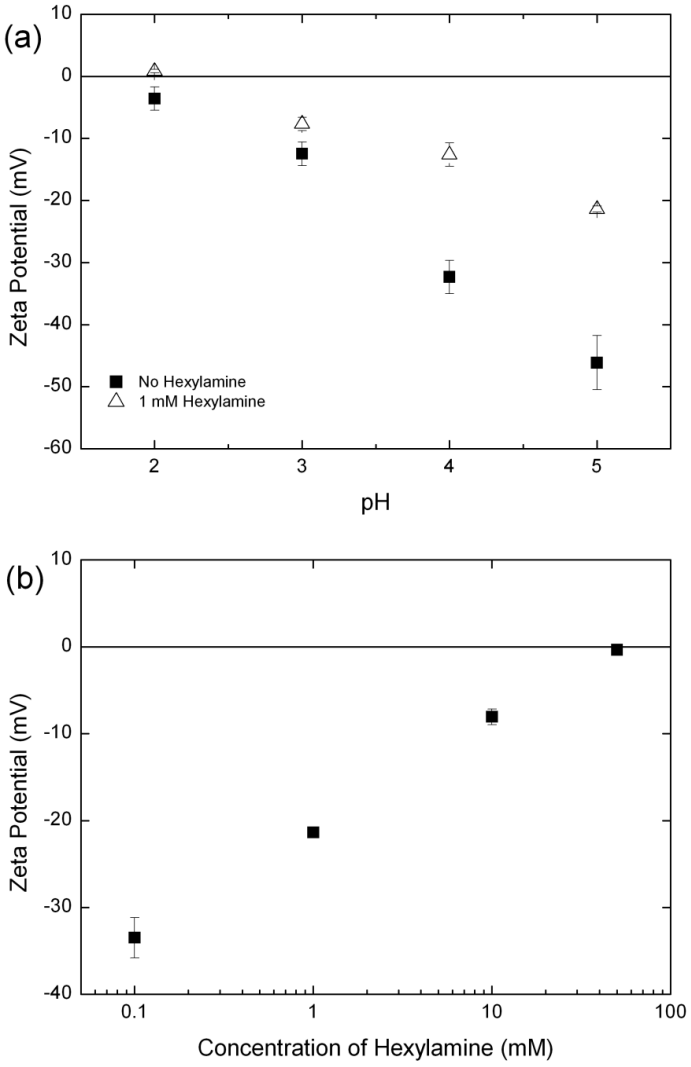

Figure 2.4. Zeta potential of SiO_2 nanoparticles as a function of (a) pH for: no hexylamine and 1 mM hexylamine (b) concentration of hexylamine at pH 5.0. Error bars represent standard deviation of three measurements.

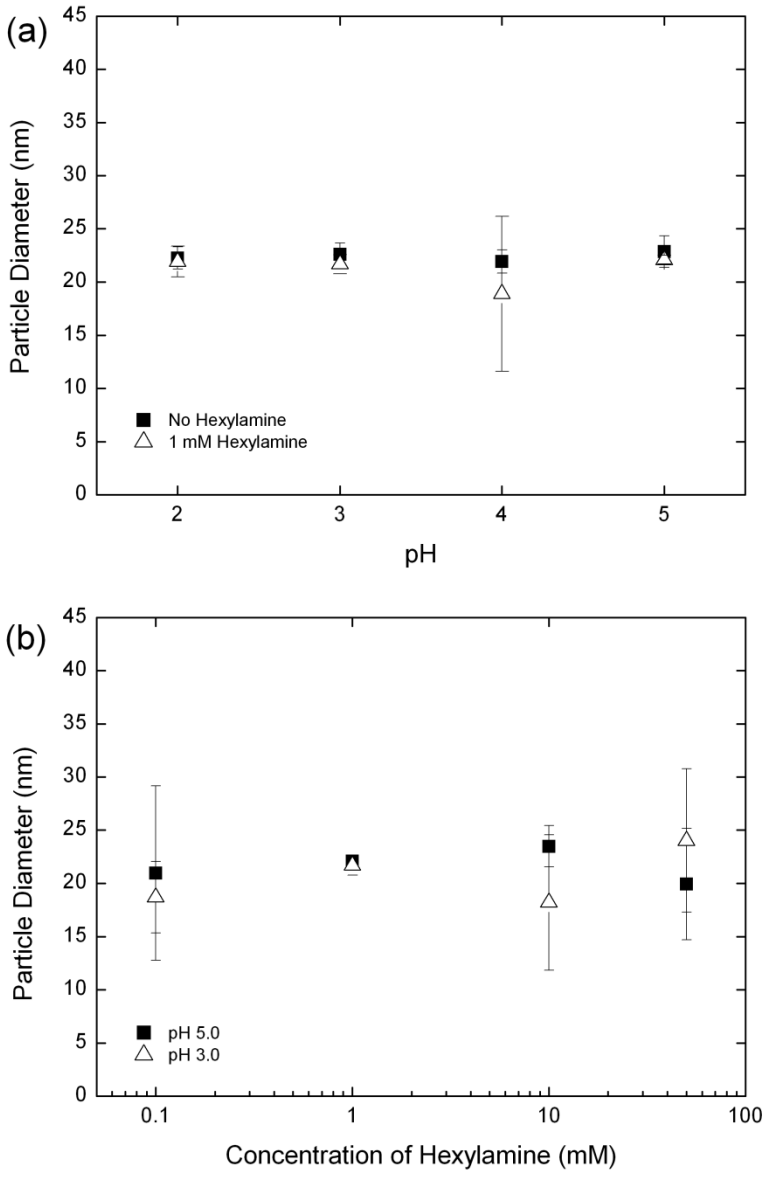

Figure 2.5. Number average particle diameter for SiO_2 nanoparticles as a function of (a) pH with no hexylamine and 1 mM hexylamine, and (b) concentration of hexylamine at pH 3.0 and pH 5.0. Error bars represent standard deviation for three measurements.

Interestingly, the addition of HA or negatively charged amphiphiles in TiO_2 suspension does not enhance the growth behavior of TiO_2/SiO_2 LbL films significantly. The addition of HA to TiO_2 nanoparticle suspensions leads to significant nanoparticle aggregation (Figure 2.6a), thus making these amphiphile modified TiO_2 nanoparticles unsuitable for

film assembly. Furthermore, a short carboxylic acid, propanoic acid, did not suppress the charge of TiO_2 nanoparticles at pH 3.0 (Figure 2.6b) and even an anionic amphiphile, sodium dodecyl sulfate (SDS), added to TiO_2 nanoparticle suspensions did not change the film growth significantly as shown in Table 2.1. For these reasons, this investigation focused on the growth of TiO_2/SiO_2 LbL films upon adding HA to SiO_2 nanoparticle suspensions.

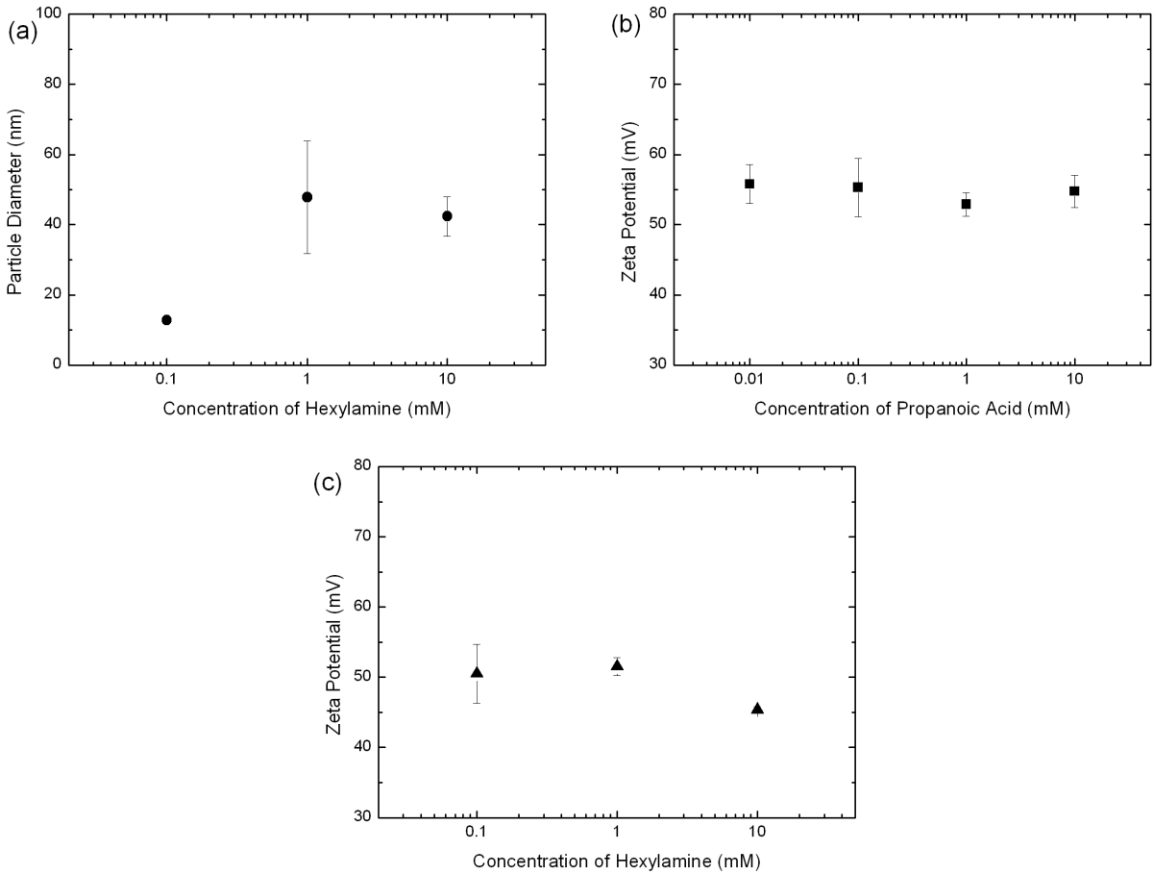

Figure 2.6. (a) Number average particle diameter for TiO_2 nanoparticles as a function of the concentration of hexylamine at pH 3.0. Zeta Potential measurements for TiO_2 nanoparticles with increasing concentrations of (b) propianic acid and (c) hexylamine at pH 3.0. The zeta potential of unmodified TiO_2 nanoparticles is 52.1 ± 4 mV. Error bars represent standard deviations for three measurements.

Table 2.1. Comparison of thickness measurements for TiO_2/SiO_2 LbL films assembled with amphiphile modified nanoparticles to films assembled without amphiphile in nanoparticle suspensions.

	Film thickness (nm) for TiO_2 3.0/SiO_2 5.0 assembly condition		
Number of bilayers	No amphiphile in suspensions	1 mM Hexylamine in SiO_2 suspension	1 mM Sodium Dodecyl Sulfate in TiO_2 suspension
3	21.9± 0.1	37.6 ± 0.7	18.5 ± 0.3
12	46.1 ± 3.3	143.8 ± 0.1	49.9 ± 0.6

2.3.3 LbL Thin Film Assembly Monitored by Quartz Crystal Microbalance

To confirm the significantly denser adsorption of SiO_2 nanoparticles upon adding HA, quartz crystal microbalance (QCM) measurements are taken to monitor the real time deposition of nanoparticles during LbL assembly. Figure 2.7a shows that for TiO_2 3.0/SiO_2 5.0 assembly condition without HA, the film growth is significantly smaller than TiO_2 3.0/SiO_2 3.0 assembly condition without HA. This result agrees with the observation made in the pH matrix (Figure 1.2) in which negligible film growth occurred for TiO_2 3.0/SiO_2 5.0. The frequency shifts, however, show that there is a significant increase in the growth of TiO_2 3.0/SiO_2 5.0 films upon adding 10 mM HA into SiO_2 nanoparticle suspensions. This result also agrees with the observation made in Figure 2.2 where film growth is significantly increased upon adding 10 mM HA for this same assembly condition. Figure 2.7b and Figure 2.7c compares the frequency shifts after deposition of SiO_2 and TiO_2 nanoparticles, respectively. For SiO_2 nanoparticles, the magnitude of the frequency shift is seen to increase 6 – 10 fold in the presence of 10 mM

HA. This result confirms that when 10 mM HA is present in SiO_2 nanoparticle suspensions, the suppression of charge indeed leads to increased deposition of SiO_2 nanoparticles on the surface, thus forming thicker LbL films. Conversely, the changes seen in the frequency shifts during the deposition of TiO_2 nanoparticles is less pronounced for each of the three assembly conditions, thus suggesting that the suppression of SiO_2 nanoparticle charge does not significantly affect the deposition of TiO_2 nanoparticles.

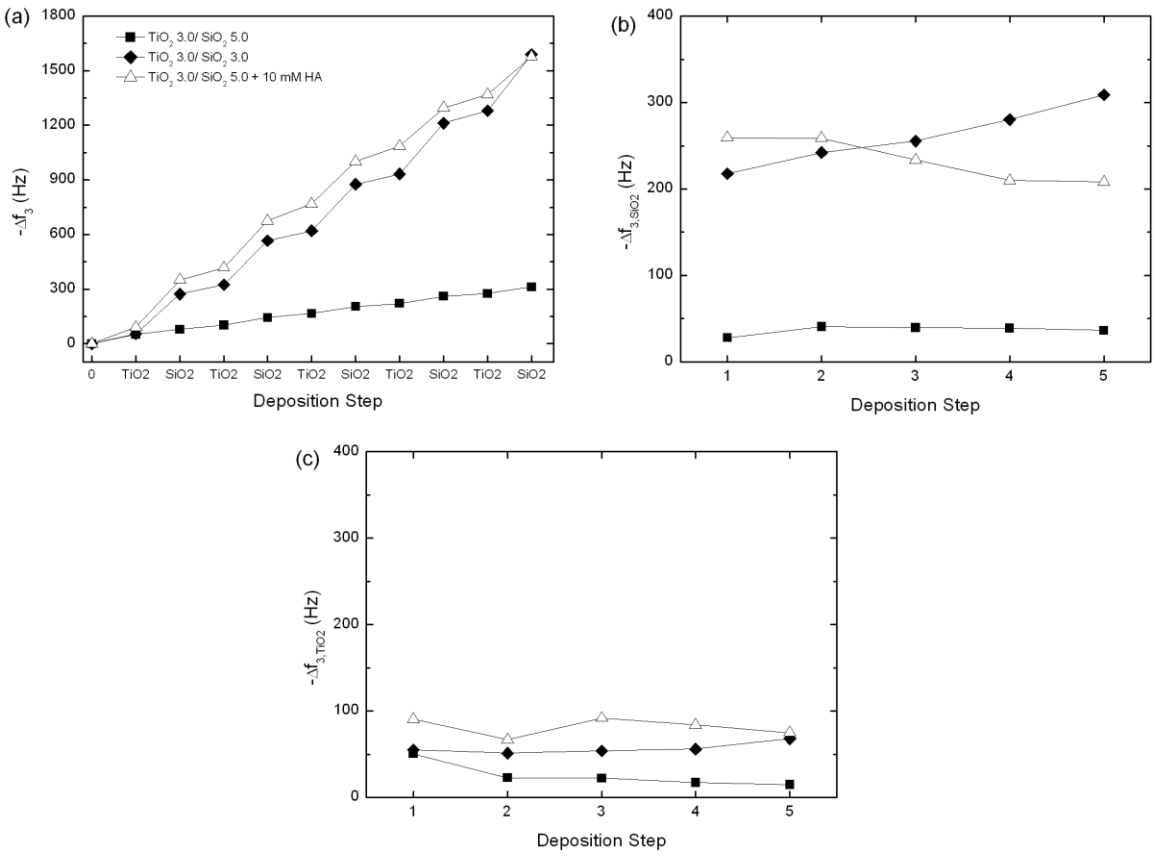

Figure 2.7. (a) QCM frequency shifts for LbL deposition of TiO_2/SiO_2 under different assembly conditions. Frequency shifts after deposition of (b) SiO_2 nanoparticles and (c) TiO_2 nanoparticles for different assembly conditions.

2.3.4 Zeta Potential of TiO_2/SiO_2 LbL Thin Films

In the previous report by Lee *et al.*, the surface charge of the outermost LbL film layer was believed to contribute to the narrow processing window of LbL films.[40] More specifically, incomplete charge reversal of the film surface after depositing each nanoparticle layer was found to lead to little adsorption of nanoparticles in the subsequent deposition step, thus, yielding negligible growth of TiO_2/SiO_2 LbL films. In addition to influencing the surface charge of suspended SiO_2 nanoparticles, it is plausible that hexylamine (HA) influences the charge of previously adsorbed nanoparticles in the film, thus leading to an increase in bilayer thicknesses. To understand the role of HA during film assembly, the zeta potential of TiO_2/SiO_2 LbL films in the presence of HA is characterized. Zeta potential measurements (Figure 2.8) are made for 6.5 bilayer films assembled at TiO_2 3.0/SiO_2 5.0. This pH combination represents an assembly condition that yields negligible incremental film thickness without added HA (average bilayer thickness is 1.6 nm) as shown in Figure 1.2. The average bilayer thickness, however, drastically increases to 21.9 nm upon adding 10 mM HA to SiO_2 nanoparticle suspensions as seen in Figure 2.2 and Figure 2.3b.

A 6.5 bilayer film in pH 5.0 solution represents a state in which the outermost LbL layer consist of TiO_2 nanoparticles with SiO_2 nanoparticles in suspension (at pH 5.0) adsorbing onto the TiO_2 nanoparticle layer. The pH of the testing solution during zeta–potential measurement is adjusted to 5.0 to mimic such condition. For films assembled with no HA, the zeta potential of the film surface is negative which confirms the incomplete charge reversal after depositing TiO_2 nanoparticles.[40] At pH 3.0 (during the

TiO_2 nanoparticle adsorption step) SiO_2 nanoparticles on the surface are weakly charged, thus, a small number of TiO_2 nanoparticles are needed to compensate the SiO_2 nanoparticle layer. When the TiO_2 nanoparticle coated film is transferred to pH 5.0 solution, the SiO_2 nanoparticle layer beneath the outermost TiO_2 nanoparticles becomes strongly negatively charged (see Figure 2.4a for the dependence of the zeta potential of SiO_2 nanoparticles on pH). As a result of this, the net surface charge becomes negative (Figure 2.8 and Figure 2.9a) at pH 5.0 despite the fact that the outermost layer consist of positively charged TiO_2 nanoparticles.[40] The net negative surface charge leads to negligible adsorption of similarly charged SiO_2 nanoparticles as they approach the surface from solution. This negligible adsorption of SiO_2 nanoparticles most likely explains the small film growth observed at this assembly condition.

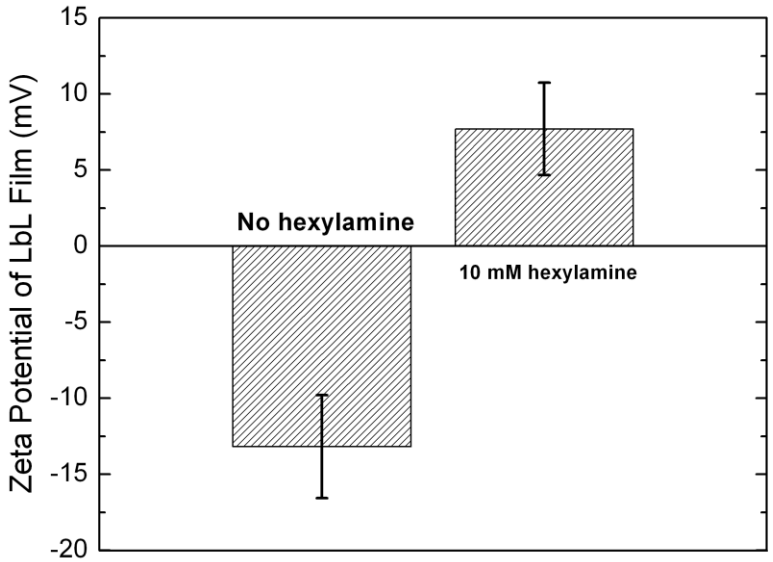

Figure 2.8. Zeta potential of 6.5 bilayer TiO_2/SiO_2 LbL thin film assembled at TiO_2 3.0/SiO_2 5.0 with no HA in SiO_2 nanoparticle suspensions or testing solution (left bar) and with 10 mM HA in SiO_2 nanoparticle suspensions and testing solution (right bar). Error bars represent standard deviation for three measurements.

Conversely, the TiO_2 3.0/SiO_2 5.0 6.5 bilayer film assembled with 10 mM HA in SiO_2 nanoparticle suspensions is found to have a positive surface zeta potential. This charge inversion from negative to positive in the presence of HA is most likely induced by the adsorption of HA on SiO_2 nanoparticles within the previously formed TiO_2/SiO_2 LbL layers. The adsorbed HA suppresses the negative charge of SiO_2 nanoparticles within the film and thus, the net surface charge becomes positive (Figure 2.8 and Figure 2.9b). Since there is now charge inversion of the surface, more SiO_2 nanoparticles can adsorb onto the surface, thus forming thicker TiO_2/SiO_2 films in agreement with the results seen in Figure 2.3a and Figure 2.3b. Fourier transform infrared (FTIR) spectra (Figure 2.10) also confirm that HA adsorbs into TiO_2/SiO_2 LbL film and show that HA remains within the film even after rinsing.

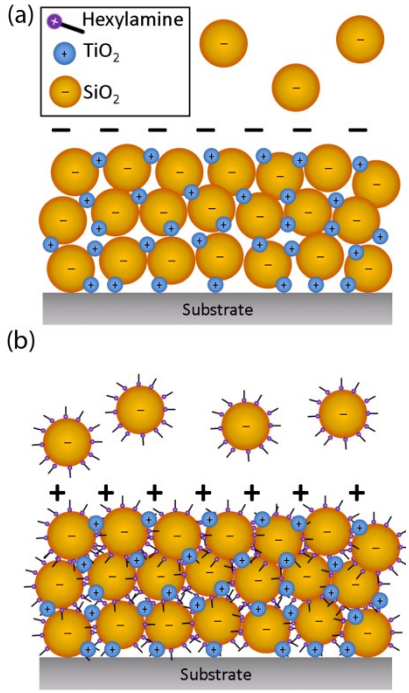

Figure 2.9. Representation of LbL assembly of TiO_2/SiO_2 films with (a) no HA present in SiO_2 nanoparticle suspensions yielding a net negative film surface charge and (b) HA in SiO_2 nanoparticle suspensions yielding a net positive film surface charge.

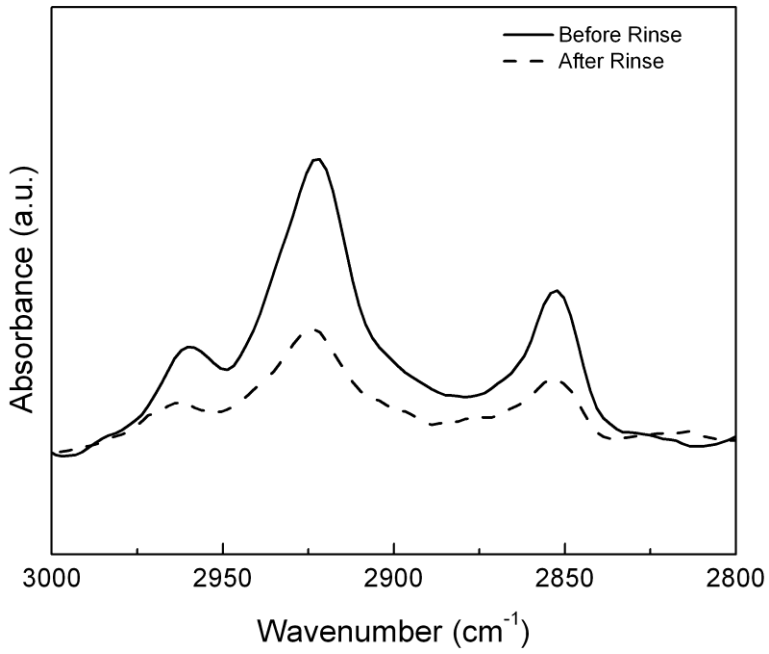

Figure 2.10. FTIR spectra of 5 bilayer TiO_2/SiO_2 LbL film assembled at TiO_2 3.0/SiO_2 5.0 with 10 mM HA in SiO_2 nanoparticle suspensions before rinse (red line) and after rinse (black line). Peaks characteristic to the alkane chains of hexylamine are observed before and after rinsing.

The adsorption of HA onto SiO_2 nanoparticles within the films is probed with QCM. Figure 2.11a shows the frequency shifts as a function of time after introducing 10 mM HA onto a blank QCM crystal with SiO_2 surface as well as crystals with 2, 4 and 6 bilayers of TiO_2/SiO_2 LbL film atop SiO_2 QCM crystals. Although HA interacts with the bare crystal, the increasing frequency shifts with the number of deposited bilayers suggests that HA also interacts with SiO_2 nanoparticles within the LbL film.[†] The frequency shifts scale with the number of deposited bilayers, suggesting that HA is interacting with SiO_2 nanoparticles throughout the film as opposed to the outermost SiO_2

[†] Negligible change in the zeta potential of TiO_2 nanoparticles with increasing concentratuon of hexylamine (Figure 2.6c) suggest that HA does not interact with the surface of TiO_2 nanoparticles. From this result, it can be inferred that HA does not interact with TiO_2 nanoparticles within the LbL film formed on the crystal so that the observed frequency shifts are only from the adsorption of HA onto SiO_2 nanoparticles within the film.

nanoparticle layer. The frequency shifts upon introducing increasing concentrations of HA onto a 6–bilayer film are also compared as shown in Figure 2.11b. This result suggests that as the concentration is increased, more HA adsorbs onto SiO_2 nanoparticles within the film, thus leading to the observed increase in frequency shifts.

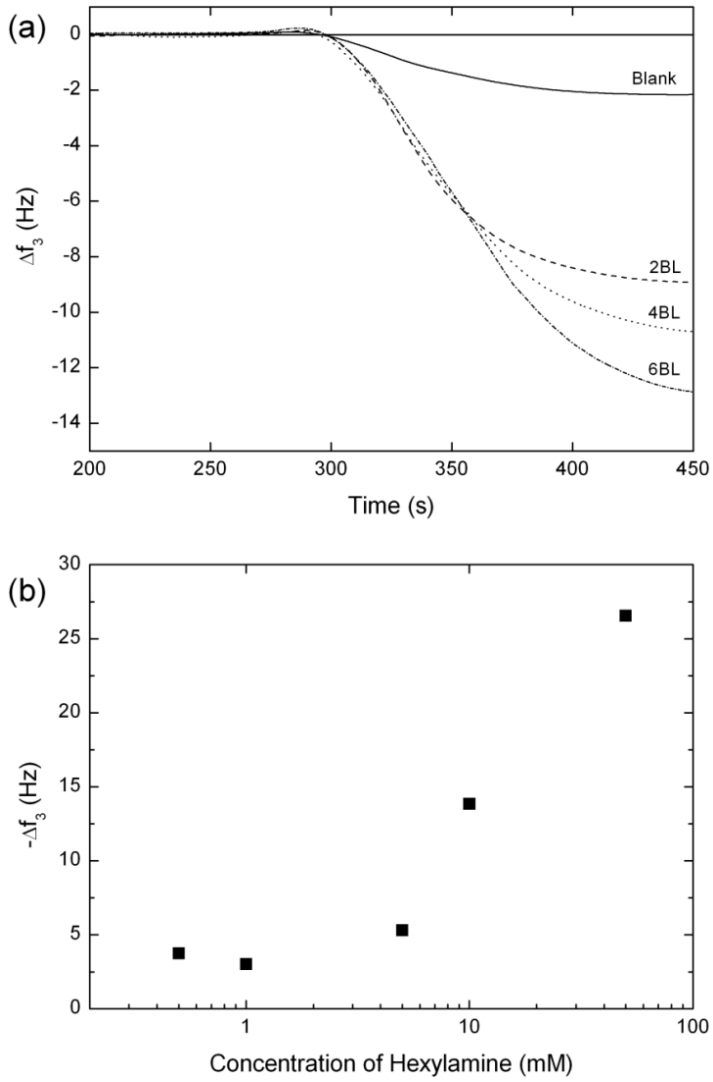

Figure 2.11. (a) QCM frequency shifts as a function of time for a blank QCM crystal (solid line) and 2, 4 and 6 bilayers of TiO_2/SiO_2 LbL film assembled on the crystal (dashed lines). (b) Frequency shifts as a function of hexylamine concentration for a 6–bilayer TiO_2/SiO_2 LbL film.

The combination of zeta potential of LbL films and QCM measurements confirm that adsorption of HA on SiO_2 nanoparticles within the film leads to charge inversion of the surface, thus enhancing LbL film growth. In addition to the film surface charge inversion effect, the decrease in surface charge of SiO_2 nanoparticles upon adding HA (Figure 2.4) leads to the enhanced growth of TiO_2/SiO_2 LbL films as discussed earlier. The decrease in surface charge results in more SiO_2 nanoparticles adsorbing on the surface to compensate the positive charge of the previous layer. Furthermore, the electrostatic repulsion between SiO_2 nanoparticles is reduced so that SiO_2 nanoparticles pack densely, leading to thicker films. Previous studies have observed a similar effect of obtaining greater surface coverage of nanoparticles by suppressing the electrostatic repulsion between particles via increasing the ionic strength of particle suspensions or by reducing the surface charge of particles via changing the suspension pH.[61, 62, 66-68] In short, the suppression of SiO_2 nanoparticle charge and the charge inversion of the LbL films due to the adsorption of HA on SiO_2 nanoparticles within LbL films contribute to the observed increase in LbL film growth.

2.4 Conclusions

In conclusion, the study presented in this chapter demonstrated that a small amphiphilic molecule, hexylamine (HA), can be used to widen the processing window of all–nanoparticle TiO_2/SiO_2 LbL thin films. Upon adding HA into SiO_2 nanoparticle suspensions, the zeta potential of nanoparticles is seen to decrease, yet SiO_2 nanoparticles

remained colloidally stable. The growth of TiO_2/SiO_2 LbL films is shown to significantly increase compared to a prior study within the same pH range. Using zeta potential measurements, the adsorption of HA onto TiO_2/SiO_2 LbL films is found to result in charge inversion of the surface, enabling the adsorption of negatively charged SiO_2 nanoparticles. Furthermore, quartz crystal microbalance (QCM) measurements showed that the suppression of SiO_2 nanoparticle charge leads to more SiO_2 nanoparticles being adsorbed on the film, thus yielding thicker films. This new approach of using short amphiphilic molecules to enhance the growth of nanoparticle LbL thin films will undoubtedly be useful for successfully performing LbL assembly of oppositely charged nanomaterials in a broad pH range.

Chapter 3. Layer–by–Layer Assembly of Charged Particles in Non–Polar Media

Reprinted (adapted) with permission from Tettey, K. E.; Yee, M. Q.; Lee, D. Layer–by–Layer Assembly of Charged Particles in Nonpolar Media. Langmuir, 2010, 26, 9974–9980. Copyright (2010) American Chemical Society.

3.1 Introduction

Nanoparticle later–by–layer (LbL) assembled thin films have traditionally been assembled in aqueous solution or, in some instances, in polar media such as alcohol[41] and formamides.[42,43] Materials synthesized in non–polar solvents are typically not suitable candidates for LbL assembly due to their poor solubility and stability in aqueous solution. This limitation can be an obstacle to generating functional LbL thin films since a large number of unique nanomaterials such as quantum dots, magnetic nanoparticles, and polymers are indeed synthesized in non–polar solvents.[45-48] LbL assembly in non–polar solvents (i.e. $\varepsilon \sim 2 - 5$)[44] is challenging because materials dispersed in non–polar solvents typically do not acquire charge. This fundamental limitation has most likely inhibited attempts to performing LbL assembly in non–polar solvents.

Although materials dispersed in non–polar solvents generally do not acquire charge, recent studies have shown that the addition of an amphiphilic surfactant such as Aerosol–OT (sodium bis(2–ethylhexyl) sulfosuccinate), shown in Figure 3.1, can impart charge on particles in non–polar solvents.[44, 69-71] The stabilization of colloidal particles in non–polar solvents has been shown to occur through electrostatic repulsion. The

repulsive forces between particles have been directly measured,[72,73] indicating that electrostatic effects are significant under appropriate conditions. It is believed that the adsorption of added surfactants onto particles and the presence of surfactant reverse micelles in solution play a crucial role in inducing surface charge on particles.[44] Although the exact charging mechanism via these charge control agents (CCAs) is not completely understood,[69] three mechanisms have been proposed: [74-76]

1. Preferential adsorption of either anions or cations of dissociated electrolyte

2. Dissociation of surface anions or cations and their subsequent stabilization in reverse micelles

3. Adsorption of neutral solute followed by ion exchange between particle surface groups and solute, and subsequent desorption of solute as a charged complex

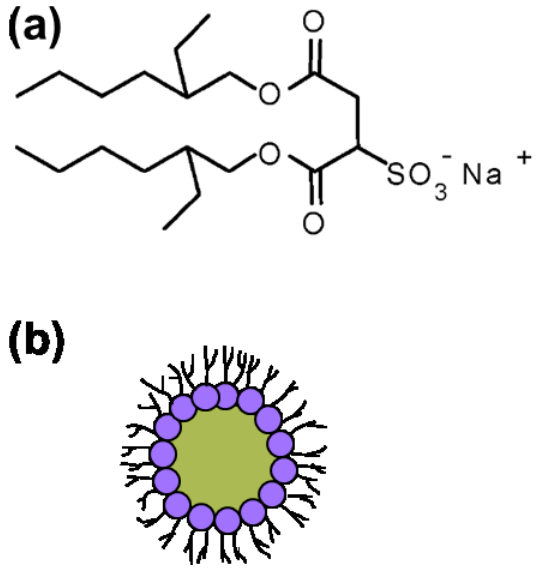

Figure 3.1. (a) Chemical structure of AOT and (b) depiction of AOT reverse micelles.

The aim of the study covered in this chapter is to demonstrate that LbL assembly of charged particles can be achieved in a non–polar solvent. Commonly available particles, namely carbon black (CB) and Al_2O_3, are used as two species to be incorporated into thin films via LbL assembly from a common non–polar solvent, toluene. AOT is added to suspensions of CB and Al_2O_3 in toluene to impart surface charge onto these particles. It will be shown that nanocomposite thin films of CB and Al_2O_3 can be assembled on glass slides based on LbL assembly. Furthermore, the composition and growth behavior of the CB/Al_2O_3 films can be varied by independently controlling the concentrations of AOT in each particle suspension. The results demonstrate that LbL assembly of charged species in non–polar media can lead to generation of nanocomposite thin films, thus resolving the limitation of nanoparticle LbL assembly to aqueous phase.

3.2 Experimental Section

3.2.1 Electrophoretic Mobility Measurements

200 mM of Aerosol–OT (AOT) (Sigma–Aldrich) in toluene (Fisher) is prepared and diluted to 100, 20, 10, 2 and 1 mM AOT/toluene solutions. 0.1 wt. % Al_2O_3 (Cabot SpectrAl 100) and CB (Columbian Chemicals Conductex 7055 Ultra) suspensions are prepared in pure toluene and sonicated for 1 hour to obtain fine suspensions. The Al_2O_3 suspension is vigorously shaken for ~30 seconds to disperse the particles, and then 3 mL is immediately transferred and mixed with 3 mL of each AOT/toluene solution to yield 0.05 wt. % Al_2O_3 in AOT/toluene dispersions. The Al_2O_3 dispersions in AOT/toluene are

subsequently sonicated for 1 hr. The same procedure is repeated for CB. Electrophoretic mobility measurements are performed with a Beckman Coulter Delsa Nano–C. Al_2O_3 dispersions are allowed to settle overnight to obtain a homogenous top layer for use in electrophoretic mobility measurements. CB dispersions for electrophoretic mobility measurements are centrifuged at 5000 rpm for 5 min then filtered with a 5–μm PTFE syringe filter to obtain a homogenous dispersion with an appropriate intensity signal. Three measurements are made for each suspension at an electric field of 85.2 V/cm. The nitrogen surface area (NSA) of CB and Al_2O_3 are 55 and 95 m^2/g, respectively, as provided by the manufacturers. Al_2O_3 and CB particles are used as received.

3.2.2 Layer–by–layer Assembly of Carbon Black and Al_2O_3 in Toluene

200 mM AOT/toluene solution is prepared by adding AOT in pure toluene and then sonicating for 20 min to ensure that AOT is completely dissolved. The 200 mM AOT/toluene solution is subsequently diluted to 20 and 2 mM solutions. 0.1 wt. % suspensions of CB and Al_2O_3 each in vials of 60 mL of pure toluene are sonicated for 20 min. The particle suspension in pure toluene is shaken vigorously for 30 seconds, and then 30 mL of each particle suspension is mixed with AOT/toluene solution in a 1:1 ratio to yield 60 mL of 0.05 wt. % particle in 100, 10 and 1 mM AOT/toluene. The particle dispersions in AOT/toluene are subsequently sonicated for 20 min. Particle dispersions are used for LbL assembly 5 min after sonication. LbL assembly is performed on glass slides (Fisherbrand plain microscope slides), which are cleaned by sonicating in 1.0 M NaOH for 20 min, thorough rinsing in de–ionized (DI) water (18.2 Ω–cm) and drying

with compressed air. The first LbL rinse bath consists of 60 mL of AOT/toluene at the same AOT concentration as the particle dispersions. The remaining rinse baths consist of 60 mL of pure toluene. Altogether, the LbL assembly consisted of baths of 0.05 wt. % CB in AOT/toluene, AOT/toluene rinse, toluene and toluene followed by 0.05 wt. % Al_2O_3 in AOT/toluene, AOT/toluene rinse, toluene and toluene. A StratoSequencer VI (NanoStrata Inc.) is programmed to expose the substrates to each particle dispersion for 10 min followed by 2, 1, and 1 min of rinse steps. Control samples are generated by substituting CB for Al_2O_3 so that only CB would be sequentially deposited on glass slides. While samples assembled from particle dispersions with 1, 10 and 100 mM AOT yielded uniform films, those assembled from particle dispersions with 0.5 mM AOT are not uniform.

3.2.3 CB/Al_2O_3 Film Characterization

UV–Vis absorbance measurements are performed using a Cary 5000 (Varian Inc.) UV–Vis–NIR spectrophotometer. The absorbance at 500 nm is used for all data analysis. Scanning electron microscopy (SEM) images are taken using an FEI 600 Quanta FEG ESEM at 5 kV and at a working distance of 10 mm. Atomic force microscopy (AFM) images are taken using an Agilent/Molecular Imaging PicoPlus AFM. Film thickness measurements are obtained using a Zygo NewView 6K series optical profilometer. A small scratch is made on the CB/Al2O3 film in order to use the bare glass substrate as a reference zero height as shown in Figure 3.2a. The height profile on either side of the

scratch (Figure 3.2b) is integrated and normalized with the profile length to get an average film thickness using the equation shown in Equation 3–1.

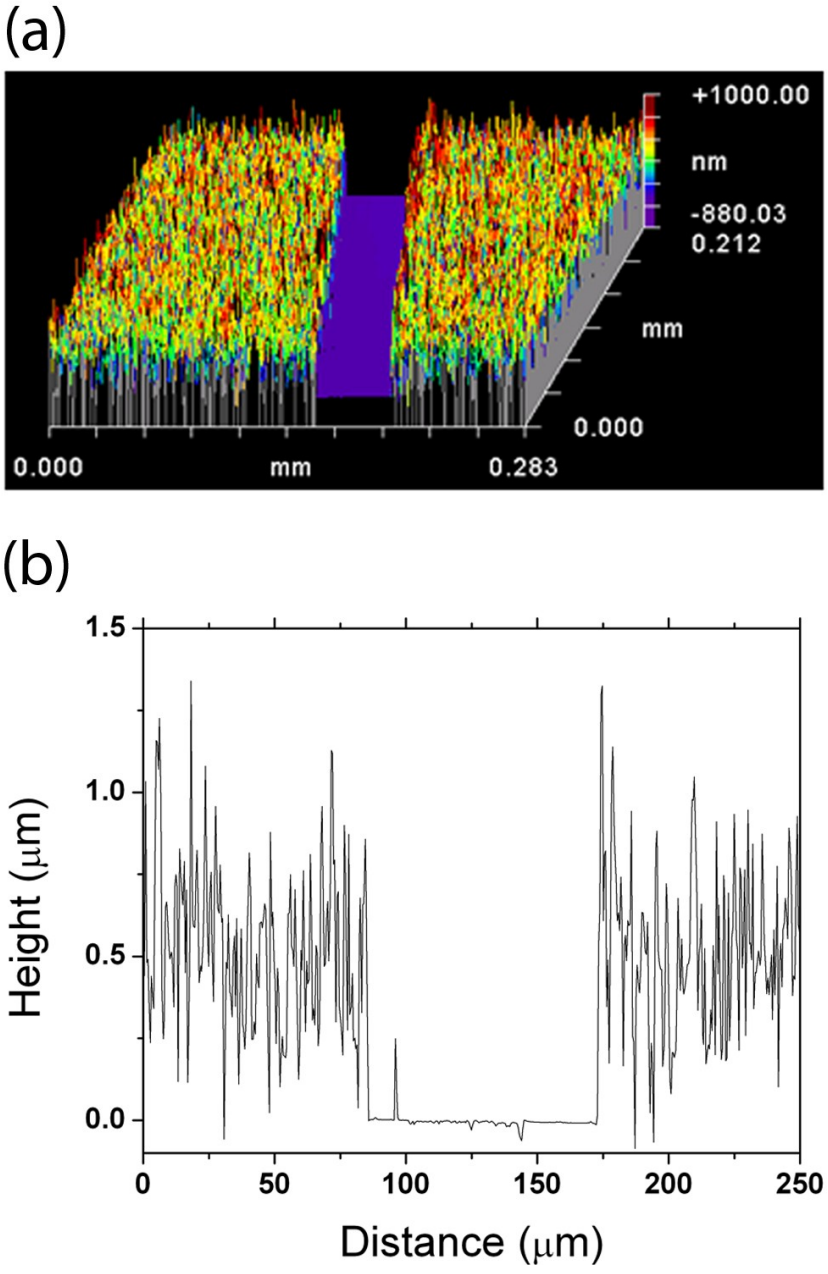

Figure 3.2. (a) Three–dimensional film profile of 15 bilayer CB/Al_2O_3 film from optical profilometry. (b) Height profile of 15 bilayer CB/Al_2O_3 film obtained from optical profilometry. The CB/Al_2O_3 film is assembled using 100 mM AOT/toluene solutions.

Equation 3–1. Calculation of film thickness from optical profilometry height profile

$$Thickness = \frac{\int (height\ profile) dx}{\int dx}$$

The film composition is determined by using thermogravimetric analysis (TA Instruments model 2960 SDT). Thick films (60 bilayers) are assembled on glass slides then scraped off into a platinum TGA pan. The temperature is increased at 10 ^{o}C/min to 110 ^{o}C then held for 20 min to remove moisture. The temperature is subsequently ramped at 10 ^{o}C/min to 1000 ^{o}C. Film conductivity measurements are performed with a Cascade Microtech C4S 4–Point probe head coupled with an Agilent DC power supply unit and Keithley 2000 multimeters. Current–voltage measurements are performed on four random positions on 30 bilayer films in order to obtain the sheet resistance. The sheet resistance of a sample and its respective film thickness are used to determine the resistivity of the film. The inverse of the film resistivity is calculated to find the film conductivity.

3.3 Results and Discussion

3.3.1 Charging of Al_2O_3 and Carbon Black in Toluene

One of the essential properties required for a material to be incorporated into thin films using layer–by–layer (LbL) assembly is that it is charged in its medium. Al_2O_3 and carbon black (CB) do not acquire charge in pure toluene and precipitate due to poor

colloidal stability as shown by the leftmost vials in Figure 3.3a and Figure 3.3b, respectively.

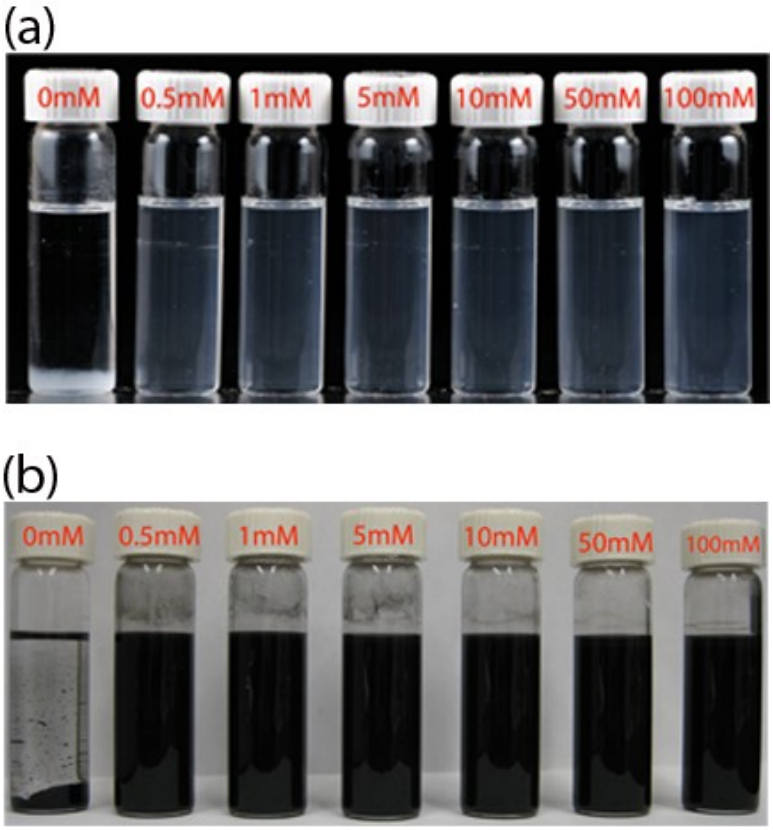

Figure 3.3. (a) Al_2O_3 and (b) carbon black dispersed in toluene containing different concentrations of AOT ([AOT]).

Surface charge is imparted on CB and Al_2O_3 particles in toluene by adding a surfactant, Aerosol–OT (AOT). CB and Al_2O_3 particles became well dispersed and colloidally stable in toluene upon adding AOT in a wide range of concentrations as shown in Figure 3.3a and Figure 3.3b. The particle dispersions are stable for several weeks, although sedimentation gradually occurs with time. Sedimented particles, however, can be easily re–dispersed with gentle agitation.

The effect of [AOT] on the particle surface charge in toluene is further studied by measuring the electrophoretic mobility of particles. The magnitude of the electrophoretic mobility is indicative of the surface charge of particles. [‡] The most important result is that CB and alumina acquire opposite charge in solution as shown in Figure 3.4a and Figure 3.4b; CB is negatively charged, whereas Al_2O_3 becomes positively charged in AOT/toluene solutions. The difference in the polarity of CB and Al_2O_3 surfaces could have led to the acquisition of opposite surface charge by these two particles. A previous study using TiO_2 nanoparticles demonstrated that the surface charge of TiO_2 particles in AOT/toluene depends on the surface polarity (or hydrophilicity) of the particles rather than its bulk composition.[71] Indeed, while Al_2O_3 could be suspended to form homogeneous dispersion in water, CB precipitated in water, which confirms that Al_2O_3 has a hydrophilic surface, whereas CB is hydrophobic. The electrophoretic mobility obtained are also consistent with a previous study that demonstrated the acquisition of negative surface charge by CB in several non–polar solutions with AOT.[74, 77]

The results obtained (Figure 3.4) show that the electrophoretic mobility of Al_2O_3 and CB depends on the concentration of AOT ([AOT]). The electrophoretic mobility of Al_2O_3 has a maximum value around 10 mM AOT and gradually decreases as [AOT] is increased above 10 mM. At low [AOT], the adsorption of AOT molecules on the surface of the particles could increase the surface charge of the particles and, hence, their electrophoretic mobility.[74, 78] The gradual decrease of electrophoretic mobility beyond a

[‡] Because of the uncertainty of the nature of the double layer in non–polar media, the electrophoretic mobility will henceforth be used to characterize the charge of particles in non–polar media as opposed to the zeta–potential.

maximum value is likely due to attraction of counterions to the particle surface, which in turn leads to neutralization of the surface charge.[70,71] The magnitude of the electrophoretic mobility of CB decreases gradually as [AOT] is increased above 0.5 mM. For CB, no peak in the magnitude of electrophoretic mobility is detected within the concentration range used in this stud; however, a maximum value (in magnitude) could be present between 0 and 0.5 mM AOT since CB in pure toluene has little charge, as evidenced by its poor colloidal stability in pure toluene (Figure 3.3b). Previous studies have shown similar trends for both hydrophilic and hydrophobic particles.[70, 71, 77]

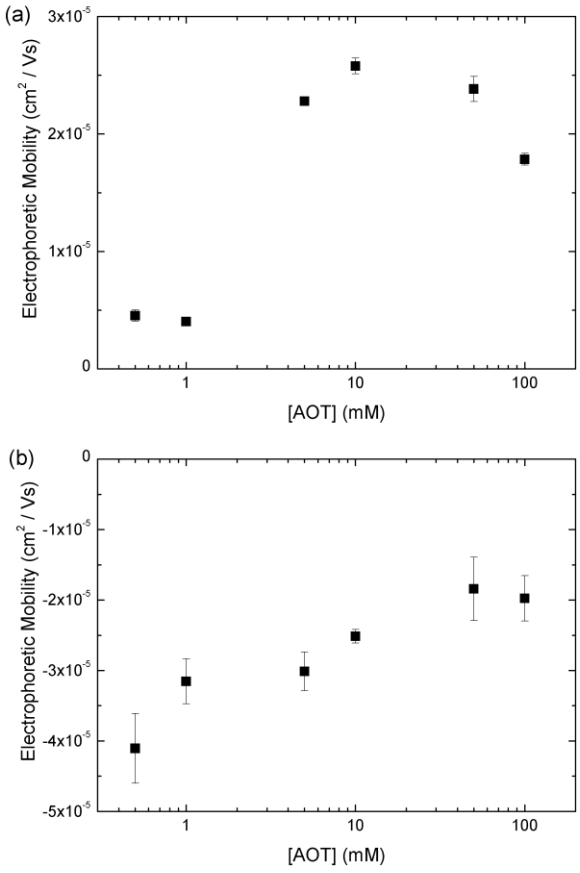

Figure 3.4. Electrophoretic mobility of dispersed (c) Al_2O_3 and (d) carbon black as a function of [AOT] in toluene. Error bars indicate standard deviations from three measurements.

3.3.2 Heteroaggregation of Carbon Black and Al_2O_3 in Toluene

Attractive interactions between a pair of materials are necessary to form LbL assembled thin films. A simple method to test for the presence of attractive forces in a medium is to mix suspensions of oppositely charged species. Heteroaggregation of oppositely charged colloidal particles in aqueous media has been investigated extensively,[79] but similar phenomena involving two oppositely charged particles in non–polar solvents is not been well documented.[80,81] To test for the existence of attractive interactions between oppositely charged particles, CB and Al_2O_3 in AOT/toluene solution were mixed together in a 1:1 ratio. The mixture becomes clear overnight, indicating that the two particles aggregate and precipitate from the suspension as shown below in Figure 3.5. The heteroaggregation of oppositely charged CB and Al_2O_3 strongly suggests the existence of attractive forces in this non–polar medium.

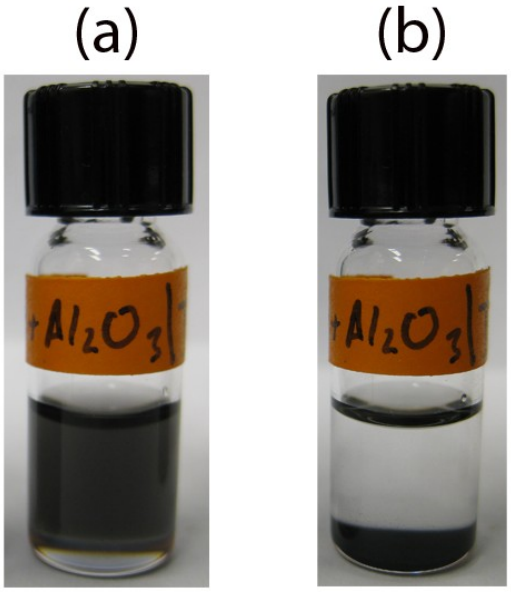

Figure 3.5. Heteroaggregation of charged CB and Al_2O_3 in toluene at (a) time = 0 and (b) time = 16 hours. The concentration of AOT in each mixture is 100 mM.

3.3.3 Layer–by–Layer Assembly of Charged Carbon Black and Al_2O_3 in Toluene.

The acquisition of opposite surface charge by CB and Al_2O_3 and the heteroaggregation of the two particles in AOT/toluene solutions strongly suggest that LbL assembly of CB and Al_2O_3 is feasible. However, the first particle to be deposited needs to be determined before performing LbL assembly of the two particles. This is determined by exposing cleaned glass slides to suspensions of CB and Al_2O_3 in 10 mM AOT/toluene solutions. AFM images (Figure 3.6) of the glass slides showed that the particle density of CB is much higher than that of Al_2O_3 after rinse steps. These results suggest that the glass surface acquires a positive charge in AOT/toluene solutions in contrast to the negative charge that glass acquires in aqueous solutions. However, previous studies have shown conflicting results in the sign and magnitude of silica charge in non–polar media doped with AOT. In one study, the charge of silica was found to be negative at low concentrations of AOT and to subsequently reverse to positive with increasing concentration of AOT.[70] In separate studies by Berg et al., the charge of silica was shown to remain negative for all AOT concentrations.[82, 83] The origin of the inconsistency in the charge of silica will be addressed in *Chapter 4*.

After determining the first particle to be deposited, LbL assembly of charged CB and Al_2O_3 in toluene was performed to generate CB/Al_2O_3 nanocomposite thin films. The assembled films are observed to become darker with increasing number of deposited bilayers as shown below in Figure 3.7a. A control experiment is performed to test the possible contribution of non–specific adsorption of CB particles and/or evaporation–induced particle deposition[84] on film growth. With repeated exposure of glass slides to

CB suspensions with rinse steps, the slides do not become significantly darker after the formation of the first layer of CB particles (Figure 3.7b).

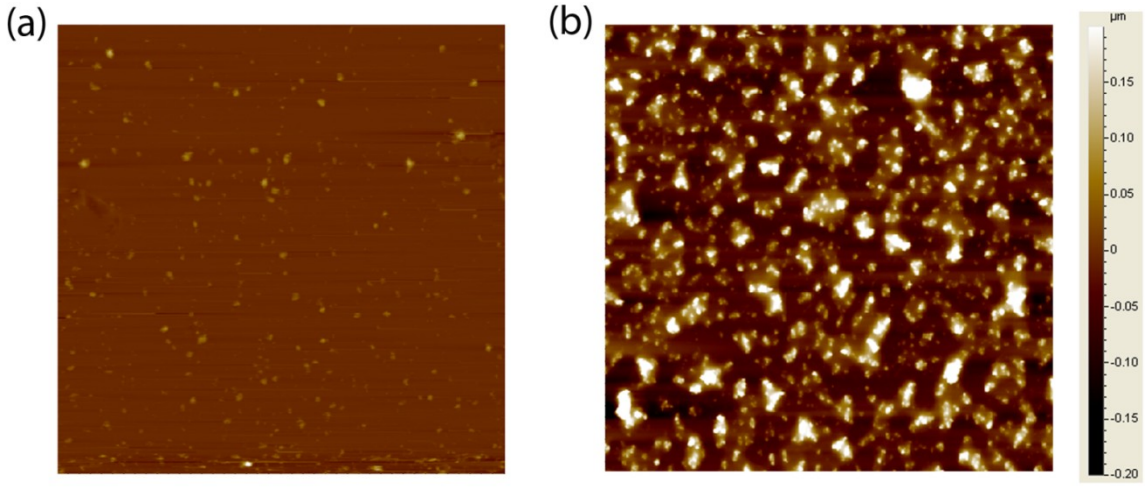

Figure 3.6. AFM images of glass slides after deposition of (a) Al_2O_3 and (b) CB in 10 mM AOT/toluene. Each side of AFM image corresponds to 20 µm.

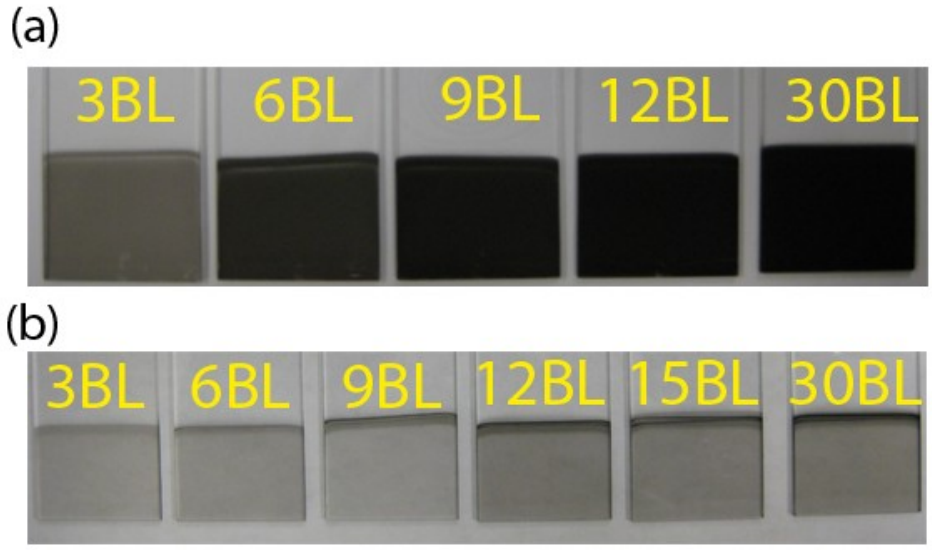

Figure 3.7. Photograph of (a) LbL assembled CB/Al_2O_3 films and (b) carbon black film formed from control experiment on glass slides. The text on glass slides represents the number of deposited bilayers (e.g. 3BL = 3 bilayers).

To quantify the film growth, UV–Vis absorbance at 500 nm is measured as a function of the number of deposited bilayers (Figure 3.8). These results show that the absorbance increases linearly with the number of deposited bilayers, suggesting that the films grow linearly; this is a hallmark of LbL assembly of oppositely charged species. The measured absorbance on the control samples (Figure 3.8) confirms that the absorbance of control films is much lower than LbL films and that the increase in the darkness of control samples with increasing number of deposited layers is small. These results indicate that the alternate deposition of oppositely charged Al_2O_3 and CB leads to the buildup of LbL nanocomposite thin films.

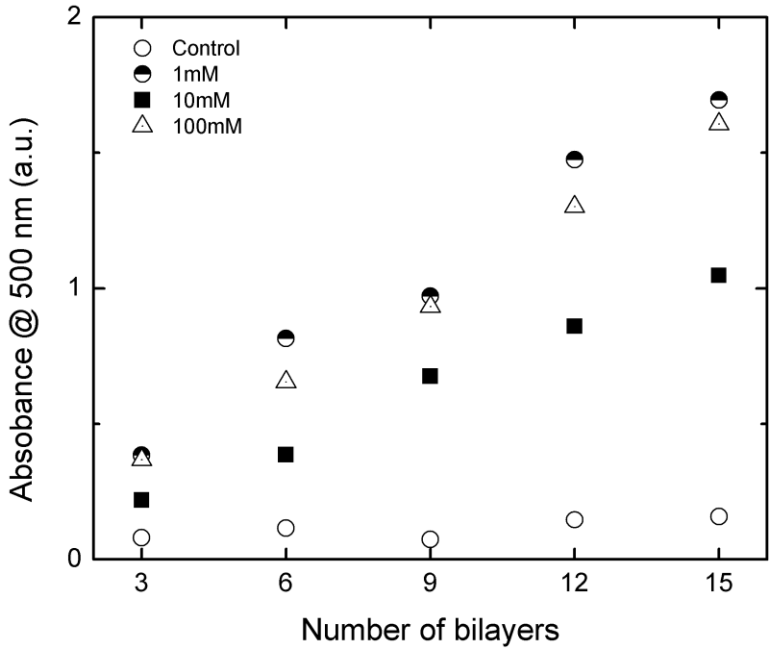

Figure 3.8. Absorbance (at 500 nm) of CB/Al_2O_3 LbL films on glass slides as a function of the number of deposited bilayers. Absorbance measurements were taken for 1, 10, and 100 mM AOT in CB and Al_2O_3. Absorbencies for control sample are shown by open circles.

The morphology of CB/Al_2O_3 LbL films is characterized by using scanning electron microscopy (SEM) as shown in Figure 3.9. SEM images (Figure 3.9a – c) show that the surface coverage increases with the number of deposited bilayers. The cross–sectional SEM image (Figure 3.9d) of a 30 BL sample illustrates that the nanocomposite film uniformly covers the substrate. For samples with a small number of bilayers as shown in Figure 3.9a, the particles are seen to cluster into isolated regions on the surface. These islands grow laterally and eventually merge to form a vertically–growing, uniform thin film at large numbers of bilayers, as seen in Figure 3.9c. Similar film morphology transformations have been observed in LbL assembled–films of a charged nanoparticle and an oppositely charged polyelectrolyte in aqueous solutions.[85] This study concluded that the lateral expansion mode (i.e. lateral growth of isolated domains) is a result of particles adhering to existing islands rather than the bare surface. This phenomenon was attributed to a compensation effect that reduces the number of adsorbed particles as the area of the film expands by: (i) partial desorption of previously adsorbed particles during adsorption of the next layer or (ii) increased electrostatic repulsion between charged components during film growth.

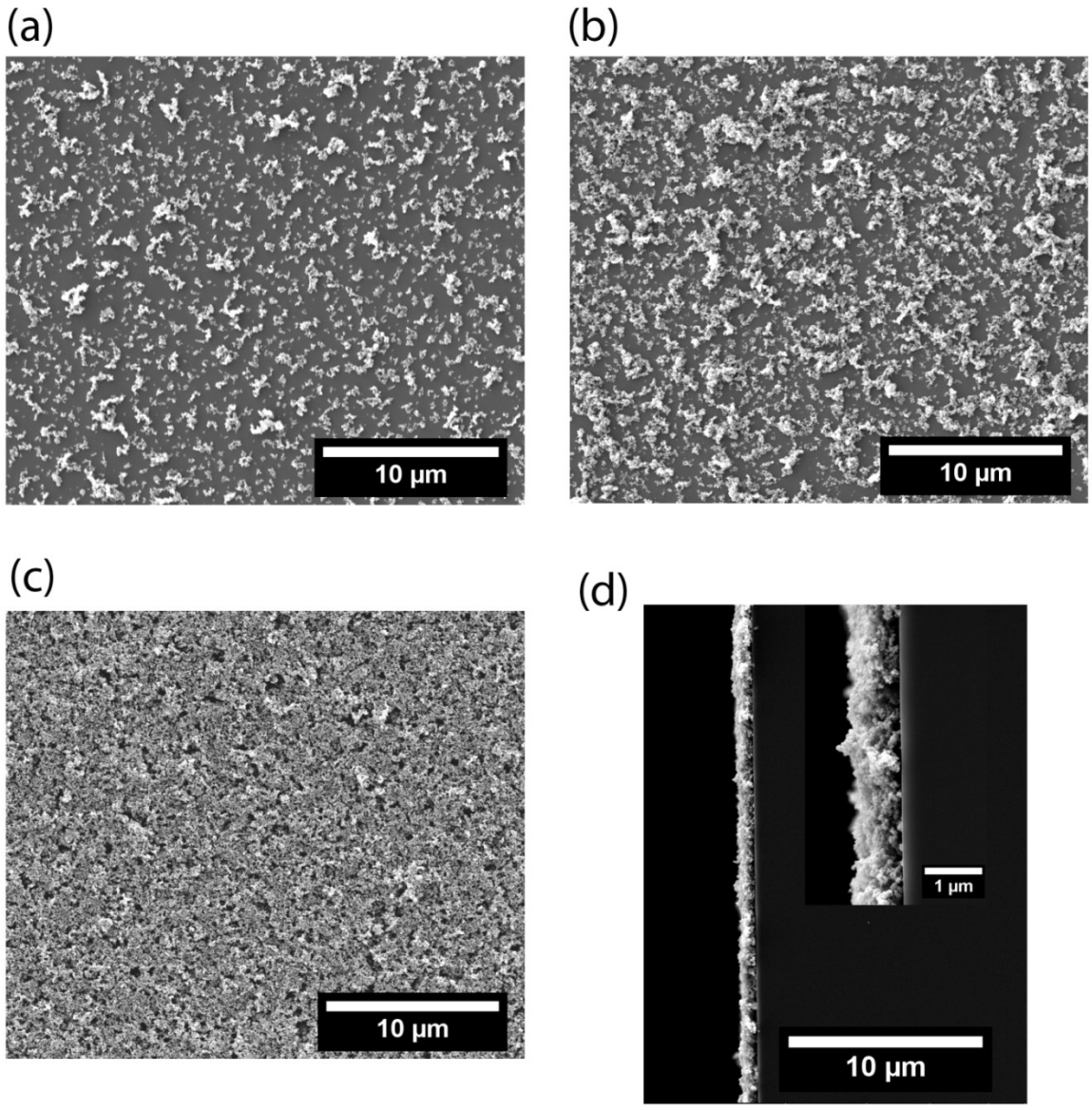

Figure 3.9. SEM images of CB/Al_2O_3 nanocomposite films after deposition of (a) 3 bilayers, (b) 6 bilayers and (c) 30 bilayers. (d) A cross–sectional SEM image of 30 bilayer CB/Al_2O_3 nanocomposite thin film on a silica wafer. The CB/Al_2O_3 films were assembled using 10 mM AOT in particle suspensions.

3.3.4 Effect of Assembly Conditions on the Physicochemical Properties of CB/Al_2O_3 Nanocomposite Thin Films

The versatility of LbL assembly in aqueous solutions is in the possibility of generating thin films with controlled structure and properties. This can be readily achieved by varying assembly conditions such as pH or ionic strength of the aqueous solution.[12,58,86] The effect of [AOT] on the composition and growth behavior of CB/Al_2O_3 films is examined since the [AOT] was shown to influence the surface charge of CB and Al_2O_3 in toluene. The effect of these assembly conditions on the absorbance per bilayer and the thickness of 15 bilayer samples are shown in Figure 3.10a,b. These results show that [AOT] in either suspension plays a critical role in changing the physical properties of the film. A similar trend is seen for the absorbance and thickness measurements; that is, the lowest values occur when the AOT concentration of CB suspension is 10 mM, whereas the highest values are obtained for 1 mM AOT in CB suspension. The concentration of AOT in CB suspensions shows a more pronounced effect compared to its concentration in Al_2O_3 suspensions.

The compositions of CB/Al_2O_3 films is further analyzed using thermogravimetric analysis (TGA).[87] Figure 3.11 shows the changes in mass with respect to temperature for CB/Al_2O_3 nanocomposite thin films generated from suspensions with 1, 10 and 100 mM AOT. Each TGA thermogram for different CB/Al_2O_3 films shows two distinct decomposition regimes. The first degradation regime between 200 and 300 ^oC arises from the decomposition of residual AOT in the nanocomposite thin films. Figure 3.11 shows that in this regime, the drop in % mass increases with [AOT] in the particle dispersion,

which indicates that the amount of residual AOT in the films increases with [AOT]. The second regime is from the decomposition of CB. Interestingly, the onset of CB decomposition is seen to occur at lower temperatures as [AOT] is increased. Changes in the decomposition temperature of a carbon–based material has been observed before in carbon nanofiber–polymer composites.[88] In that study, the changes in decomposition temperature were attributed to polymer–nanofiber interactions that modulate the thermal stability of the carbon nanofiber. It is possible that the decomposition of residual AOT in the film, possibly on the surface of CB, facilitates the oxidation of CB at low temperatures.

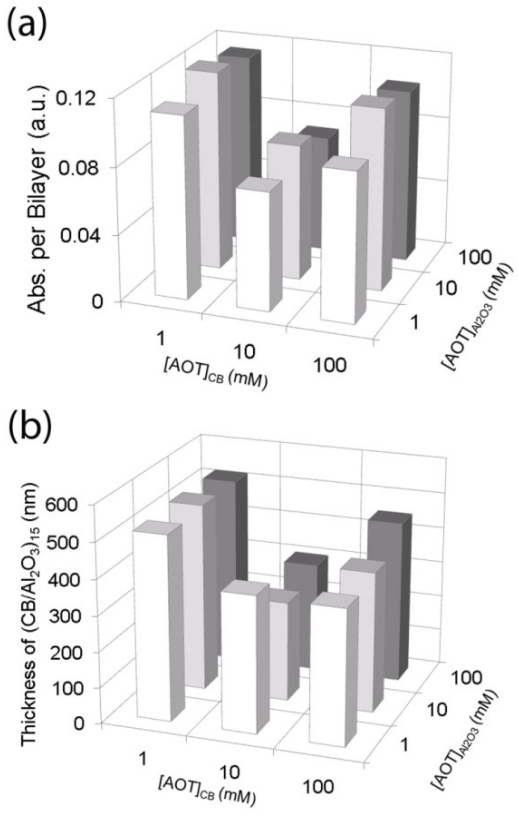

Figure 3.10. Histograms showing (a) the absorbance per bilayer (arbitrary units) and (b) the thickness (nm) of the 15 bilayer films as a function of the concentration of AOT (mM) in Al_2O_3 and CB suspensions.

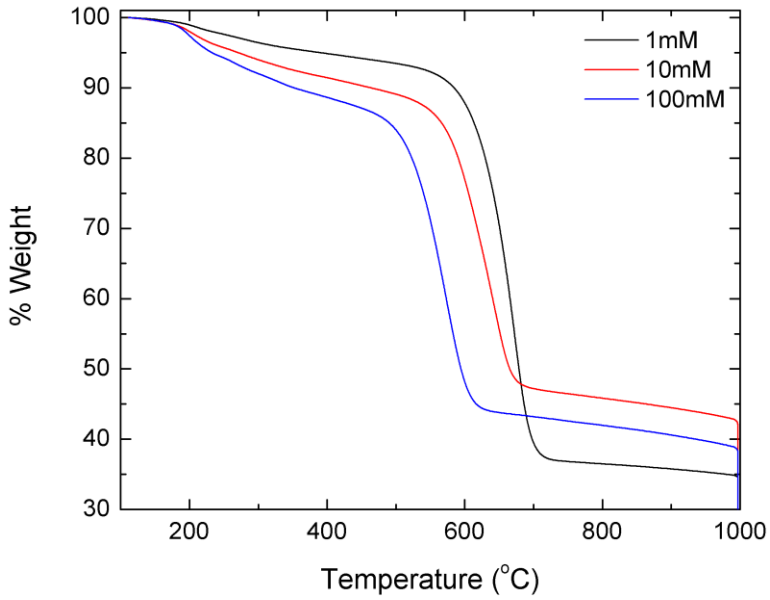

Figure 3.11. Change in mass of CB/Al_2O_3 films as a function of temperature using thermogravimetric analysis (TGA). Black, red and blue lines represent thermograms of CB/Al_2O_3 films assembled in 1 mM, 10 mM, and 100 mM AOT/toluene solutions, respectively.

The compositions of CB/Al_2O_3 nanocomposite thin films as determined from TGA are summarized in Table 1. The relative mass fraction of CB in the nanocomposite thin films agrees well with the results shown in Figure 3.10; the CB/Al_2O_3 film assembled at 1 mM AOT contains the largest amount of CB. These results clearly demonstrate that modifying the surface charge of CB and Al_2O_3 particles by changing [AOT] provides a versatile way of controlling the structural properties of CB/Al_2O_3 nanocomposite films.

3.3.5 Electrical Properties of CB/Al_2O_3 Nanocomposite Thin Films

Carbon black is often used as a filler to improve the electrical conductivity of insulators. Electrically conductive ceramics can be used in a broad range of applications such as static dissipation and protection.[89] The electrical properties of CB/Al_2O_3 are probed by measuring the conductivity of CB/Al_2O_3 films generated from 1, 10 and 100 mM AOT solutions (Table 3.1). For all three samples, the films became conductive due to the percolation of CB within the films. The measurements show that the conductivity of films depends on [AOT]. In addition, there is a positive correlation between the relative mass fraction of CB and the film conductivity. This is expected since CB is the conductive component in the films.

Table 3.1. Composition and conductivity of CB/Al_2O_3 films determined from TGA and four–point probe measurement, respectively. m_i indicates wt. % of component *i*.

[AOT] (mM)	m_{CB}	m_{Al2O3}	m_{AOT}	$\frac{m_{CB}}{m_{CB}+m_{Al2O3}}$	**Conductivity (S/m)**
1	57	37	6	61	28.49 ± 0.44
10	43	47	10	48	8.54 ± 0.01
100	44	44	12	50	21.31 ± 0.02

3.4 Conclusions

In conclusion, layer–by–layer (LbL) assembly of oppositely charged materials is demonstrated in a common non–polar solvent, toluene, thus addressing the second limitation of nanoparticle LbL. A surfactant, AOT, is used to induce negative and positive surface charge on carbon black (CB) and Al_2O_3, respectively. While each particle is stable in AOT/toluene solution via charge stabilization, a mixture of the two particles results in heteroaggregation, suggesting the existence of an attractive force. LbL assembly of CB/Al_2O_3 films can be performed on glass slides and the concentration of the charge inducing agent, AOT, is shown to play a crucial role in controlling the properties of the films such as composition and thickness. The simplicity of this procedure is advantageous for creating nanocomposite thin films of ceramics and CB in non–polar solvents.

Chapter 4. Effect of Thermal Treatment and Moisture Content on the Charge of Silica Particles in Non–Polar Media

Reproduced by permission of The Royal Society of Chemistry. K. E. Tettey and D. Lee. Effect of thermal treatment and moisture content on the charge of silica particles in non–polar media. Soft Matter. 2013, 9, 7242-7250.

4.1 Introduction

In *Chapter 3*, the limitation of nanoparticle LbL to aqueous phase was addressed by using a surfactant Aerosol–OT (AOT) to impart charge on common particles in toluene. Previous studies have however shown that the amount of water in non–polar media can drastically affect the charge behavior of various particles.[90-92] An understanding of the effect of moisture content on the charge of particles is important since water is practically impossible to eliminate in non–polar media. Furthermore, it is important to understand the nature of the surface chemistry of colloids and its relation to charge acquired in non–polar media.

Some prior studies, which have tried to establish such a relation, have shown conflicting results. For example, in one study, the charge of silica was found to be negative at low concentrations of AOT and to subsequently reverse to positive with increasing concentration of AOT.[70] Meanwhile, two separate studies by Berg *et al.* found that the charge of silica remains negative for all AOT concentrations.[82, 83] In fact, the results shown in *Chapter 3* suggest that glass slides acquire a positive charge in

AOT/toluene. It is more than likely that these differences in the charge acquired for the same bulk material, silica, is a result of the surface groups present.

The goal of the study presented in this chapter, therefore, is to gain insights into the effect of moisture content and surface chemistry on the charge of silica in non–polar solvents. To study the effect of these two parameters, silica particles are thermally treated to alter the surface chemistry, and the moisture content of silica dispersions is controlled by storing them under different relative humidities. Using electrophoretic mobility measurements, Fourier transform infrared (FTIR) spectroscopy, thermogravimetric analysis (TGA), and Karl Fischer titration, it will be shown that the surface chemistry of silica and moisture content does indeed have a significant effect on the charge of silica particles in non–polar media, resulting in charge reversal of the particles in some cases. The results gathered provide some important clues to explain the inconsistent charge results reported for silica in non–polar solvents.

4.2 Experimental Section

4.2.1 Materials

Monodisperse colloidal silica particles are obtained from three different suppliers: Fiber Optics Center Inc. (Silica–1), Alfa Aesar (Silica–2) and Bangs Laboratories Inc. (Silica–3). Silica particles are also synthesized using the Stöber method.[93] Briefly, a 2.1 g solution of Tetraethyl orthosilicate (TEOS) (Sigma Aldrich) is added to a solution of 38 g of ethanol (Fisher), 9 g of deionized (DI) water (18.2 MΩ–cm, purified by a Barnstead

Nanopure System) and 1.4 g of concentrated NH_4OH (Fisher) under vigorous stirring at room temperature. The combined solution is stirred overnight (~18 hours) before further use. Stöber particles (Silica–4) are washed in DI water through multiple centrifugation and redispersion steps, and are used following overnight drying at 70 ^{o}C under vacuum. Thermally treated silica samples are prepared by placing silica powder in an alumina crucible and heating in a furnace to the desired temperature for the required time. Silica dispersions are immediately prepared after thermal treatment. Only Silica–1 particles are used to study the effect of thermal treatment and moisture content. Methyl red solution (Sigma Aldrich) is prepared by adding the dye into toluene, followed by 20 minutes of sonication.

4.2.2 Silica Particle Characterization

Particle size measurements (Delsa Nano C, Beckman Coulter) are performed by preparing dispersions of 0.05 wt % silica in DI water. The hydrodynamic diameter of the particles are 240 $\pm$ 11 nm for Silica–1, 169 $\pm$ 4 nm for Silica–2, 337 $\pm$ 14 nm for Silica–3 and 250 $\pm$ 11 nm for Silica–4. Scanning electron microscopy (SEM) images of Silica–1 particles are taken using an FEI 600 Quanta FEG ESEM at 5 kV and at a working distance of 10 mm. Fourier transform infrared spectra (FTIR) are obtained using a Nicolet 8600 FTIR spectrometer (Thermo Scientific). Freestanding pellets of silica mixed with KBr are prepared for this purpose. The isolated silanol peak height is normalized with the peak height of the overtone structure at ~1870 cm^{-1}.[94] Weight loss of silica due to dehydration and dehydroxylation is determined using thermogravimetric analysis (TA

instruments Q600). Samples are heated to 1000 ^{o}C at 5 ^{o}C/min in a stream of nitrogen flowing at 10 mL/min. The physisorbed water content of silica particles is calculated as the percent weight loss of silica samples between room temperature and the temperature at which all physisorbed water is removed.[95-97] This latter value is determined as the first temperature where the derivative of weight change becomes zero. Three–phase contact angle measurements of planar silica substrates in a continuous phase of pure toluene are performed with a contact angle goniometer (Attension by KSV Instruments). A 20 μL drop of DI water is placed on the planar silica substrate immersed in toluene. As–is substrates are used 6 hours after piranha treatment while thermally treated silica substrates are used after heating in a furnace to the desired temperature for 6 hours. Thermally treated substrates are immediately transferred into a glass cuvette containing pure toluene for measurements.

4.2.3 Preparation of Particle Dispersions in AOT/toluene for Electrophoretic Mobility Measurements

200 mM of AOT (Sigma Aldrich) in pure toluene (Fisher) is prepared and diluted to 100, 20, 10, 2 and 1 mM AOT/toluene solutions. 0.1 wt % silica suspensions are prepared in pure toluene and sonicated for 1 hour to get fine suspensions. The silica suspension is vigorously shaken for ~30 seconds to disperse the particles, and then mixed with an equal volume of each AOT/toluene solution to yield 0.05 wt % silica in AOT/toluene solutions. The dispersion of silica in AOT/toluene is subsequently sonicated for 1 hour followed by storage in a desiccator. A desiccant (Drierite) is used to fix the desiccator relative

humidity at 11% (low). Saturated salt solutions of K_2CO_3 and NaCl are used to fix the relative humidity at 47% (medium) and 69% (high), respectively.[98] Silica particle dispersions are kept at a fixed relative humidity for 15–18 hours. Electrophoretic mobility and size measurements of silica dispersions in AOT/toluene are performed with a Beckman Coulter Delsa Nano–C flow cell. Dispersions are briefly vortexed to redisperse aggregates before loading in the flow cell. Electrophoretic mobility measurements are performed at an electric field strength of 85.2 V/cm.

4.2.4 Solution Characterization

The solution conductivity of AOT/toluene stored at a fixed relative humidity is measured with a handheld conductivity meter (D–2 Inc. model JF–1A–HH). Water content is measured with a coulometric Karl Fischer titrator (Denver Instruments model 275KF). Hammett indicator tests are performed by adding 200 μL of methyl red solution to 5 mL of silica in pure toluene suspension (0.01 g/mL) stored at a fixed relative humidity.

4.2.5 Quartz Crystal Microbalance (QCM) Measurements

Silica–coated QCM crystals (Q–Sense) are cleaned by immersing in 2 wt% sodium dodecyl sulfate (SDS) solution for 30 min followed by rinsing with DI water, drying with nitrogen and 10 min oxygen plasma treatment. The output of QCM measurements is a frequency shift (Δf) proportional to mass uptake on the QCM crystal. Frequency shift measurements are performed with an E4 quartz crystal microbalance with dissipation

monitoring (QCM–D) by Q–Sense. A flow rate of 100 μL/min, controlled using a Harvard Instruments syringe pump (model PhD Ultra), is used for all measurements. Pure toluene and AOT/toluene solutions are kept in desiccators at the desired relative humidity during measurements in order to ensure negligible change in the water content of these solutions. Drifts in the baseline frequency shifts are corrected in Origin Pro to yield a steady baseline around zero. All frequency shifts reported are from the fifth overtone (Δf_5). The first 400 seconds are reported for frequency shifts for pure toluene to AOT/toluene transitions.

4.3 Results and Discussion

4.3.1 Effect of Thermal Treatment on Particle Charge

The first part of this study focuses on the effect of thermal treatment on the charge of silica particles in toluene doped with AOT (AOT/toluene). Silica particles are thermally treated for ~6 hours at various temperatures up to 1000 °C. Dynamic light scattering (DLS) measurements and scanning electron microscopy (SEM) images as shown in Figure 4.1 and Figure 4.2 reveal that particles retain their original size distribution after high temperature thermal treatment. However, particles fuse when thermally treated at ~1100 ^{o}C; therefore, the upper temperature limit is set to 1000 ^{o}C for this study.

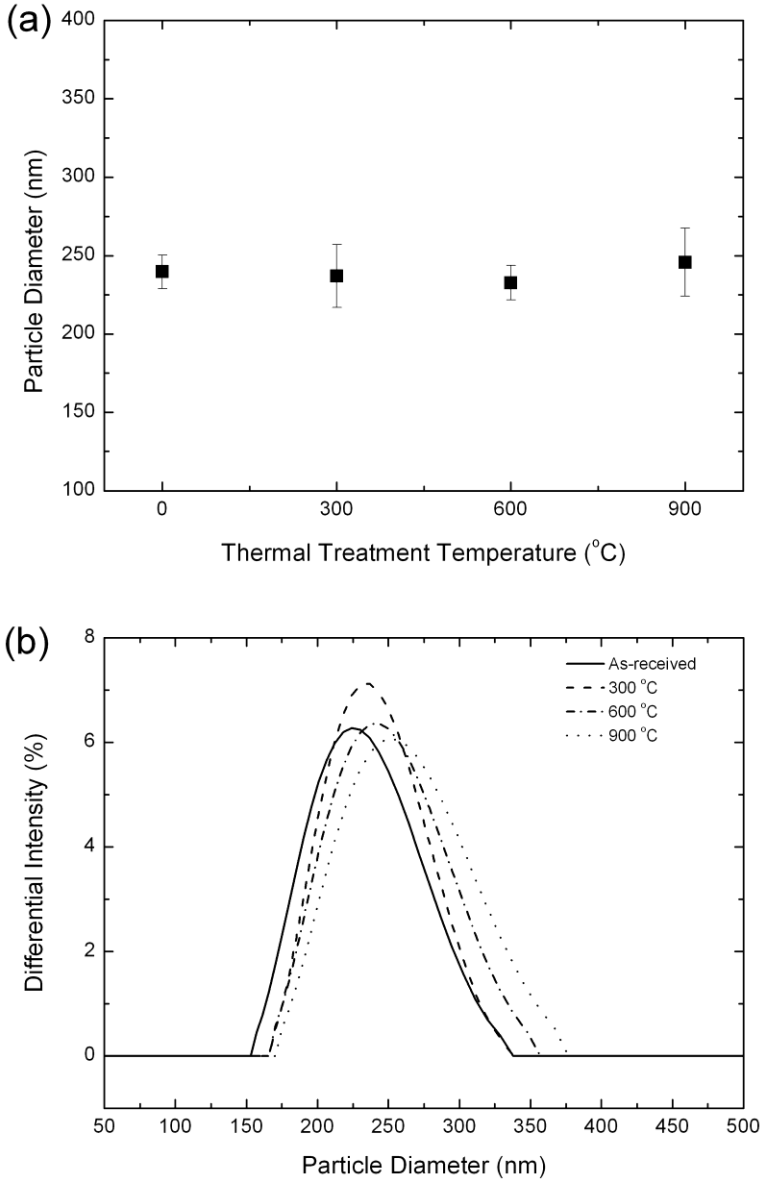

Figure 4.1. Dynamic light scattering (DLS) (a) average particle diameter and (b) size distribution of silica particles as–received and thermally treated at different temperatures. Error bars represent standard deviation of six measurements.

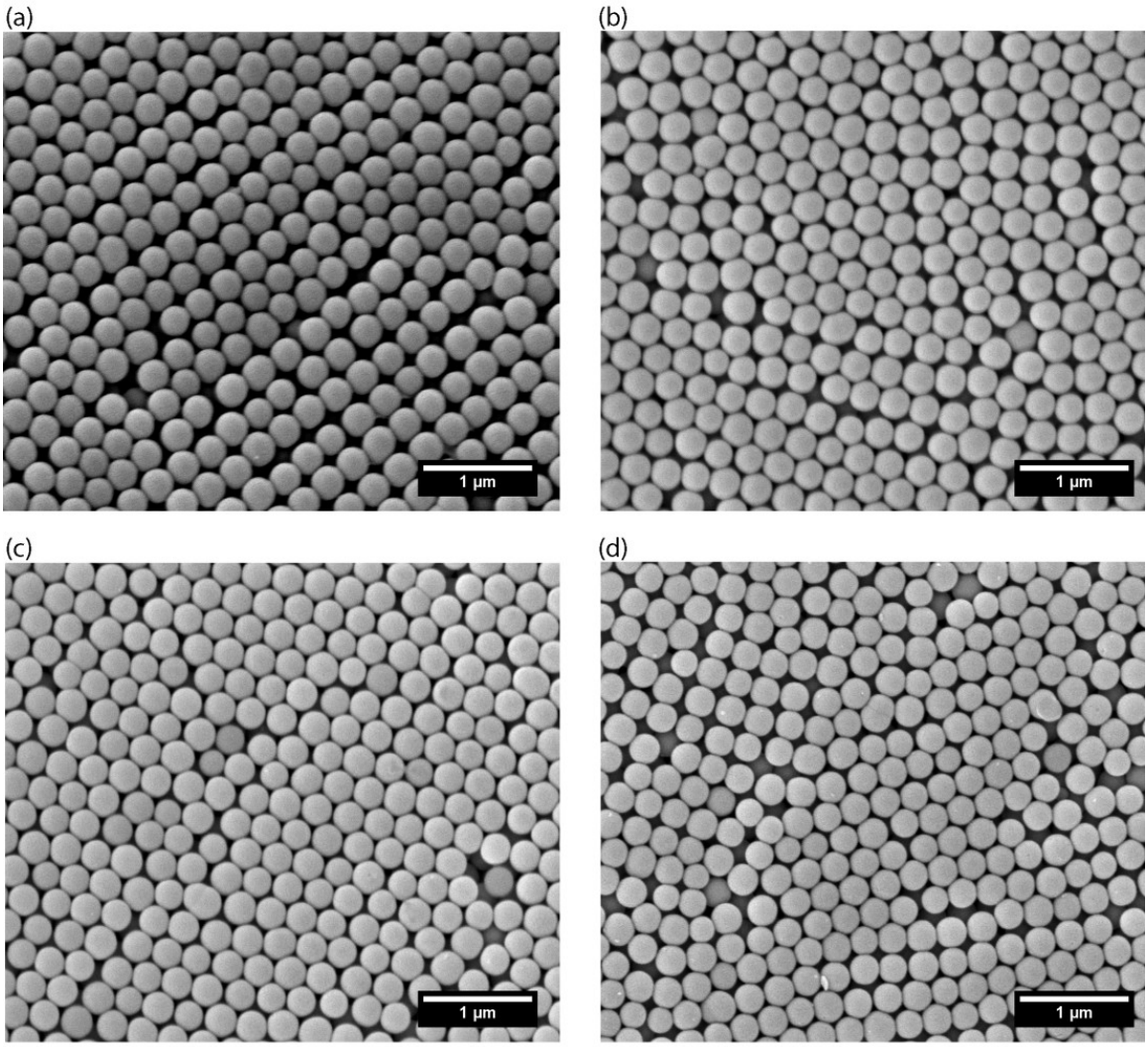

Figure 4.2. Scanning electron microscopy (SEM) images of silica particles (a) as–received and thermally treated at (b) 300 ^{o}C, (c) 600 ^{o}C and (d) 900 ^{o}C. Silica particles do not fuse for all thermal treatment temperatures.

Thermogravimetric analysis (TGA) is used to monitor the weight loss of silica particles with temperature. In Figure 4.3a, a TGA thermogram for Silica–1 particles used for the majority of this study shows a sharp weight loss between 0 and 200 ^{o}C due to dehydration – the removal of physisorbed water from the surface of silica.[99] The gradual weight loss

at temperatures above 200 ^{o}C is due to the dehydroxylation process – the removal of silanol groups from the surface by a condensation reaction in which siloxane bonds are formed.[26, 99] This TGA result suggests that the surface chemistry of silica changes with thermal treatment.

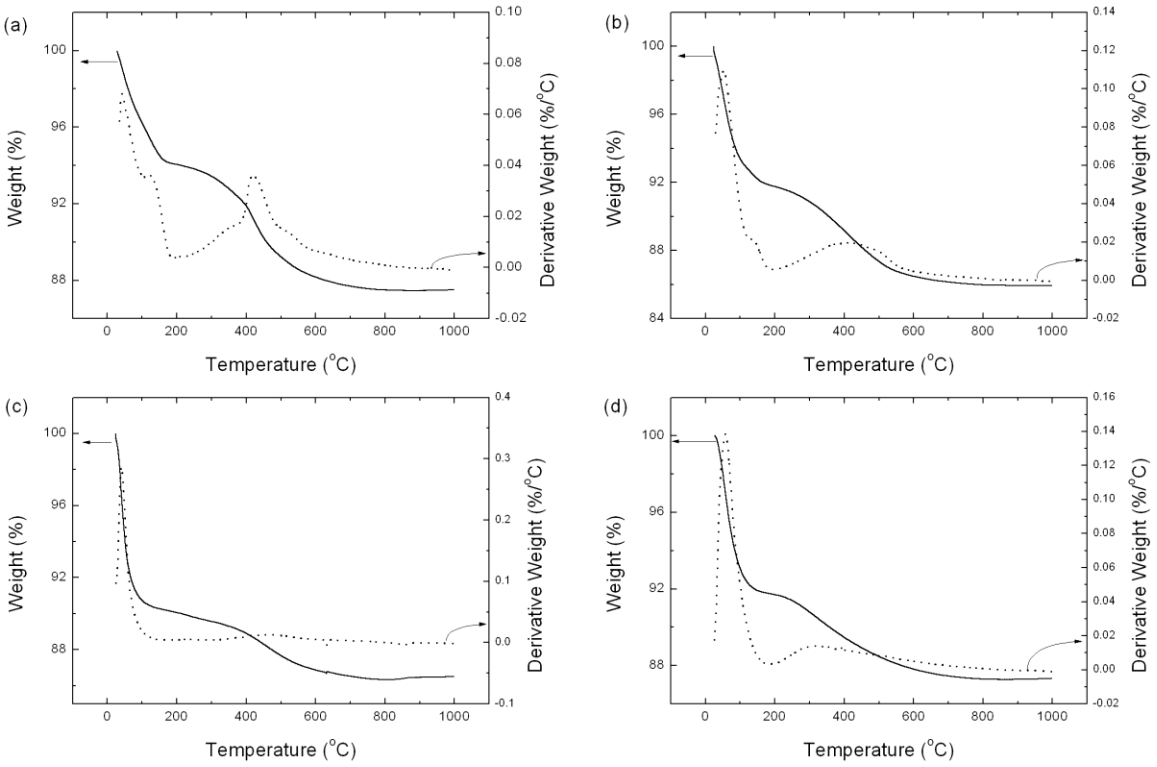

Figure 4.3. Weight loss of (a) Silica–1, (b) Silica–2, (c) Silica–3 and (d) Silica–4 particles as a function of temperature (solid line) as determined by thermogravimetric analysis (TGA). Dashed lines represent derivative of weight change with respect to temperature.

Fourier transform infrared (FTIR) spectroscopy is a useful technique for probing surface groups and has extensively been used to examine the surface chemistry of silica.[100, 101] FTIR is used in this study to confirm the changes in silica surface groups as a function of

thermal treatment temperature. The silica surface groups of interest in this study are physisorbed water, surface siloxane bonds, and isolated and bridged (or vicinal) silanol groups. Silanol groups present within the bulk structure of colloidal silica particles and inaccessible to external solutes are designated as internal silanol groups.[101] For as–received silica (i.e., fully hydroxylated with no thermal treatment), physisorbed water consists of multiple layers of water stabilized by a hydrogen–bond network.[99] Unstrained siloxane groups are relatively unreactive,[26] whereas the acidity of bridged and isolated silanol groups are known to differ; specifically, isolated silanol groups are more acidic (pK_a 4.5) than bridged silanol groups (pK_a 8.5), thus making them capable of dissociating more readily than bridged silanol groups.[102-104] The FTIR spectra in Figure 4.4a, shows that as thermal treatment temperature increases, the ~3680 cm^{-1} absorbance band, attributed to internal silanol groups diminishes. Likewise, the broad absorbance band between ~3620 – 3200 cm^{-1} (centered at ~3450 cm^{-1}) attributed to bridged silanol groups decreases with thermal treatment temperature.[101] Conversely, the sharp isolated silanol group peak at ~3745 cm^{-1} is initially absent but emerges at ~500 °C. Further examination of the isolated silanol peak shows a sharp increase in the normalized peak height between 500 and 700 °C followed by a gradual decrease (Figure 4.4b).

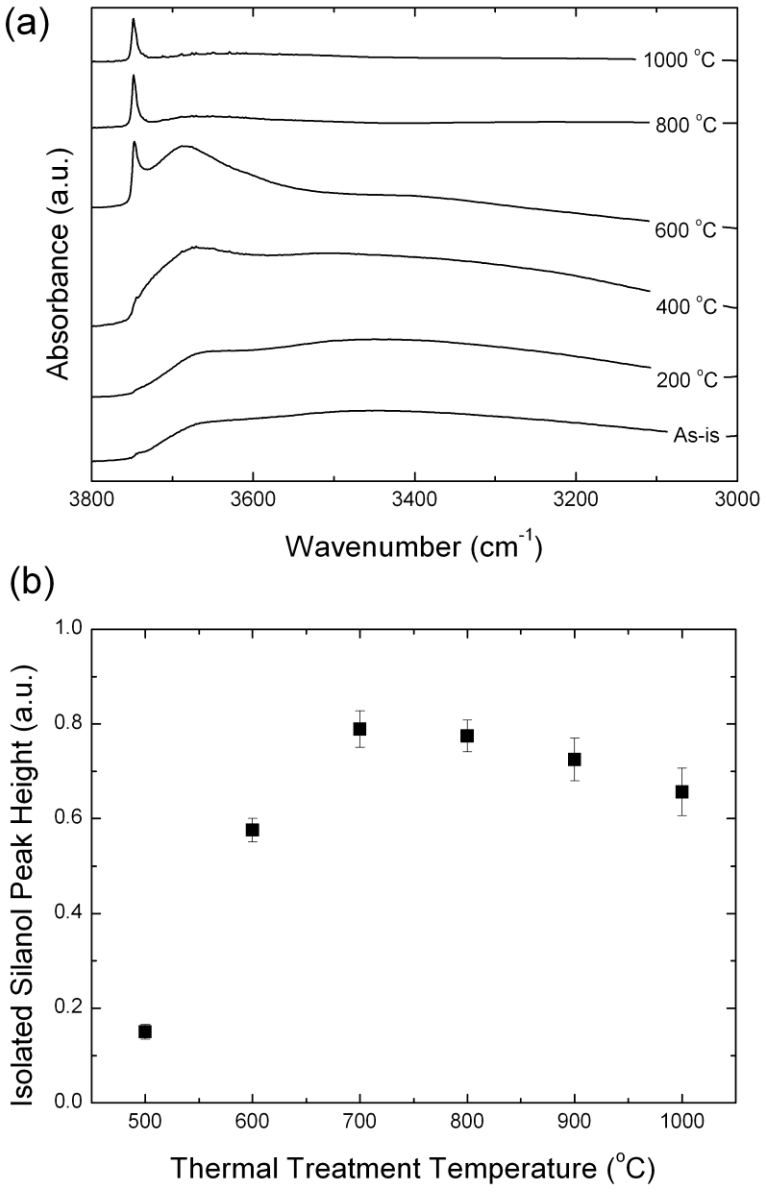

Figure 4.4. (a) Fourier transform infrared (FTIR) spectra of silica particles and (b) change in the normalized peak height of isolated silanol groups with thermal treatment temperature. Error bars represent standard deviation of six measurements.

Following the removal of physisorbed water, the effect of heat treatment on bridged silanol groups is the formation of siloxane bridges, isolated silanol groups and water vapor as a byproduct as shown in Figure 4.5. The overall effect is an initial increase in the number of isolated silanol groups as seen in Figure 4.4b. With further heat treatment, isolated silanol groups undergo a condensation reaction to form siloxane bridges and water, thus accounting for the eventual decrease in the isolated silanol peak height for temperatures greater than ~700 °C.[26] Isolated silanol groups are known to exist to some extent after thermal treatment, up to ~1200 °C.[99] The observed transitions with thermal treatment account for the TGA weight loss in Figure 4.3 and are consistent with previous reports that have examined the effect of heat treatment on silica surfaces.[26, 99, 105]

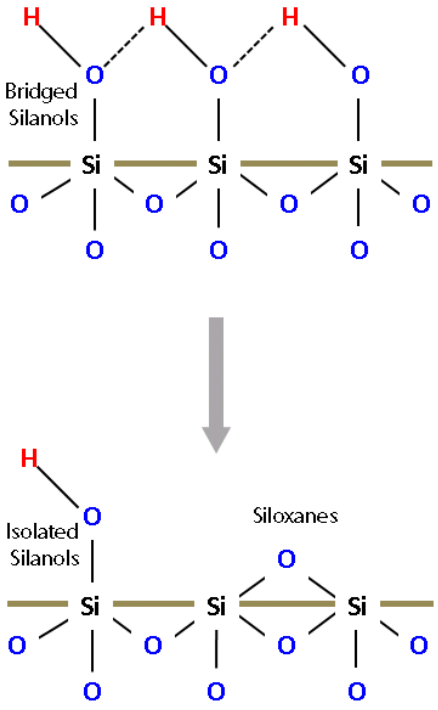

Figure 4.5. Effect of heat treatment on bridged silanol groups. Heat treatment leads to the formation of isolated silanol groups, siloxane bridges, and water as a by–product.

The electrophoretic mobility results shown in Figure 4.6 reveal that thermal treatment has a significant effect on the charge of silica particles in AOT/toluene. The non–monotonic change in electrophoretic mobility with thermal treatment temperature can be divided into three regions: (1) a slight charge increase from 0 to 200 °C, (2) a drastic charge decrease from 200 to 500 °C and (3) an increase in charge from 600 to 1000 °C. The sign of silica particle charge in AOT/toluene kept at low relative humidity is found to be negative for all three regions, which agrees well with the previously proposed acid–base interaction mechanism.[106, 107] This mechanism states that charging in non–polar media with a charge inducing agent is a result of ion exchange between particle surface groups and surfactant molecules. It was also proposed that for an acidic particle such as silica, uncharged AOT monomers adsorb on the surface followed by proton transfer from silanol surface groups to AOT. The charged AOT monomers subsequently desorb from the surface into AOT reverse micelles thus yielding a net negative surface charge.[82, 83] This acid–base interaction mechanism is particularly amenable to surfaces with dissociable groups[76] as is the case with thermally treated silica particles which have dissociable silanol groups present in the temperature range used in this study.

Three–phase contact angle (TPCA) measurements[108, 109] (Figure 4.7) of a water droplet on a planar silica surface in a continuous phase of pure toluene reveal that the surface remains hydrophilic (water contact angles in Figure 4.7 remain $< 90^{o}$) even after thermal treatment up to 1000 ^{o}C. This result has an important implication; one of the proposed mechanisms for the origin of particle charge in non–polar media in the presence of AOT is based on the preferential partitioning of cations and anions between the

particle surface and AOT reverse micelles in solution.[110, 111] Based on this mechanism, hydrophilic particles such as silica are expected to gain a net positive charge due to the preferential adsorption of the sodium cation of AOT over that of the sulfosuccinate anions.[110] Such a mechanism is not consistent with our observations because the surface of silica remains hydrophilic throughout the temperature range used in this study.

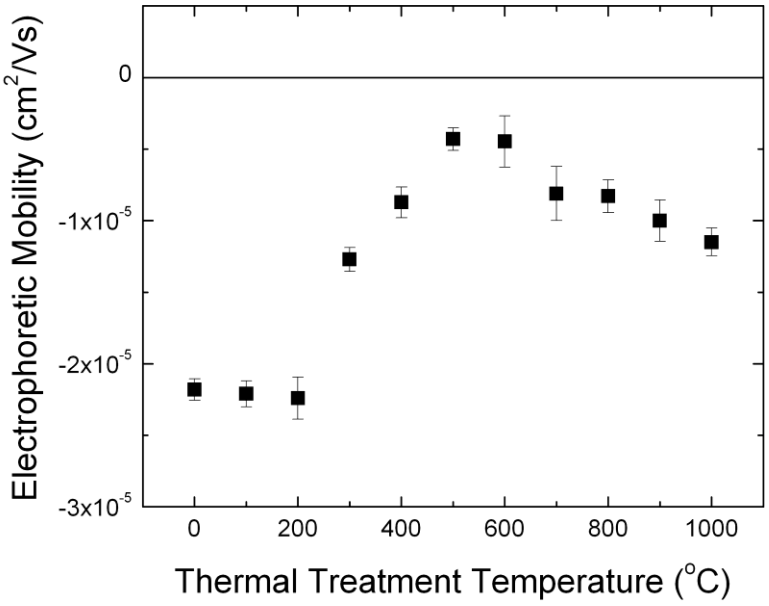

Figure 4.6. Electrophoretic mobility of silica particles thermally treated at various temperatures. Silica dispersions are prepared in 10 mM AOT/toluene and are kept at a low relative humidity (11% RH) for 15 – 18 hrs. Error bars represent standard deviation of six measurements.

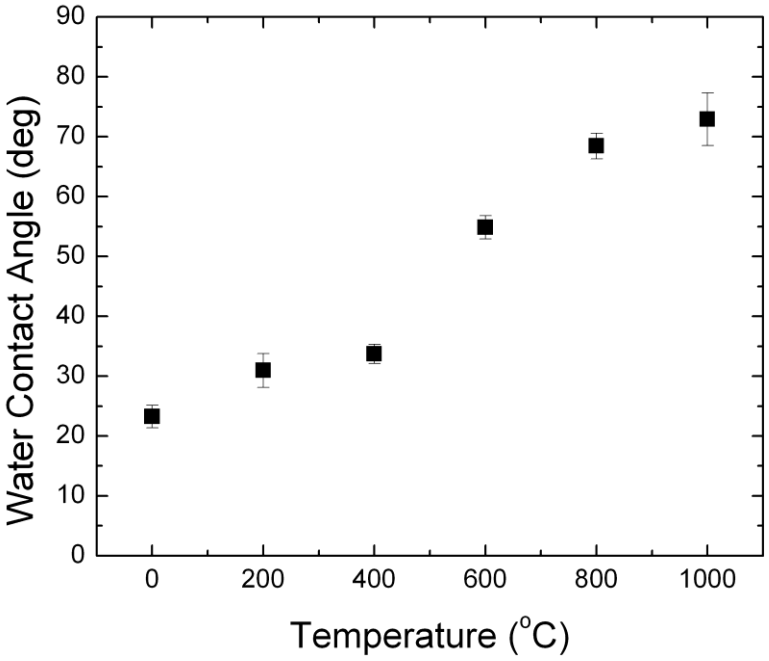

Figure 4.7. Three–phase contact angle measurements of planar silica surface thermally treated at different temperatures. Error bars represent standard deviation for four separate samples.

A prior study showed that the adsorption behavior of surfactant correlates well with the charge behavior of particles.[112] In our system, changes in the surface chemistry of silica with thermal treatment could result in changes in the adsorption behavior of AOT monomers and micelles, which, in turn, affects the charge state. In addition to these differences in the interactions between silica surface and AOT, the ionization of the silica surface is dependent on the surface groups present. In fact, there exist some correlation between surface groups present (Figure 4.4) and the charging behavior of thermally treated silica particles shown in Figure 4.6. For example, the charge decrease between 200 and 600 °C is attributed to the loss of bridged silanol groups that dominate the surface. These silanol groups, likely participate in particle charging through acid–base

interactions with adsorbed AOT,[83] therefore resulting in a corresponding charge decrease as they diminish. This result agrees well with a previous study, in which the charge of alumina suspended in OLOA/toluene was found to decrease after calcination at 800 ^{o}C.[90] This behavior was attributed to the removal of surface hydroxyl groups during calcination.

Silica particles thermally treated above 600 ^{o}C, however, show a peculiar charge increase. A possible explanation for this behavior is as follows. As previously mentioned, isolated silanol groups are more acidic (i.e., lower pK_a) and reactive than bridged silanol groups;[102-104] hence, these groups would readily donate protons to adsorbed AOT monomers via acid–base interactions. The charge of silica particles would therefore increase as the fraction of isolated silanol groups (i.e. the ratio of isolated silanol groups to bridged silanol groups) increases above 600 ^{o}C. In fact, thermal treatment for times greater than 6 hours has little effect on the fraction of isolated silanol groups on the surface as well as the charge of silica particles in 10 mM AOT/toluene at a low relative humidity (Figure 4.8). This result suggests that a majority of the change in surface groups of silica takes place within the first 6 hours. This proposed mechanism, however, does not fully describe the observed trend because the isolated silanol group concentration eventually decreases above 700 ^{o}C but the charge nevertheless increases. The exact mechanism of this charge increase above 600 °C warrants further study. One possible approach is to correlate the point of zero charge (PZC) or isoelectric point (IEP) of thermally treated silica in water to their electrophoretic mobility in AOT/toluene.[83, 113] However, such an approach presents some challenges since for thermally treated silica,

PZC and IEP measurements have to be performed in an aqueous phase, which could result in a different surface state (e.g., hydration state) compared to thermally treated silica in AOT/toluene.

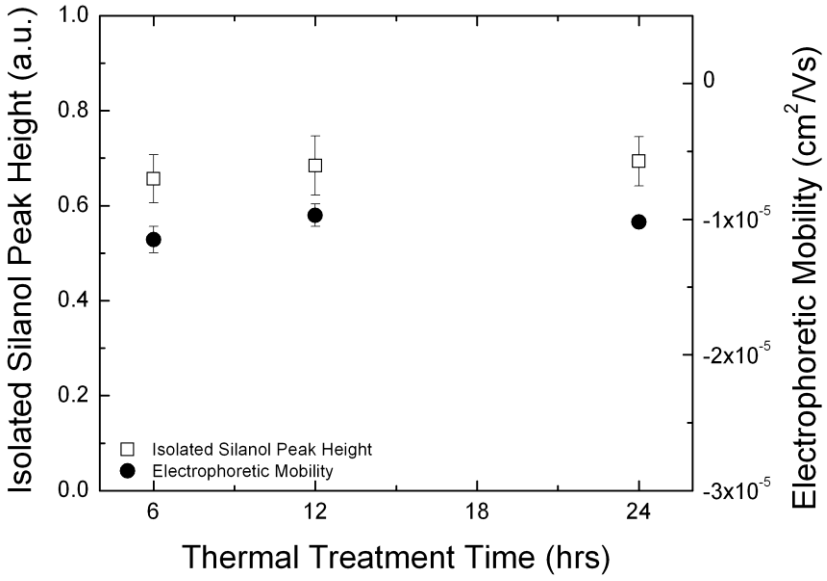

Figure 4.8. Change in normalized isolated silanol group peak height (left axis) and electrophoretic mobility of particles in 10 mM AOT/toluene stored at low relative humidity (right axis) with particle thermal treatment (1000 ^{o}C) time.

4.3.2 Effect of Water on Particle Charge

In addition to examining the role of surface groups on the charge of silica, this study also examine the effect of moisture on particle charging. In non–polar media such as toluene, ambient conditions such as relative humidity can result in water levels of hundreds of parts per million (ppm), which could possibly play a role in the inconsistent charge characteristics of silica previously observed. In reality, colloids are seldom used under completely dry conditions, and thus, relative humidity could also have a significant

impact on practical applications of charged particles in non–polar media.[71] In addition, the charge–inducing agent and the particles themselves could carry small traces of water. The first step taken to understand the effect of relative humidity on particle charge involves examining its effect on solution properties. To control the amount of water in non–polar media, silica dispersions are stored at low (11%), medium (47%) and high (69%) relative humidities for 15–18 hours. Moisture content as measured by Karl Fischer titration reveals that the concentration of water does not significantly change after ~15 hours (Figure 4.9); thus, storing dispersions at each relative humidity for 15–18 hours results in reproducible water content for each condition.

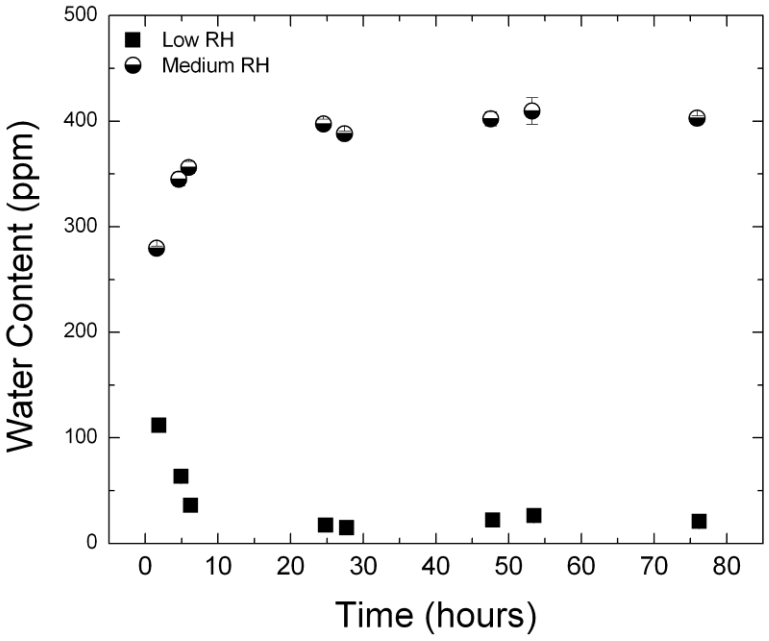

Figure 4.9. Temporal change in water content of 10 mM AOT/toluene solution stored at low (11%) and medium (47%) relative humidity

As shown in Figure 4.10a, water content increases with [AOT] which is a result of the hygroscopic nature of AOT.[69, 114] The molar ratios of water and surfactant, W_o = $[H_2O]/[AOT]$, obtained based on the results in Figure 4.10a, reveal that there is relatively small change in water content due to the presence of silica particles as summarized in Table 4.1. Instead, the amount of water present in dispersions is dominantly determined by the partitioning of water vapor from atmosphere into solution. The solution conductivity increases linearly with [AOT] for a fixed relative humidity as shown in Figure 4.10b. This result is consistent with the behavior of AOT above its critical micelle concentration (CMC)[73] and has been attributed to the spontaneous disproportionation of neutral micelles to charged micelles ($2M^o \leftrightarrow M^+ + M^-$) which contribute to solution conductivity.[44, 69, 115] AOT reverse micelles are also known to swell with increasing moisture content.[116] The increase in solution conductivity (σ) and hydrodynamic radius (r_h) of AOT reverse micelles with relative humidity implies that the fraction of charged micelles (χ) increases since χ is directly proportional to the solution conductivity (σ) and hydrodynamic radius (r_h) of AOT reverse micelles (i.e. $\chi \sim \sigma r_h$).[44, 69, 115]

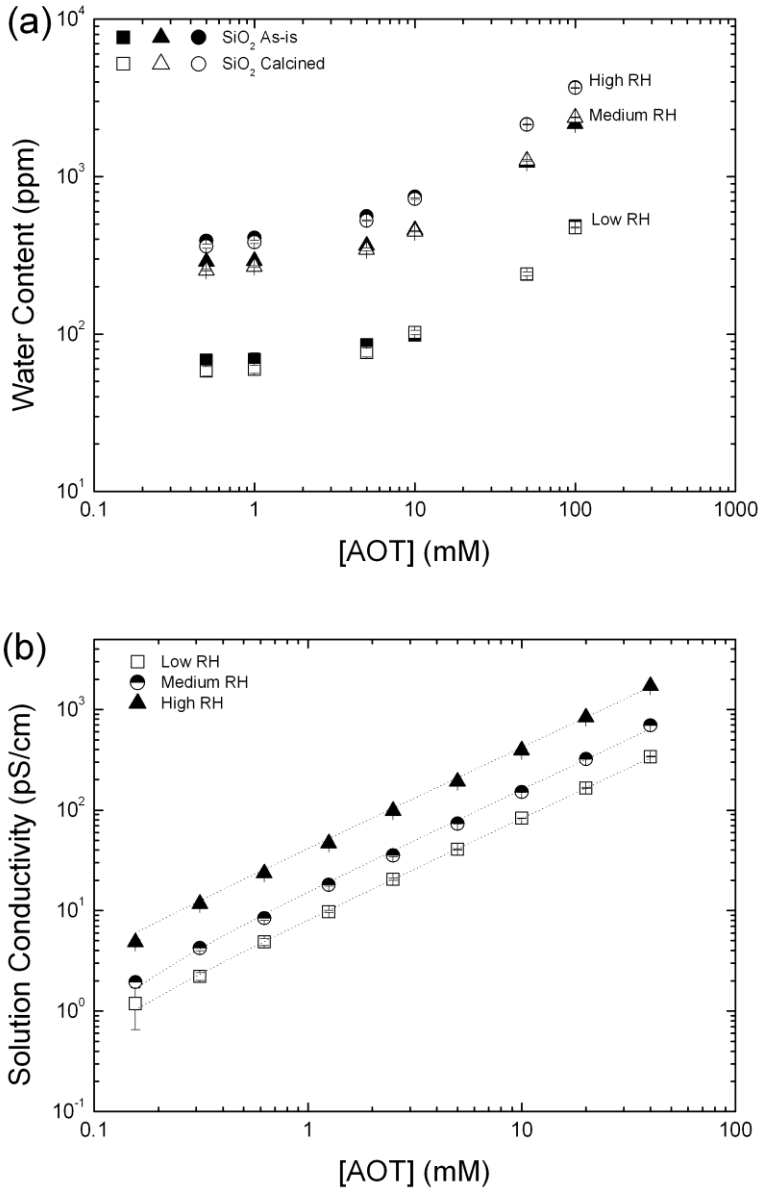

Figure 4.10. Change in AOT/toluene (a) water content (in ppm) and (b) solution conductivity with respect to concentration of AOT ([AOT]) for three different relative humidities – low (11%), medium (47%) and high (69%). Error bars represent standard deviation of three measurements.

Table 4.1. Molar ratio of water to surfactant (W_o) for solutions at low, medium and high relative humidities.

Relative Humidity (RH)	W_o	
	No silica particles	As–received silica particles
Low (11% RH)	0.0064	0.0081
Medium (47% RH)	0.0305	0.0370
High (69% RH)	0.0694	0.0649

As–received silica dispersions with various concentrations of AOT are prepared and kept at low, medium and high relative humidities. The electrophoretic mobility (Figure 4.11) reveals that the moisture content as controlled by relative humidity has an enormous effect on the silica particle charge. Figure 4.11 shows that the magnitude of the electrophoretic mobility of silica particles is characterized by a maximum value with increasing [AOT], which is consistent with observations made in previous studies.[74, 82, 83, 117] The initial rise in the magnitude of electrophoretic mobility is a result of an increase in acid–base interactions between silica and AOT, whereas the gradual decrease towards zero has been attributed to charge screening by charged micelles formed through the spontaneous disproportionation process.[69, 75, 82, 118, 119] Figure 4.11 reveals that for all concentrations of AOT, the magnitude of electrophoretic mobility of silica particles decreases with increasing relative humidity. This behavior can be explained by charge screening dominating surface charging.[92] The charge screening effect increases as the

fraction of charged micelles χ increases with relative humidity as discussed in the previous section. As the electrophoretic mobility of particles decreases, weak repulsive electrostatic interactions results in particle flocculation as shown by the particle size increase in Figure 4.12a. A similar effect also occurs for thermally treated particles as shown in Figure 4.12b.

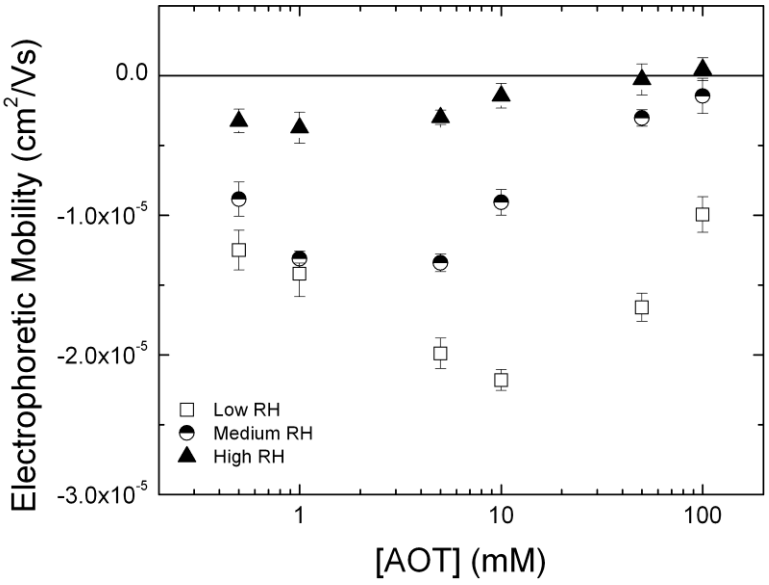

Figure 4.11. Electrophoretic mobility of silica particles for different concentrations of AOT and relative humidities.

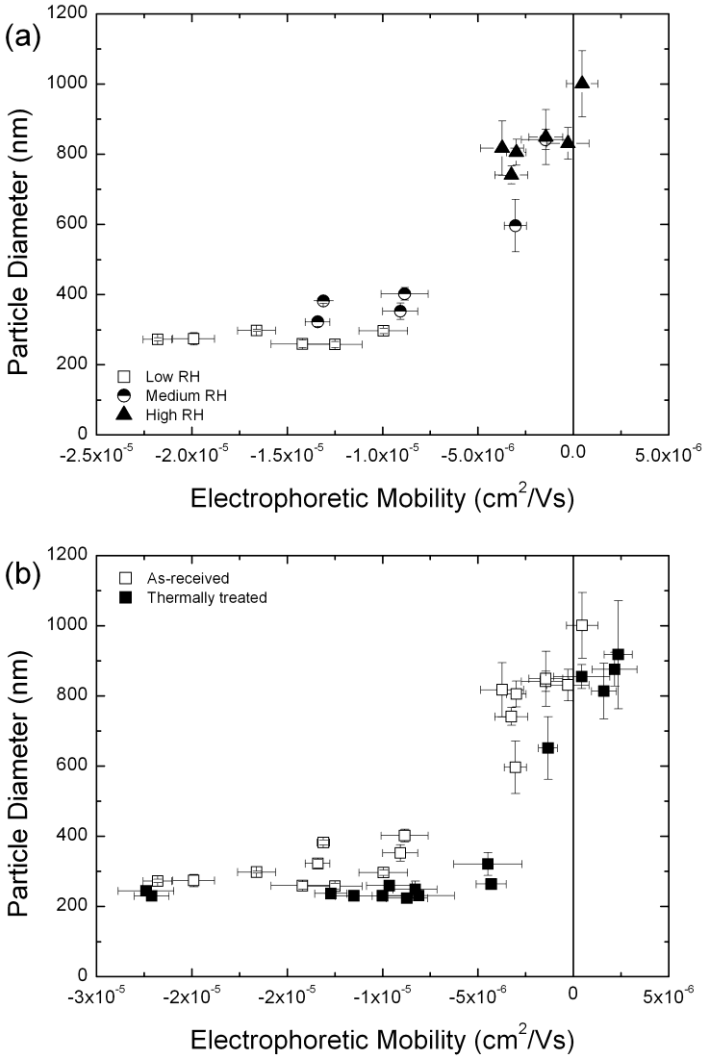

Figure 4.12. (a) Change in particle size with electrophoretic mobility and (b) Change in silica particle size with electrophoretic mobility for as–received and thermally treated samples. Error bars represent standard deviation of six measurements.

Quartz crystal microbalance with dissipation (QCM–D) is used to further investigate the origin of decreasing surface charge with relative humidity. This is achieved by measuring the adsorption of water and AOT present in toluene onto a silica–coated quartz crystal surface. The QCM result with silica–coated quartz crystal is expected to provide

important insights into the interaction between AOT (or water) and silica surfaces, although the absolute amount of AOT or water molecules interacting with silica–coated quartz crystal surface may be different from that interacting with the particle surface.

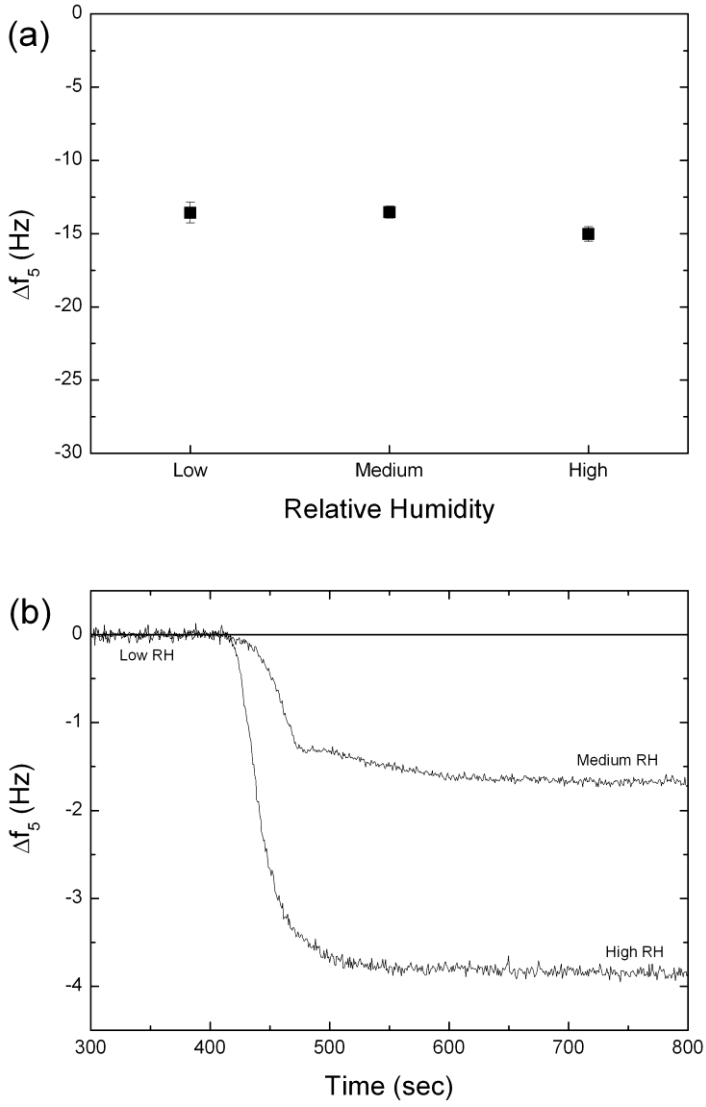

Figure 4.13. Quartz crystal microbalance (QCM) frequency shifts (Δf_5 : 5th overtone) for adsorption of 100 mM AOT/toluene solution (a) at low, medium and high relative humidities from a baseline in pure toluene at the same relative humidity and (b) at medium and high relative humidities from a baseline in 100 mM AOT/toluene at a low relative humidity solution. Error bars in (a) represent standard deviation of three measurements.

The standard output of a QCM is a frequency shift (Δf) proportional to mass increase on the QCM crystal surface. A baseline in pure toluene stored at low, medium or high relative humidity is obtained, after which the solution is exchanged for 100 mM AOT/toluene at the same relative humidity. The frequency shifts shown in Figure 4.13a arise from the adsorption of AOT onto the surface of the silica–coated quartz crystal. The frequency shift for all three conditions is comparable, which implies that similar amount of AOT adsorbs on the silica surface regardless of the moisture content present in solution. In Figure 4.13b, a baseline in 100 mM AOT/toluene kept at low relative humidity is first obtained after which the solution is exchanged for 100 mM AOT/toluene kept at either medium or high relative humidity. The frequency shift ($-\Delta f_5$) of ~4 Hz seen for the high relative humidity solution reveals that more water adsorbs on the silica surface at this condition compared to the medium relative humidity solution with a $-\Delta f_5$ of ~1.7 Hz. Based on these results, it can be inferred that water adsorbing on the silica surface results in the formation of a hydration layer. Therefore, in addition to the charge screening effect by charged micelles, the formation of a hydration layer on the as–received silica surface could also diminish charge through a decrease in acid–base interactions with adsorbed AOT. Furthermore, a previous study has suggested that adsorbed water phase could form bridges between particles resulting in flocculation.[91] This could also contribute to particle flocculation with increasing moisture content as seen in Figure 4.12.

The effect of moisture on the electrophoretic mobility of thermally treated silica is also probed in this study. The charge of thermally treated samples at medium and high

relative humidity (Figure 4.14) is found to change in a similar manner to samples at a low relative humidity. For as–received and 200 ^{o}C thermally treated samples, the charge becomes less negative with increasing relative humidity. However, for higher thermal treatment temperatures, the charge of particles reverses from negative to positive for medium and high relative humidity samples. It is quite possible that this charge reversal is a result of a change in the acidity of silica particles due to adsorbed water.

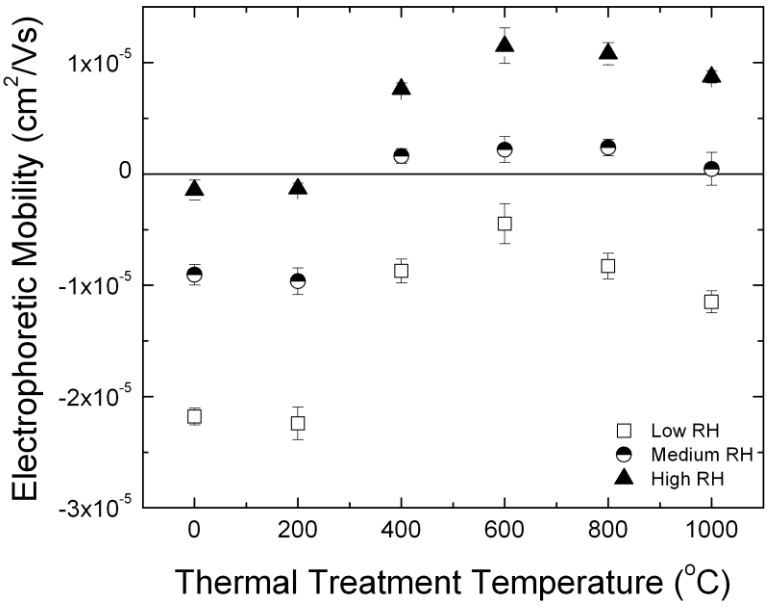

Figure 4.14. Electrophoretic mobility of silica particles in 10 mM AOT/toluene thermally treated at different temperatures. Particle dispersions are stored at low, medium and high relative humidity.

It has been proposed previously that the addition of water to alcohols, which are relatively polar media, makes the surface of oxides such as rutile titania and alumina more basic and therefore makes these particles more positively charged; however, to the best of knowledge, this hypothesis has not been confirmed experimentally thus far.[120] To

test this hypothesis, the Hammett indicator method, which has been used to probe the acidity of solid surfaces in non–aqueous solutions is used.[121] For both as–received and thermally treated silica particles, a change in the color of adsorbed indicator, methyl red, from an acid red color to a more basic orange color with increasing moisture content in the media is observed as shown in Figure 4.15.

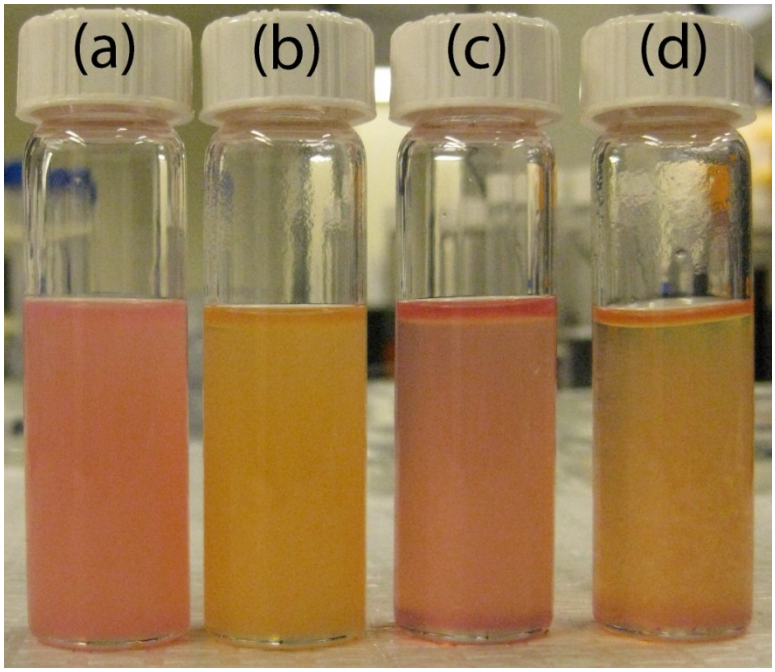

Figure 4.15. Methyl red dye indicator test for as–received silica particles at (a) low and (b) high relative humidity, and for 1000 ^{o}C thermally treated silica particles at (c) low and (d) high relative humidity.

For the system used in this study, this change in the surface acidity for silica particles with isolated silanol groups present (particles thermally treated at 400 ^{o}C and above), results in a positive surface charge. This is a result of the relative acidities of the silica surface and AOT changing such that the surface becomes an electron donor during acid–

base interactions with AOT. The results obtained above have important implications; the charging behavior of silica after thermal treatment and storage under different relative humidity conditions suggests that the sign of silica charge in non–polar media doped with AOT is highly dependent on surface chemistry and moisture content. The surface chemistry of silica, in particular, the relative ratio of bridged and isolated silanol groups, could change depending on synthetic procedures used during manufacture. Furthermore, the amount of water in the particle dispersion depends strongly on the relative humidity of the ambient environment. These observations could shed some light onto the origin of conflicting results previously reported.

Measurements of the electrophoretic mobility of as–received colloidal silica particles from different suppliers in 10 mM AOT/toluene solution[§] stored at a low relative humidity show some discrepancies in the magnitude of their charge. The origin of this discrepancy can be explained by using the newly gathered understanding on the role of moisture on particle charge. In Figure 4.16, physisorbed moisture content as determined by thermogravimetric analysis (TGA)[95-97] (Figure 4.3) is plotted against the electrophoretic mobility of particles in 10 mM AOT/toluene at a low relative humidity. From this plot, it is evident that there is a strong correlation between physisorbed water content and electrophoretic mobility such that particle charge decreases with increasing physisorbed water content. This result agrees well with QCM measurements (Figure 4.13) and suggests that physisorbed water on the surface of as–received silica indeed has

[§] An AOT concentration of 10 mM is used since this yields the maximum value in the magnitude of electrophoretic mobility for Silica-1 at a low relative humidity.

an adverse effect on charge. The removal of physisorbed water could also explain the slight increase in electrophoretic mobility for silica thermally treated between 0~200 ^{o}C (Figure 4.6). The effect of the total concentration of surface hydroxyl groups (the silanol number) can be neglected since this has been reported to be a physicochemical constant (~4.9 OH groups nm^{-2}) independent of the origin or structural characteristics of amorphous silica.[122]

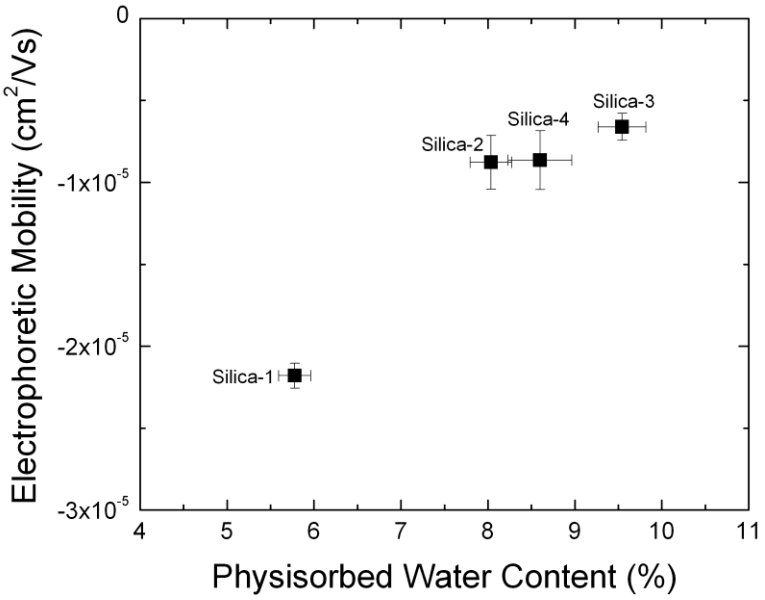

Figure 4.16. Change in electrophoretic mobility with physisorbed water content for silica particles from four different suppliers in 10 mM AOT/toluene stored at a low relative humidity. Error bars represent standard deviation of six measurements for electrophoretic mobility and three measurements for water content.

4.4 Conclusions

In conclusion, thermal treatment of silica particles and relative humidity is shown to have a significant effect on the charge of particles in AOT/toluene. The effect of thermal treatment is a non–monotonic change in the charge of silica. This behavior is attributed to changes in the type and fraction of surface silanol groups. The charge of as–received silica particles is also found to decrease with increasing moisture content. This possibly occurs as a result of the formation of a hydration layer on the surface of silica as observed with QCM. Furthermore, increasing moisture content reverses the charge of dehydroxylated silica from negative to positive. Adsorbed water is found to make the surface of as–received and dehydroxylated silica more basic; however, the exact mechanism of charge reversal warrants further study. The effect of physisorbed water content of as–received particles from different suppliers is also found to have an effect on their charge in the same solution condition. The results obtained emphasize the importance of carefully controlling the surface chemistry and water content in particle dispersions in order to enhance the reproducibility of electrophoretic mobility measurements in non–polar media. Furthermore, these parameters, in addition to the concentration of the charge–inducing agent, provide a new way to control the charging of colloids in non−polar media.

Chapter 5. Effect of Relative Humidity on Layer–by–Layer Assembly of Oppositely Charged Particles in Non–Polar Media

5.1 Introduction

The study presented in *Chapter 3* showed that the charge of particles (as controlled by the concentration of AOT) could be used to tune the growth of LbL assembled films. In *Chapter 4*, it was shown that water content in SiO_2 dispersions in AOT/toluene (as controlled by ambient relative humidity), has a significant effect on the charge of SiO_2. In fact, the charge of SiO_2 reversed under certain conditions. Based on this result, it is quite plausible that relative humidity will also have an effect on the growth of LbL assembled films. In fact, the quality of the LbL assembled films made using carbon black and Al_2O_3 particles in AOT/toluene (*Chapter 3*) has been seen to depend on the season in which the assembly is performed (i.e., summer vs. winter).

The goal of the study covered in this chapter, therefore, is to bridge the findings in *Chapters 3* and *4* by exploring the effect of relative humidity (RH) on the LbL assembly process in non–polar solvents. The carbon black and Al_2O_3 particles dispersed in AOT/toluene are used as a model system and the ambient RH of the LbL assembly chamber is set to three different values, ~ 12 %, ~ 42 % and ~ 62 %. It will be shown that RH increases the water content of particle dispersions in AOT/toluene, which in turn significantly changes the charge of carbon black and Al_2O_3 particles as well as the growth

behavior of LbL assembled films. The results gathered emphasize the importance of controlling ambient RH for non–polar LbL assembly and suggest that RH could be used as an additional parameter to control the non–polar LbL assembly process.

5.2 Experimental Section

5.2.1 Materials

Al_2O_3 (SpectrAl 100) and carbon black (Conductex 7055 Ultra) are obtained from Cabot and Columbian Chemicals, respectively. The nitrogen surface area (NSA) of carbon black (CB) and Al_2O_3 are 55 and 95 m^2/g, respectively, as provided by the manufacturers. Both particles are used as received. De–ionized (DI) water (18.2 MΩ–cm) is generated from a Barnstead Nanopure system (Thermo Scientific). Toluene, NaCl, NaOH, K_2CO_3, Drierite® and plain microscope glass slides are purchased from Fisher Scientific while Aerosol–OT (AOT), is purchased from Sigma–Aldrich. Drierite® is used to fix the relative humidity (RH) at ~ 12 % (low) while saturated salt solutions of K_2CO_3 and NaCl are used to fix the RH at ~ 42 % (medium) and ~ 62 % (high), respectively.[98]

5.2.2 Preparation of Al_2O_3 and CB Dispersions in AOT/toluene

200 mM of AOT in toluene is prepared and diluted to 100, 20, 10, 2 and 1 mM AOT/toluene solutions. 0.1 wt. % Al_2O_3 and CB suspensions are prepared in pure toluene and sonicated for 1 hour to obtain fine suspensions. A set volume of each particle

suspensions is vigorously shaken to disperse the particles, and then mixed with an equal volume of each AOT/toluene solution to yield 0.05 wt. % Al_2O_3 or CB dispersions in AOT/toluene. A lower particle weight fraction (0.005 wt %) is used for CB electrophoretic mobility measurements in order to get a good intensity reading. Both dispersions are subsequently sonicated for 1 hour and stored overnight in a desicator at a fixed relative humidity.

5.2.3 Layer–by–Layer Assembly of CB and Al_2O_3 in Toluene

LbL assembly is performed on glass slides, which are cleaned by sonicating in 1.0 M NaOH for 20 min, thorough rinsing in DI water and drying with compressed air. 0.05 wt % CB and Al_2O_3 dispersions in AOT/toluene to be used for LbL are prepared and sonicated for 1 hour. The first LbL rinse bath consists of 60 mL of AOT/toluene at the same AOT concentration as the particle dispersion used. The remaining rinse baths consists of 60 mL of pure toluene. LbL assembly is performed with a StratoSequencer VI spin dipper (NanoStrata Inc.). The dipper has an enclosed chamber in which the particle dispersions and rinse solutions are kept for ~ 24 hours at a fixed RH. Following this time, the dispersions are sonicated for 20 min to be used immediately for LbL. Fabrication of one bilayer involves exposing a glass slide to 0.05 wt. % CB in AOT/toluene, AOT/toluene rinse, two pure toluene rinse steps followed by 0.05 wt. % Al_2O_3 in AOT/toluene, AOT/toluene rinse, and two pure toluene rinse steps. The LbL dipper is programmed to expose glass slide substrates to particle dispersions for 10 min followed by 2, 1, and 1 min rinse steps.

5.2.4 Particle Dispersion and LbL Film Characterization

The water content of solutions and dispersions is measured with a coulometric Karl Fischer titrator (Denver Instruments model 275KF). Electrophoretic mobility and particle size measurements are performed with a Beckman Coulter Delsa Nano–C. Six electrophoretic mobility measurements are made for each suspension using a flow cell at an electric field of 85.2 V/cm while three size measurements are made using a standard quartz cuvette. UV–Vis absorbance measurements are performed using a Cary 5000 (Varian Inc.) UV–Vis–NIR spectrophotometer. The absorbance at 500 nm is used for all data analysis. Scanning electron microscopy (SEM) images are taken using an FEI 600 Quanta FEG ESEM at 5 kV and at a working distance of 10 mm. Film thickness measurements are obtained using a Zygo NewView 6K series optical profilometer. A small scratch is made on the film in order to use the exposed glass substrate as a reference height. The height profile on either side of the scratch (Figure 5.1a) is integrated and normalized with the profile length to get an average film thickness. This procedure is repeated along six random line segments for each film sample. The height obtained by optical profilometry is found to be consistent with cross–sectional SEM images shown in Figure 5.1b.

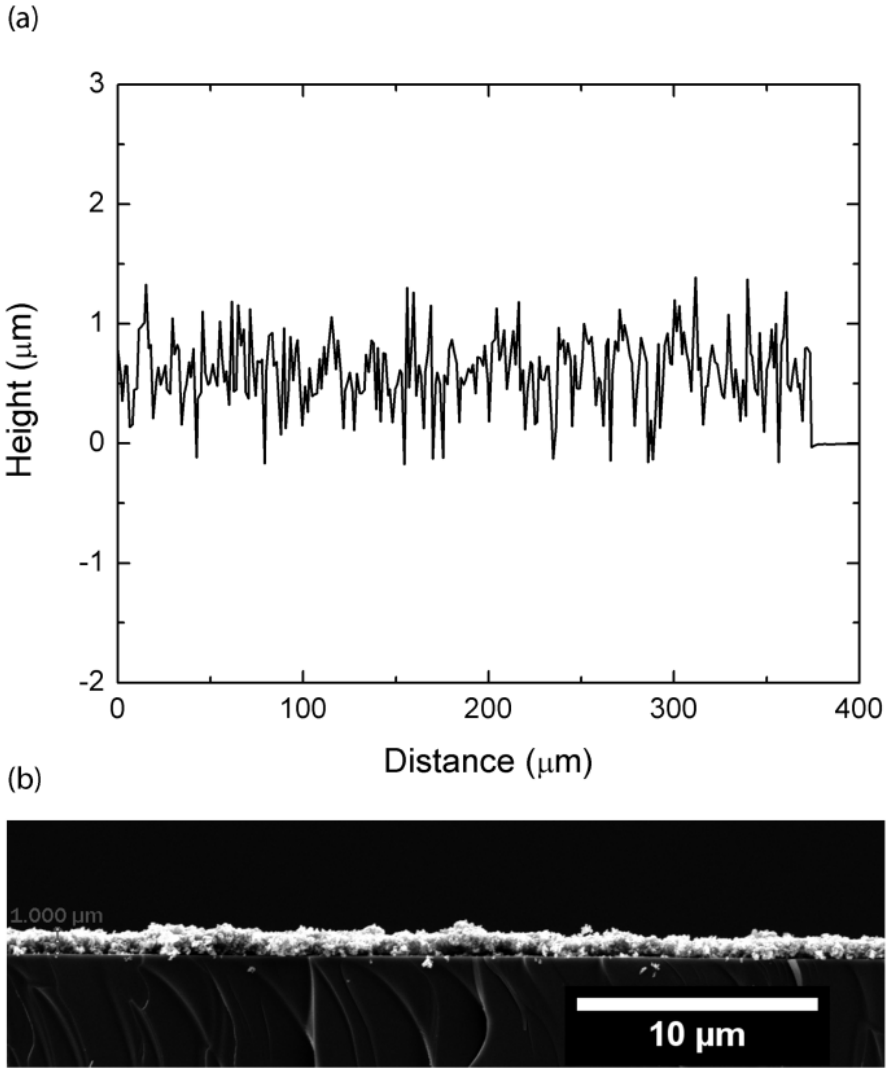

Figure 5.1. (a) Optical profilometry height profile and (b) cross–section scanning electron micrograph of CB/Al_2O_3 film assembled at 1 mM AOT and low relative humidity (primer layer).

5.2.5 Quartz Crystal Microbalance (QCM) Measurements

Silica–coated QCM crystals (Q–Sense) are cleaned by immersing in 2 wt % sodium dodecyl sulfate (SDS) solution followed by rinsing with DI water, drying with nitrogen and oxygen plasma treatment. Frequency shift measurements are performed with a Q–Sense E4 quartz crystal microbalance with dissipation monitoring (QCM–D). A flow rate

of 200 μL/min, controlled by a Harvard Instruments syringe pump (model PhD Ultra), is used for all measurements. AOT/toluene solutions and particle dispersions are kept in desiccators at the desired relative humidity during measurements to avoid any change in the water content. A baseline in AOT/toluene is first obtained before depositing Al_2O_3 or CB on the QCM crystal. All frequency shifts reported are from the fifth overtone (Δf_5).

5.3 Results and Discussion

5.3.1 Effect of Relative Humidity on Solution Moisture Content

This study begins by examining the effect of relative humidity (RH) on the water content of toluene doped with AOT (AOT/toluene) as exemplified by 100 mM AOT/toluene solutions. These AOT/toluene solutions are kept in an LbL chamber at three different RHs: low RH (~ 12 %) fixed with a desiccant Drierite®, medium RH (~ 42 %) fixed with a saturated K_2CO_3 salt solution, and high RH (~ 62 %) fixed with a saturated NaCl salt solution. Karl Fischer titration is used to measure the water content of solutions at different time points. Figure 5.2 shows that the water content of AOT/toluene solutions indeed changes with the LbL chamber RH as well as with time.

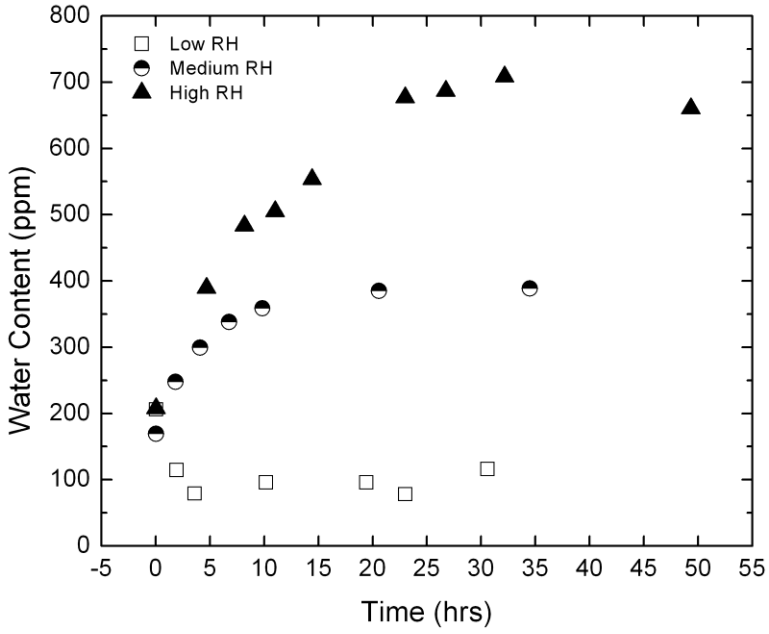

Figure 5.2. Temporal change in water content of 100 mM AOT/toluene solutions kept at low (~ 12 %), medium (~ 42 %) and high (~ 62 %) relative humidity.

Despite the significant fluctuations in the ambient lab RH with time, the RH within the LbL chamber containing drierite or saturated salt solutions is found to stabilize after ~ 5 hours as shown in Figure 5.3. However, Figure 5.2 shows that it takes ~ 24 hours for the water content of 100 mM AOT/toluene solutions kept at medium and high RH to reach a steady value. The water content of AOT/toluene solutions is found to be higher than pure toluene for all RHs due to the hygroscopic nature of AOT as shown in Figure 5.4.[69] The addition of particles, as exemplified by Al_2O_3 added to 100 mM AOT/toluene, results in a modest increase in the water content of dispersions kept at a low RH, and has a negligible effect on the water content of dispersions kept at medium and high RH as shown in Figure 5.4. In short, these results strongly indicate that water is mostly introduced into dispersions by AOT and partitioning of ambient water vapor into solution.

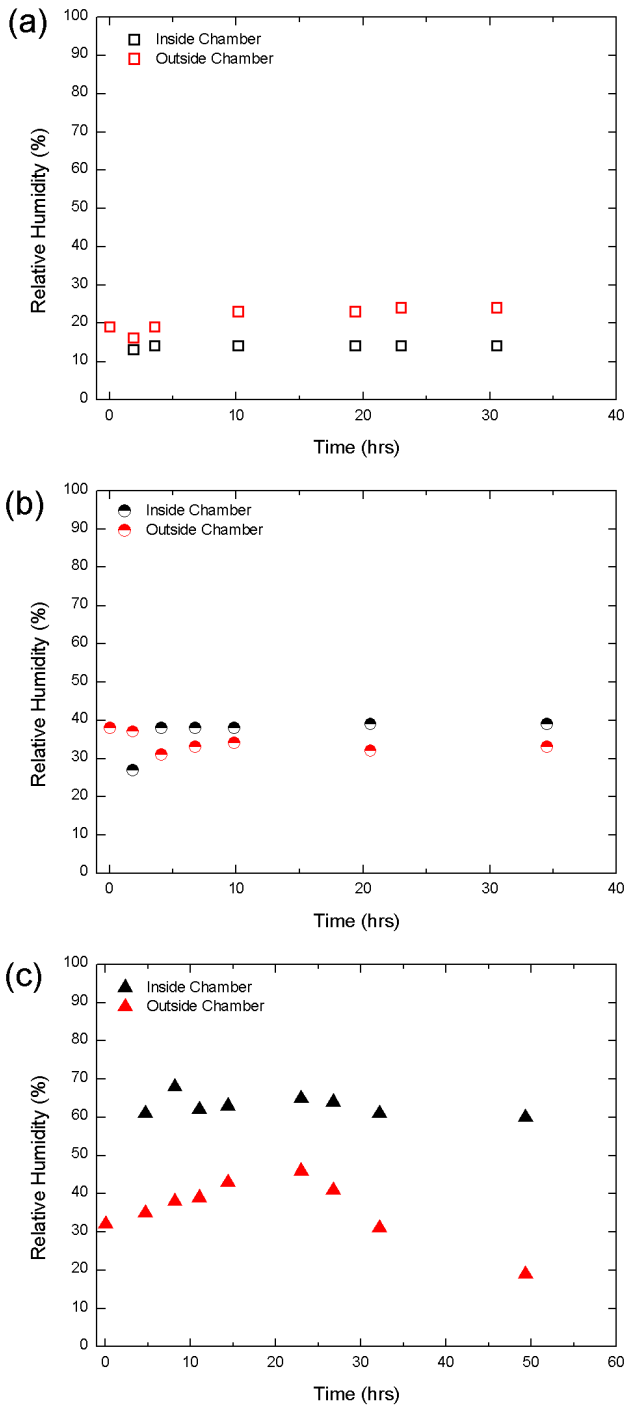

Figure 5.3. Temporal change in relative humidity inside (black symbols) and outside (red symbols) LbL chamber. The humidity inside the LbL chamber is fixed at (a) low (~ 12 %), (b) medium (~ 42 %) and (c) high (~ 62 %) relative humidity. The measured relative humidity outside the chamber differs for each run and with time due to constant fluctuations in ambient lab relative humidity.

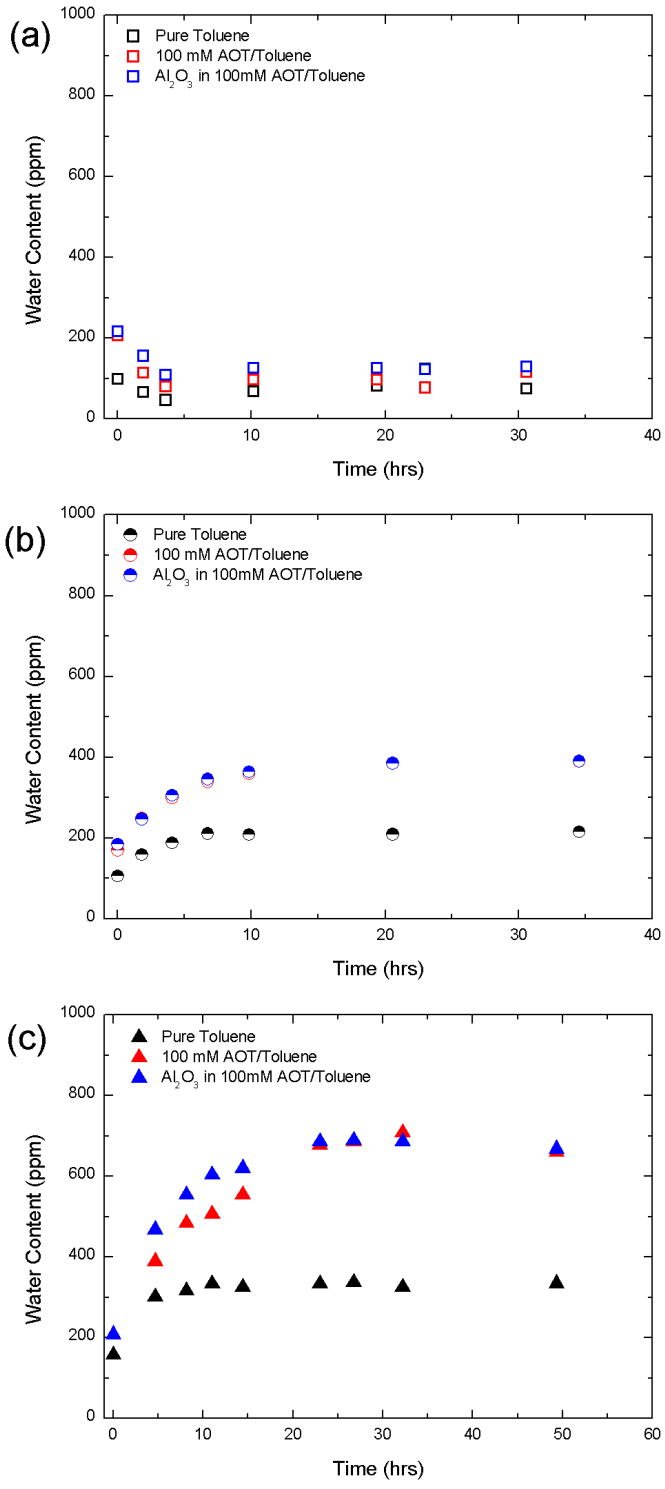

Figure 5.4. Temporal change in water content for pure toluene (black symbols), 100 mM AOT/toluene (red symbols) and Al_2O_3 dispersed in 100 mM AOT/toluene (blue symbols) for (a) low, (b) medium and (c) high relative humidity.

Layer–by–layer (LbL) assembly in this study is started after keeping dispersions at a fixed RH for ~ 24 hours. After this time, the dispersion water content does not change appreciably. Particle dispersions are sonicated for 20 minutes to get homogeneous dispersions prior to starting the LbL run. This sonication step breaks up any particle aggregates that may have formed and has little effect on the water content of the dispersions as shown Figure 5.5 below.

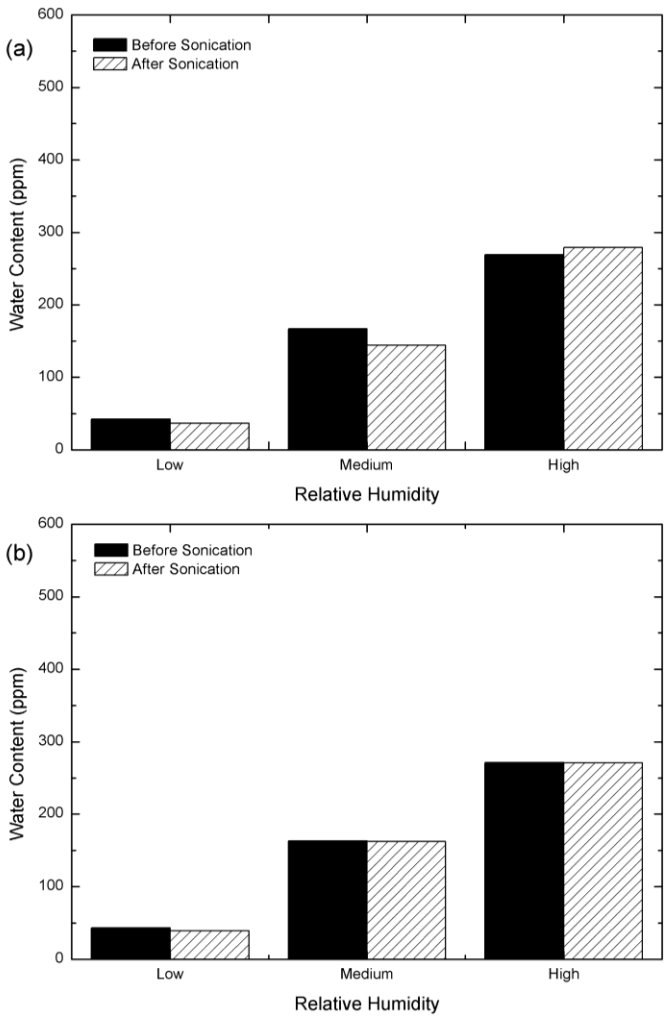

Figure 5.5. Water content of (a) Carbon black and (b) Al_2O_3 dispersed in 1 mM AOT/toluene before (left – solid color) and after (right – patterned) 20 mins of sonication. Dispersions are kept at low, medium and high relative humidity.

The 15 bilayer LbL runs used in this study take ~ 10 hours (time range ~ 24 – 34 hours in Figure 5.2 and Figure 5.4), during which the dispersion water content does not change appreciably. Meanwhile ambient lab RH fluctuates considerably with time (Figure 5.3), thus, emphasizing the importance of using a fixed RH to ensure that the water content of non–polar LbL solutions and particle dispersions does not change with time.

5.3.2 Effect of Relative Humidity on Particle Electrophoretic Mobility and Size

Al_2O_3 and carbon black (CB) dispersions with varying [AOT] are prepared and kept at low, medium and high RH to fix the water contents within the dispersions. Following this, the electrophoretic mobility (a measure of particle charge) of both particles is measured for increasing [AOT]. Both the electrophoretic mobility of Al_2O_3 and CB are found to change with [AOT] as shown in Figure 5.6a,b. In general, the magnitude of the electrophoretic mobility is characterized by an increase to a maximum value followed by a gradual decrease as [AOT] increases. Similar trends have previously been observed in studies involving charging of metal oxides and CB in non–polar media.[70, 77, 113, 123, 124] The initial rise in electrophoretic mobility is believed to be a result of increasing acid–base interactions, whereas the gradual decrease is thought to be a result of screening by charged micelles.[69, 75]

For the AOT concentrations used for LbL in this study, 1, 10, and 100 mM, the measured electrophoretic mobility reveals that RH has a significant effect on the charge of both Al_2O_3 and CB particles. In general, Figure 5.6a shows that the electrophoretic mobility of Al_2O_3 dispersed in 1 and 10 mM AOT/toluene decreases with increasing RH,

however, the electrophoretic mobility of Al_2O_3 dispersed in 100 mM AOT/toluene increases with RH. Likewise, Figure 5.6b shows that increasing RH slightly increases the electrophoretic mobility of CB dispersed in 1 mM AOT/toluene but decreases the electrophoretic mobility in 10 and 100 mM AOT/toluene. The size of Al_2O_3 particles changes slightly with water content while that of CB increases (Figure 5.6c,d).

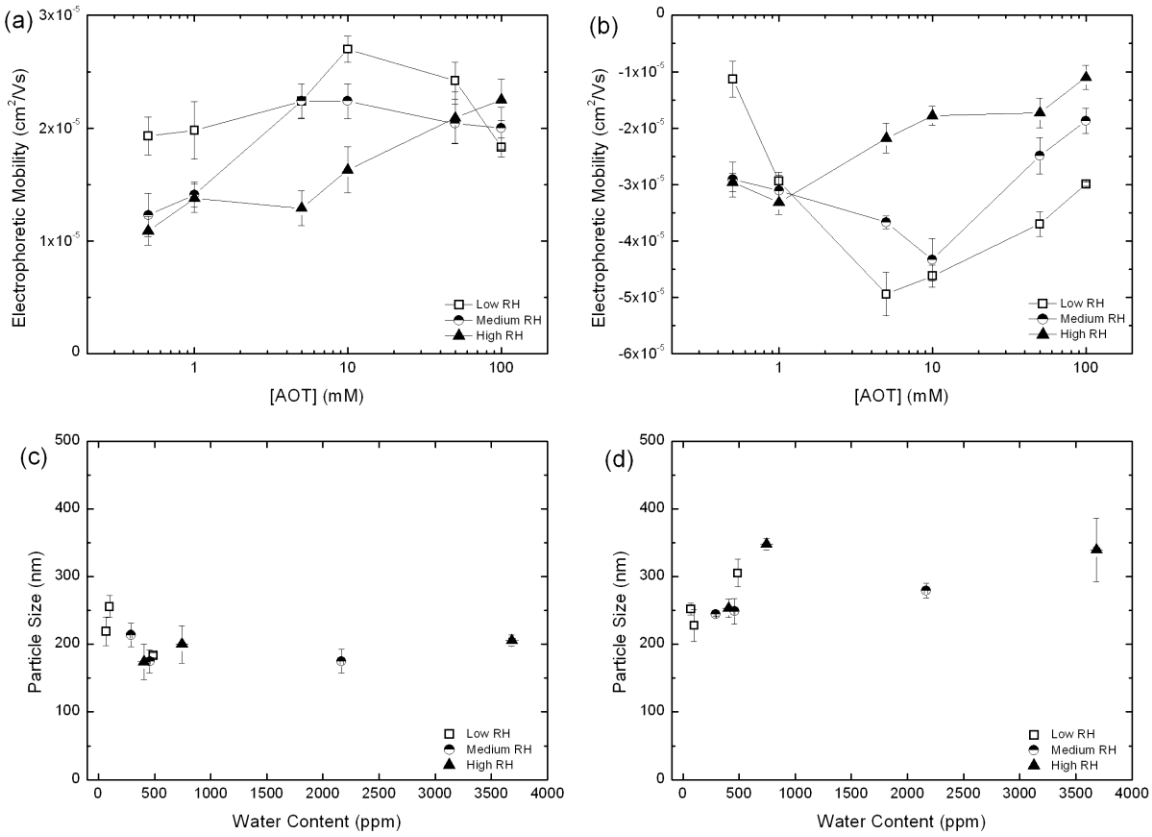

Figure 5.6. Change in electrophoretic mobility of dispersed (a) Al_2O_3, and (b) carbon black as a function of [AOT]. Change in size of (c) Al_2O_3, and (b) carbon black particles with water content in AOT/toluene. Dispersions are kept at low, medium and high relative humidity.

5.3.3 Effect of Relative Humidity on the Growth of LbL Films

The study of LbL assembly of charged Al_2O_3 and CB in AOT/toluene in *Chapter 3* revealed that the concentration of AOT ([AOT]) can be used to tune the growth behavior of LbL films. In this present study, it is possible that for a fixed [AOT], the growth of LbL films will change with RH, since increasing RH is found to have a significant effect on the electrophoretic mobility of dispersed Al_2O_3 and CB particles (Figure 5.6a,b). This hypothesis is probed by varying the LbL chamber RH for 1, 10 and 100 mM AOT assembly conditions. Figure 5.7 reveals that RH indeed has a significant effect on the growth of LbL films on bare glass slides, as films with varying darkness and uniformity are obtained depending on the [AOT] and RH combination used.

Scanning electron microscopy (SEM) images reveal that films assembled at 1 and 10 mM AOT/toluene and low RH are dense and have complete surface coverage (Figure 5.8e,f). Although the 10 mM–high RH film appears fairly uniform, SEM images (Figure 5.8c,d) show that the surface coverage is incomplete even after 15 bilayers. Visual inspection shows that the remaining assembly conditions produce films of poor quality characterized by non–uniform surface coverage even after 15 bilayers. From the SEM images of these samples (Figure 5.8a,b), it is evident that the surface coverage of Al_2O_3 and CB particles is very low.

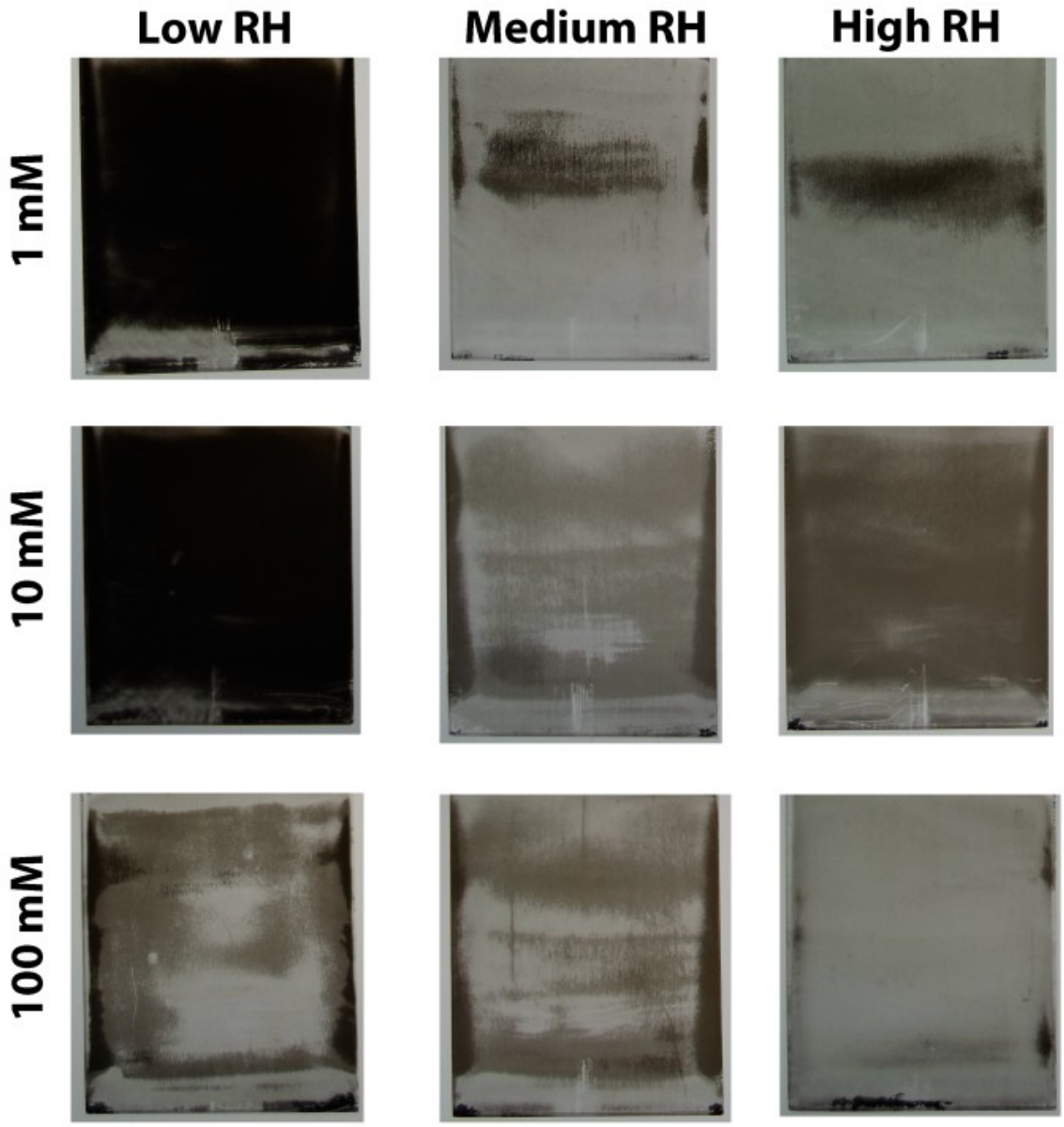

Figure 5.7. Photographs of 15 bilayer CB/Al_2O_3 LbL films formed on bare glass slide using 1, 10, and 100 mM assembly conditions. Dispersions used for LbL are kept at low, medium, and high relative humidities.

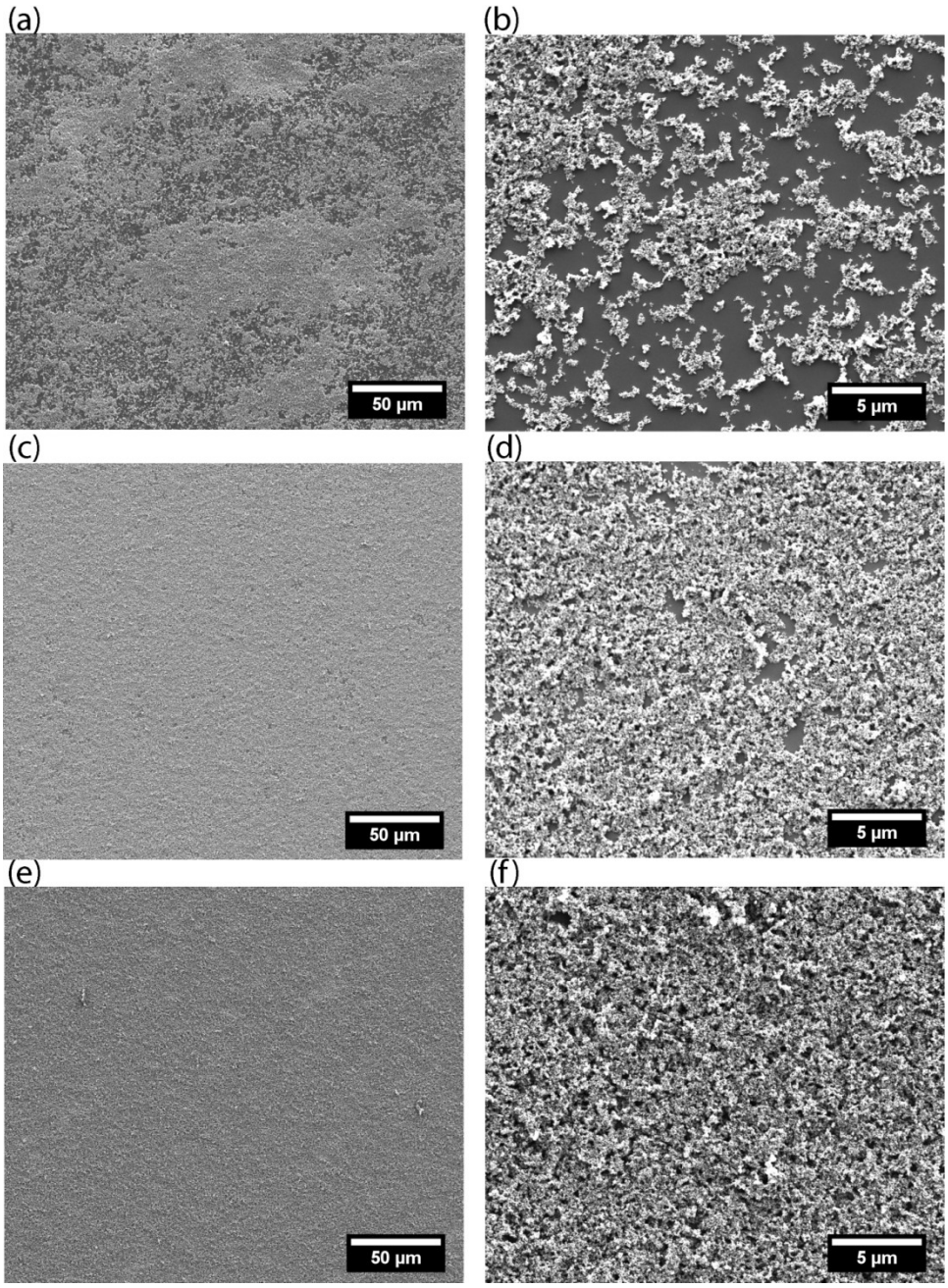

Figure 5.8. Scanning electron micrographs of CB/Al_2O_3 films assembled at (a, b) 1 mM, (c, d) 10 mM AOT/toluene and high relative humidity, (e, f) 1 mM AOT and low relative humidity (primer layer).

UV–Vis spectroscopy and film thickness measurements are used to quantify the effect of RH on the growth of LbL films. Figure 5.9 shows that the UV–Vis absorbance at 500 nm for CB/Al_2O_3 films changes with both [AOT] and RH. These changes are indicative of the amount of deposited materials on the bare glass slide as shown in Figure 5.7. It is plausible that the poor film quality for some [AOT] and RH combinations is a result of poor adhesion between particles and the substrate during LbL assembly. To address poor material adhesion in aqueous LbL assembly, primer layers are often used since they facilitate the adsorption of polymers and nanoparticles on a substrate by reducing the influence of the substrate.[11, 26, 125] For this study, a 15 bilayer CB/Al_2O_3 LbL film assembled at 1 mM–low RH is used as the primer layer since this condition gives uniform films with complete surface coverage as shown in Figure 5.7 and Figure 5.8e,f.

Figure 5.9a and Figure 5.10a respectively show the absorbance and thickness of LbL films atop primer layers. To better quantify only the LbL films deposited on the primer layer, increases in absorbance ($A_{p+f} - A_p$) and thickness ($T_{p+f} - T_p$) are calculated as shown in Figure 5.9b and Figure 5.10b respectively. Here, '*A'* represents the absorbance at 500 nm and '*T'* the thickness while subscripts '*p'* represents the primer layer and '*f*' the LbL film deposited on top of the primer layer. The increase in film thickness ($T_{p+f} - T_p$) is found to scale linearly with the increase in absorbance ($A_{p+f} - A_p$) as shown in Figure 5.10c. From these numerical results, it is evident that different growth behaviors can also be achieved on the primer layer, by changing [AOT] and RH of the LbL run. For example, both UV–Vis and thickness measurements show that high RH consistently results in the thinnest films on the primer layer for all [AOT]. Conversely,

the thickest films atop the primer layers are obtained at 1 mM–low RH and 10 mM–high RH, the latter condition being thicker than the former. Meanwhile, medium RH conditions result in films with intermediate thicknesses. Interestingly, the LbL film growth with 100 mM AOT is comparable for all RHs.

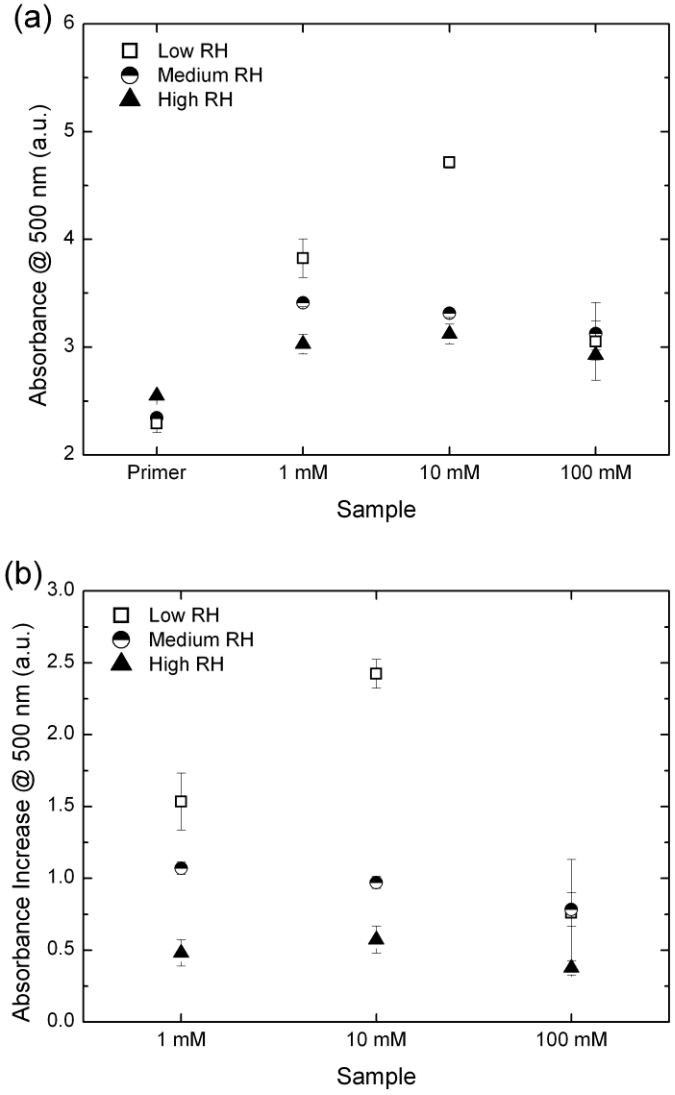

Figure 5.9. (a) UV–Vis absorbance at 500 nm for assembled CB/Al_2O_3 + primer layer films, and (b) increase in absorbance, resulting from only 15 bilayers of CB/Al_2O_3 deposited on primer layer. Films are assembled at different conditions.

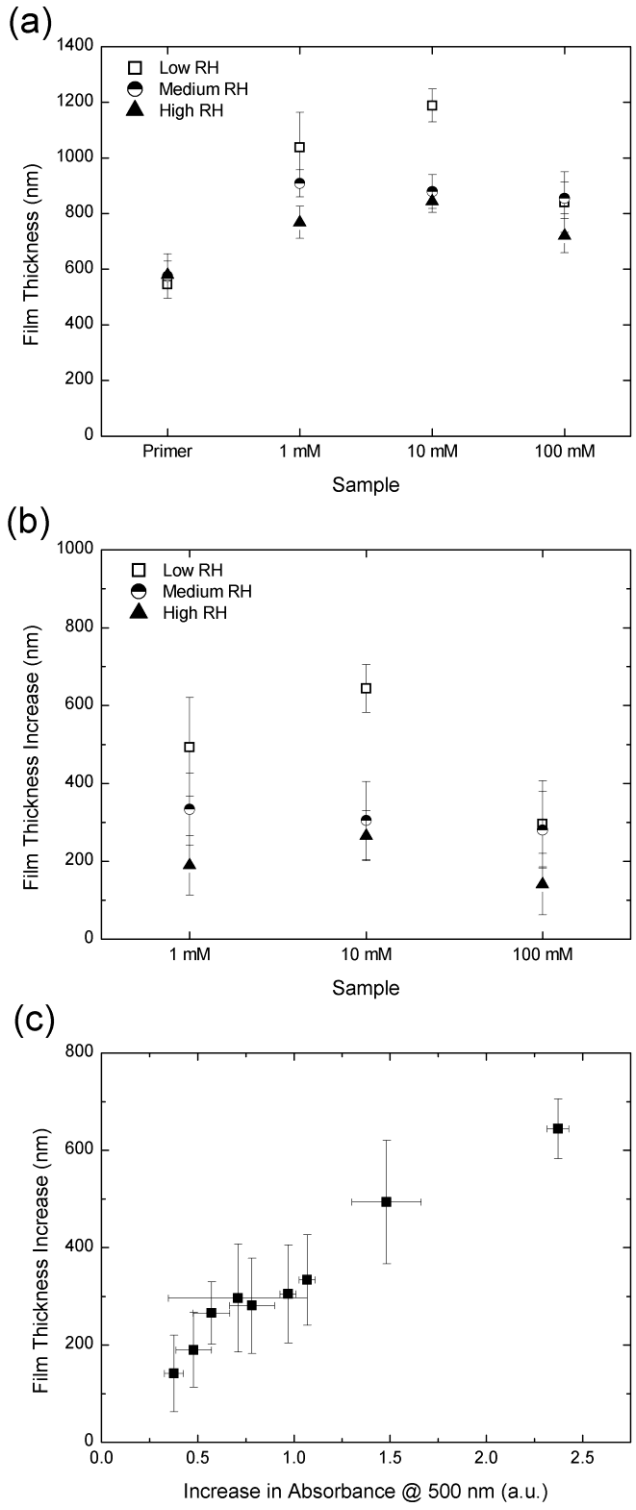

Figure 5.10. (a) Thickness measurements for CB/Al_2O_3 + primer layer films, (b) increase in film thickness compared to primer layer, and (c) increase in film thickness versus increase in absorbance. Films are assembled at different conditions.

A comparison of the UV–Vis absorbance between films deposited on bare glass slide to those atop primer layer shows that the effect of the primer layer on LbL film growth is not consistent. Figure 5.11 reveals that for some assembly conditions, specifically 10 mM–low RH, 1 mM–medium RH, and 10 mM–medium RH, the primer layer increases the deposition of material. However, for other assembly conditions such as 1 mM–low RH and 10 mM–high RH, the primer layer decreases deposition. Furthermore, the primer layer can result in negligible change in the deposition of material as seen for 1 mM–high RH, 100 mM–medium, and 100 mM–high RH.

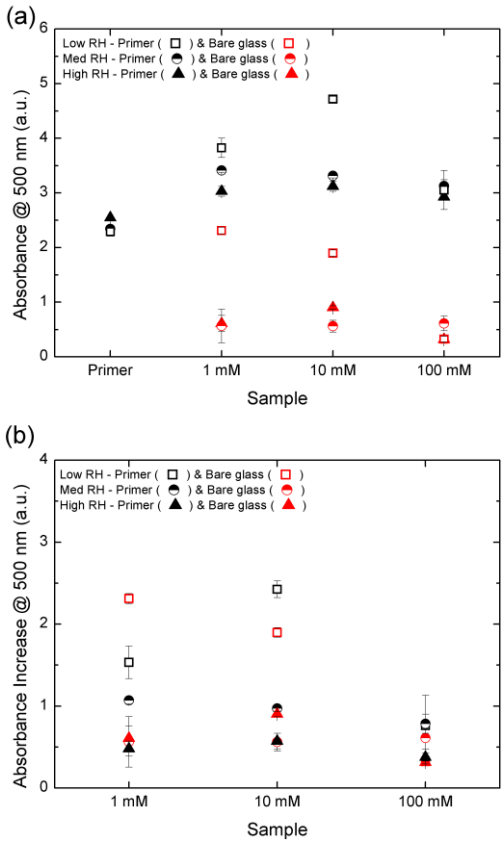

Figure 5.11. (a) UV–Vis absorbance at 500 nm for assembled CB/Al_2O_3 + primer layer films and (b) increase in absorbance compared to primer layer using dispersions kept at different relative humidities and with varying [AOT]. Black symbols represent films formed on primer layer and red symbols for films assembled on bare glass.

It is quite plausible that the absence of AOT in the pure toluene rinse baths would result in the removal of particles from the LbL films during the pure toluene rinse steps since particles have no charge in the absence of AOT; thus, the pure toluene rinse baths are replaced with AOT/toluene. This effort, however, yields no improvement in film quality or growth as exemplified by two assembly conditions: 100 mM–high RH and 10 mM–medium RH (Figure 5.12). The possiblity of any effects from the rinse procedures is therefore ruled out.

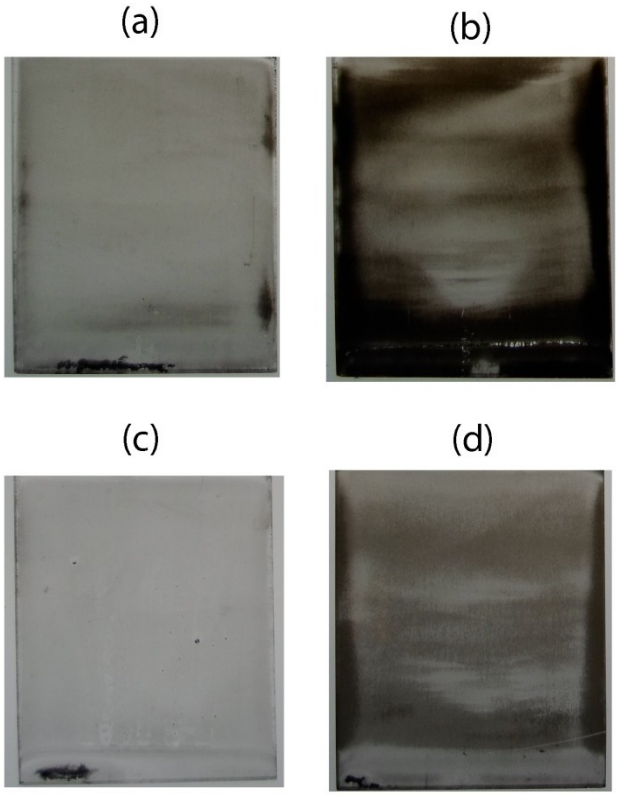

Figure 5.12. Photographs of 15 bilayer CB/Al_2O_3 LbL films assembled on bare glass slides using 100 mM assembly conditions and high relative humidity with standard rinse baths. The deposition times in particle suspensions are (a) 10 min and (b) 30 min. In (c), all rinse baths are 100 mM AOT/toluene at high relative humidity while in (d), all rinse baths are 10 mM AOT/toluene at medium relative humidity.

A prior study by Lee *et. al.* on all–nanoparticle LbL in water showed that the zeta potential ratio of oppositely charged nanoparticles in suspension can be used to control the growth of LbL films.[40] Based on this report, the changes in the electrophoretic mobility of Al_2O_3 and CB particles with RH (Figure 5.6) on the growth behavior of the LbL films is probed. The attempt to establish a relationship between the electrophoretic mobility (*EM*) ratio of CB and Al_2O_3 a (i.e. EM_{CB} / EM_{Al2O3}) as shown below in Figure 5.13, reveals no strong correlation. However, in general, the film thickness tends to decrease with RH as previously described and as shown in Figure 5.14a. This observation suggests that water content rather has an effect on the growth rate of films. Figure 5.14b shows that in fact, there is some relationship between the film thickness and the water content of the dispersions such that the thickness decreases with increasing water content.

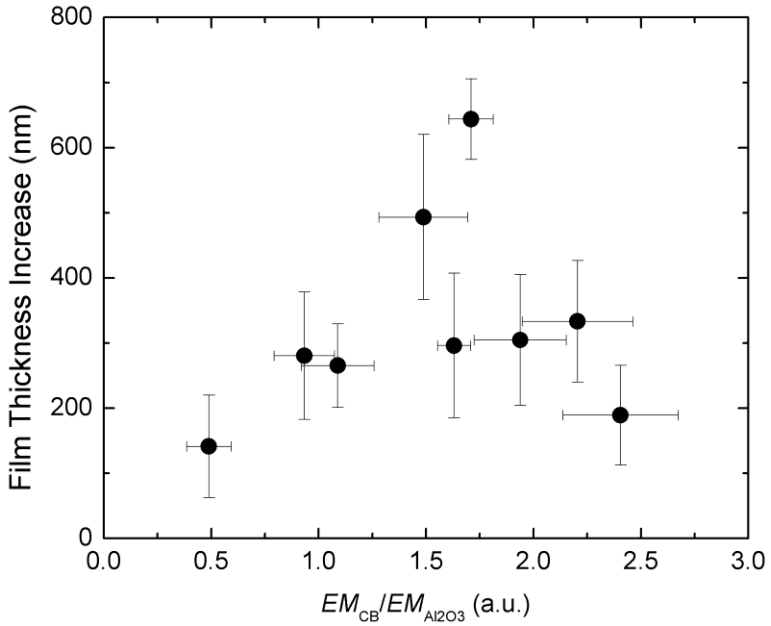

Figure 5.13. Increase in film thickness versus electrophoretic mobility (EM) ratio of CB and Al_2O_3 resulting from deposition of 15 bilayer CB/Al_2O_3 films for all assembly conditions and relative humidities.

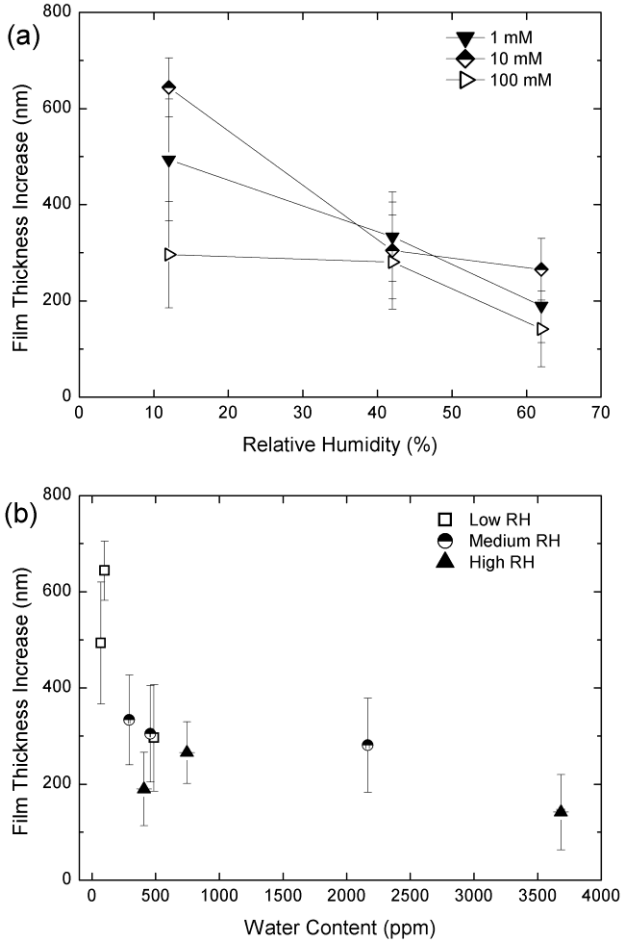

Figure 5.14. Film thickness versus (a) relative humidity, and (b) water content, for 15 bilayer CB/Al_2O_3 films assembled on top of primer layer.

Quartz crystal microbalance with dissipation (QCM–D) is employed to study the effect of water on the adsorption of CB and Al_2O_3. In QCM measurements, frequency shifts (Δf) are proportional to the change in mass of material on the QCM crystal, specifically, the adsorption of material results in more negative frequency shifts while desorption results in more positive frequency shifts. Two assembly conditions, which have contrasting growth behaviors (1 mM–low RH and 1 mM–high RH) are used. Furthermore, the LbL protocol used to assemble CB/Al_2O_3 films on bare glass slides is replicated. In this

protocol, CB is first deposited on glass slides, therefore, the QCM study begins by monitoring the adsorption of CB on a silica–coated QCM crystal. The adsorption of CB on the QCM crystal is found to be comparable for two different RHs (i.e. water contents) and [AOT] as shown in Figure 5.15a. Furthermore, the change in frequency shift with time shows that CB continues to adsorb on the surface of the QCM crystal even after the 10–minute interval used for LbL. However, CB/Al_2O_3 films formed on bare glass slides with longer deposition times of 30–minutes at high RH are nevertheless non–uniform although they appear slightly darker (Figure 5.12a,b). In the second step of the LbL protocol used, Al_2O_3 is deposited on top of the previous CB layer; therefore, the QCM study continues by monitoring the adsorption of Al_2O_3 on top of the CB–coated QCM crystal. The negative frequency shift for Al_2O_3 at low RH in Figure 5.15b reveals that Al_2O_3 adsorbs on top of the CB–coated QCM crystal, however, the adsorption of Al_2O_3 at high RH is found to differ significantly. For this high RH condition, the initial frequency shift during exposure of CB–coated QCM crystal to Al_2O_3 is slightly positive, implying that a small amount of the preexisting CB layer desorbs from the surface. However, after ~20 minutes, the frequency shift becomes slightly negative due to the adsorption of a small amount of Al_2O_3. This result, along with similar adsorption behavior observed for 100 mM–high RH sample (Figure 5.16) suggests that the relatively low adsorption of Al_2O_3 at high RH compared to the adsorption of Al_2O_3 at low RH results in poor film growth. In fact, there is some agreement with the earlier study on CB/Al_2O_3 LbL films (*Chapter 3*) in which repeated deposition of glass slides in only CB dispersions gave films (Figure 3.7b) comparable to the non–uniform films shown in Figure 5.7.[123]

Furthermore, the slight desorption of preexisting CB layers during exposure to Al_2O_3 accounts for the decrease in the thickness of CB/Al_2O_3 LbL films assembled on top of a primer layer for some assembly conditions. Although the exact reason for the negligible adsorption of Al_2O_3 at high RH remains unclear, it is quite possible that a combination of water content, particle charge and adsorbed AOT play a critical role in the adsorption of particles. The relative contribution of each parameter warrants further investigation on the adsorption of particles will warrant further study.

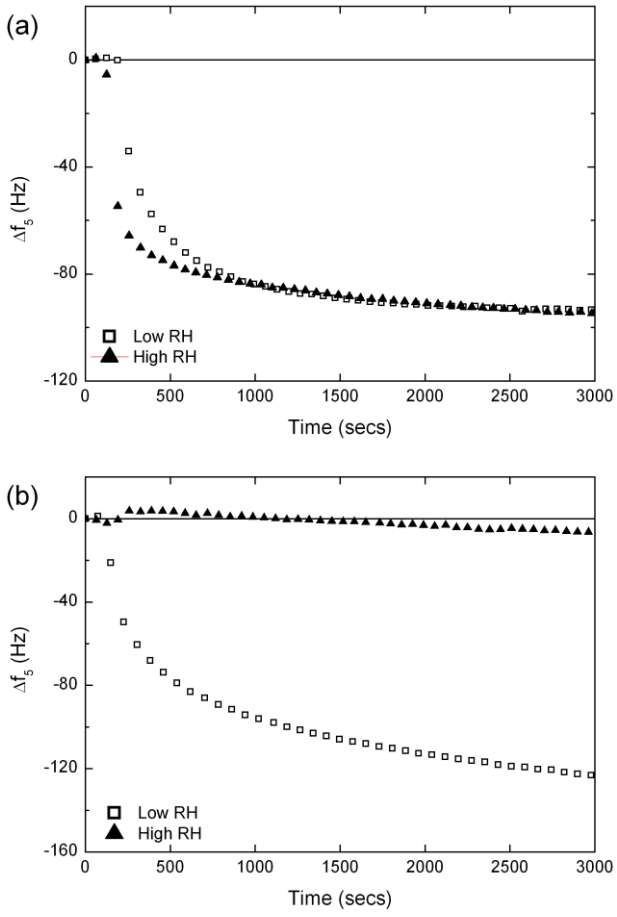

Figure 5.15. QCM frequency shifts (fifth overtone – Δf_5) for (a) carbon black depositing on bare Si QCM crystal and (b) Al_2O_3 depositing on carbon black coated QCM crystal. Both particles are dispersed in 1 mM AOT/toluene at low and high RH.

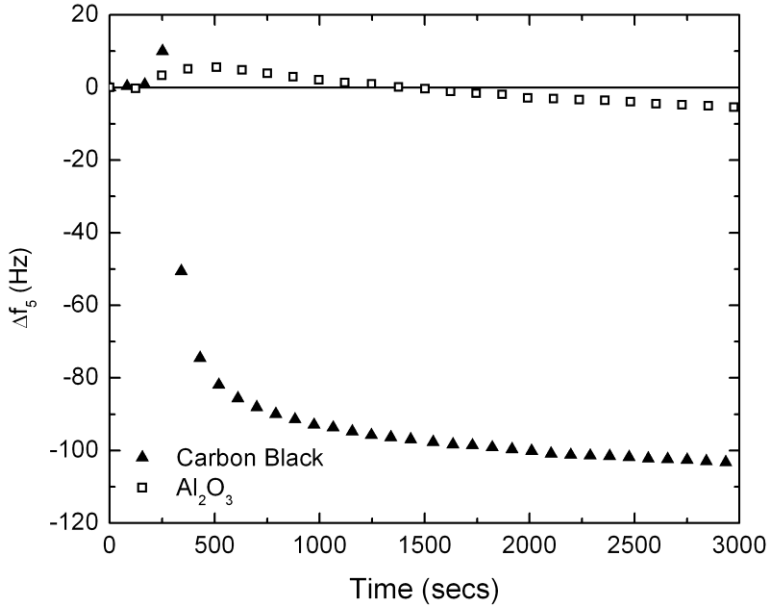

Figure 5.16. QCM frequency shifts (fifth overtone – Δf_5) for carbon black and Al_2O_3 dispersed in 100 mM AOT/toluene at high RH. Carbon black adsorbs on a bare Si QCM crystal while Al_2O_3 adsorbs on a carbon black coated QCM crystal.

5.4 Conclusions

In conclusion, the study presented in this chapter showed that relative humidity has a significant effect on the water content of AOT/toluene solutions and particle dispersions used for LbL assembly in a non–polar solvent, toluene. These changes, in turn, affect the electrophoretic mobility of Al_2O_3 and CB particles in AOT/toluene. Furthermore, RH affects the growth and quality of LbL assembled CB/Al_2O_3 films. In general, for a fixed [AOT], the thickness of CB/Al_2O_3 films formed tends to decrease as RH increases, thus emphasizing the importance of controlling the water content in particle dispersions used during LbL assembly in non–polar solvents. Increasing water content was found to diminish the adsorption of Al_2O_3, which in turn hampers the growth of films. The origin

of this behavior remains unclear; however, it is possible that the particle charge, the amount of water present in dispersions, and even adsorbed AOT could all play a role in the adsorption of particles and growth of LbL assembled films in non–polar media. Future work will involve elucidating the role of each of these parameters on LbL assembly film growth in non–polar solvents.

Chapter 6. Photocatalytic and Conductive MWCNT/TiO_2 Nanocomposite Thin Films Generated via Layer–by–Layer Assembly in Non–Polar Media

Reprinted (adapted) with permission from Tettey, K. E.; Yee, M. Q.; Lee, D. Photocatalytic and Conductive MWCNT/TiO_2 Nanocomposite Thin Films. ACS Appl. Mater. Interfaces, 2010, 2, 2646–2652. Copyright (2010) American Chemical Society.

6.1 Introduction

Photocatalytic materials convert solar energy to chemical energy, making them useful for the decontamination of organics[126, 127] and biological pathogens.[128, 129] Titanium dioxide (TiO_2) is one of several semiconductors with desirable photocatalytic properties which generates electron–hole pairs upon activation by ultraviolet (UV) light. These electron–hole pairs, in turn, create active species such as surface associated OH radicals, photogenerated OH radicals and superoxides ($O_2\cdot$), which participate in subsequent chemical reactions leading to the degradation of organic contaminants.[130]

The utility of TiO_2 as a photocatalyst, however, is often limited by the recombination of photogenerated electron–hole pairs.[130] Suppression of electron–hole recombination is thought to be imperative for improving the photocatalytic activity of TiO_2.[130] One proposed method of achieving this task is by creating nanocomposites of TiO_2 and carbon nanotubes (CNTs). The unique characteristics of CNTs, such as their electron–accepting capability and conductivity, make them ideal for sequestering photogenerated electrons.[131] These properties of CNTs could hinder electron–hole

recombination, thus leading to the enhancement of TiO_2 photocatalytic activity. In addition, the suppression of electron–hole recombination in TiO_2 has been utilized to improve the efficiency of dye–sensitized solar cells[132] and photoelectrochemical solar cells.[133]

CNT–TiO_2 nanocomposites have been prepared through a number of different techniques. These include hydrothermal treatment,[132,134] sol–gel coating of CNTs,[135, 136] hydrolysis,[137] electrodeposition[138] and electrospinning.[139] A major drawback to many of these methods is that they typically depend on the oxidation of CNTs to prepare CNT/TiO_2 nanocomposites. Although the fabrication process can be readily facilitated by using oxidation, such treatment typically involves the use of highly corrosive chemicals and drastically changes the electronic properties of CNTs by disrupting their conjugated structure. Such changes, in turn, degrade the efficacy of CNTs as electron acceptors and carriers.[39, 140] In addition, the aforementioned methods of fabricating CNT/TiO_2 nanocomposites have been mostly used for the generation of bulk nanocomposites and do not provide a straightforward method for creating conformal thin films and coatings with precisely controlled composition and properties. The generation of CNT/TiO_2 thin films would enhance the utility of these nanocomposites in various applications.

One versatile method of fabricating nanocomposite thin films is layer–by–layer (LbL) assembly. Previous reports have demonstrated that photocatalytic thin films composed of TiO_2 nanoparticles and charged polymers can be generated by LbL assembly.[141-145] Incorporation of CNTs into TiO_2 thin films using LbL assembly could further enhance their photocatalytic activity. However, LbL assembled nanocomposite

thin films composed of CNTs have been generally prepared using oxidized CNTs paired with an oppositely charged polymer in aqueous solutions.[146-148] Although high temperature hydrogen treatment can be used to reduce the oxidized bonds in CNTs, the complete recovery of the pristine properties of CNTs is difficult.[149] While un–oxidized CNTs have been incorporated into LbL assembly films from aqueous solutions using anionic surfactants,[150] aromatic surfactants[151, 152] and copolymers,[153] such approaches typically require the utilization of newly synthesized molecules for the stabilization of CNTs.

The study reported in this chapter utilizes the LbL assembly technique developed in *Chapter 3* to demonstrate that conductive and photocatalytic MWCNT/TiO_2 nanocomposite thin films can be generated based on LbL assembly in non–polar solvents. This LbL assembly approach enables the incorporation of pristine MWCNTs into thin films without the need for their oxidation through harsh chemical treatments. In addition, it will be shown that the growth behavior and electrical properties of MWCNT/TiO_2 thin films can be controlled by varying the assembly parameters, and that the presence of MWCNTs enhances the photocatalytic activity of TiO_2 nanoparticles.

6.2 Experimental Section

6.2.1 Electrophoretic Mobility Measurements

MWCNT and TiO_2 particle suspensions in toluene containing AOT (AOT/toluene) are made by firstly preparing 0.1 wt. % of particles in pure toluene (Fisher). 200, 100, 20, 10,

2 and 1 mM AOT (Sigma–Aldrich) in toluene are also prepared in separate vials. The 0.1 wt % TiO_2 powder (Degussa P25) and MWCNTs (Cheap Tubes Inc.) in pure toluene is sonicated for 1 hour then mixed with an equal volume (3 mL) of AOT/toluene solutions to obtain 0.05 wt. % particles in 100, 50, 10, 5, 1 and 0.5 mM AOT/toluene. Particle suspensions in AOT/toluene are sonicated for an additional hour. TiO_2 suspensions are allowed to sediment overnight and MWCNTs are filtered through a 5 μm PTFE filter before being used for electrophoretic mobility measurements. Electrophoretic mobility measurements are made with a Beckman Coulter Delsa Nano–C at a field voltage of 85.2V/cm.

6.2.2 Layer–by–Layer Assembly of MWCNTs and TiO_2

AOT/toluene solutions (60 mL) are prepared by making a 400 mM AOT stock solution followed by dilution to 200, 100, 20 and 10 mM solutions. 0.1 wt. % of TiO_2 and MWCNTs (60 mL) are prepared in pure toluene and sonicated for 1 hour. An equal volume (30 mL) of AOT/toluene solutions and 0.1 wt. % particle suspension in pure toluene are mixed together and sonicated for 1 hour to yield 0.05 wt. % TiO_2 and MWCNTs in 200, 100, 50, 10 and 5 mM AOT/toluene. LbL assembly of MWCNTs and TiO_2 is performed on glass slides (Fisherbrand) cleaned by sonication in NaOH (1 M) for 20 min followed by rinsing in de–ionized (D.I.) water (18.2 MΩ–cm) and drying with compressed air. The cleaned glass slides are exposed to the prepared solutions in the following order: 0.05 wt. % MWCNTs in AOT/toluene, AOT/toluene rinse, toluene and toluene followed by 0.05 wt. % TiO_2 in AOT/toluene, AOT/toluene rinse, toluene and

toluene. The concentration of AOT in the AOT/toluene rinse baths is kept at the same concentration as in particle suspensions. A StratoSequencer VI (NanoStrata Inc.) is programmed to expose slides in particle suspensions for 10 min, followed by 2, 1 and 1 min in rinse baths.

6.2.3 MWCNT/TiO_2 Film Characterization

Absorbance measurements on films are made using a Cary 5000 (Varian Inc.) UV–Vis–NIR spectrophotometer. The absorbance at 500 nm is used for all data analysis. SEM images are taken with an FEI 600 Quanta FEG ESEM at 5 kV. Sheet resistance measurements are taken with a four–point probe station comprised of a Cascade Microtech C4S 4–Point probe head, HP power supply unit and Keithley 2000 multimeters. Voltage and current measurements are taken at 10 random locations on each MWCNT/TiO_2 film. These values are subsequently used to calculate the sheet resistance. Thickness measurements are made with a Zygo NewView 6K series optical profilometer. To get an averaged film thickness, height profiles along a line segment are integrated and normalized with the length of the profile. Film thickness and sheet resistance measurements are used to calculate film conductivities. TGA measurements are taken with a TA Instruments SDT Q600. Samples for TGA are prepared by scraping off 60–bilayer films into a platinum TGA pan. The temperature is ramped from room temperature to 110 ^{o}C at 10 ^{o}C/min then held for 20 minutes to remove residual moisture. Following this, the temperature is increased to 1000 ^{o}C at a ramp rate of 10 ^{o}C/min and in air. Surface coverage is determined by analyzing SEM images using image analysis

software ImageJ. The image threshold is adjusted until all MWCNT/TiO_2 domains are covered. From this, the surface coverage is calculated as the ratio between the area of MWCNT/TiO_2 domains and the total image area.

6.2.4 Photocatalytic Activity of MWCNT/TiO_2 Films

Photocatalysis experiments are performed by preparing 5 mg/L Procion Red MX–50 dye (Sigma–Aldrich) in D.I. water as the model organic contaminant. The glass slides on which MWCNT/TiO_2 films are prepared are cut to make use of only the regions with assembled films. For consistency, the same film areas are used for each set of experiments. The slides are placed in a plastic petri dish containing dye solution (7 mL). The petri dish is covered with a quartz slide to minimize evaporation. A UV lamp (UVP Inc.) is placed 6.7 cm above the petri dish followed by insulation of the setup from external light. Longwave UV (365 nm, 6 W) is used for all experiments. 500 μL of dye sample is collected every 30 min for UV–Vis analysis. For this analysis, the absorbance at the peak (538 nm) is monitored to determine the concentration change of the dye solution. Single component TiO_2 films are formed by calcining MWCNT/TiO_2 films at 600^{o}C for 1 hour. The same procedure described above is used to probe the photocatalytic activity of single component TiO_2 films. X–ray diffraction (XRD) analysis is performed using a Rigaku GeigerFlex D/Max–B powder diffractometer equipped with a Cu Kα source. The fate of AOT after photocatalysis is probed by using FTIR spectroscopy. 30–bilayer MWCNT/TiO_2 films from 100 mM AOT suspensions are deposited on two CaF_2 FTIR windows (Thorlabs Inc.). Each sample is placed in a plastic

petri dish containing D.I. water. While the first film was kept in the dark for 5 hours, the second was irradiated with 365 nm UV for the same period. A Nicolet 8700 FTIR spectrometer (Thermo Scientific) is used for data acquisition.

6.3 Results and Discussion

6.3.1 Charging of MWCNT and TiO_2 in Toluene

Particles in non–polar solvents tend to be colloidally unstable when no electrostatic or steric repulsion exists between them.[154] To suspend multi–walled carbon nanotubes (MWCNTs) and TiO_2 nanoparticles by electrostatic repulsion in a low permittivity solvent, toluene ($\varepsilon = 2.3$), a charge inducing agent, Aerosol OT (AOT), is used. In non–polar solvents, it is believed that AOT molecules form reverse micelles, a small fraction of which undergo spontaneous disproportionation to from oppositely charged micelles. [44, 69] While TiO_2 and MWCNTs could not be dispersed in pure toluene, TiO_2 became well dispersed throughout our AOT concentration range (0.5 – 100 mM) and MWCNTs became well dispersed in solutions with AOT concentration of 5 mM and greater as shown below in Figure 6.1.

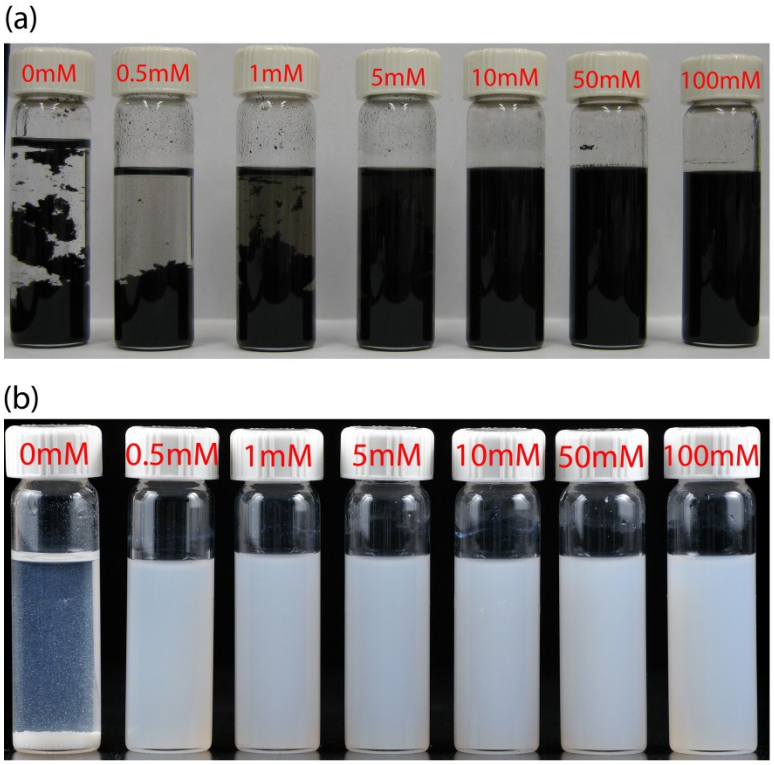

Figure 6.1. (a) MWCNTs and (b) TiO_2 dispersed in toluene containing different AOT concentrations shown in red text.

To observe the change in surface charge of TiO_2 and MWCNTs in toluene with varying concentration of AOT ([AOT]), electrophoretic mobility measurements are taken as shown in Figure 6.2. The electrophoretic mobility of both TiO_2 and MWCNTs is seen to depend on [AOT]. Interestingly, while TiO_2 particles acquired positive charge, MWCNTs became negatively charged in AOT/toluene solutions. In *Chapter 3*, carbon–based material (carbon black) was shown to become negatively charged, while oxide alumina became positively charged in AOT/toluene solutions.[123] Figure 6.2a and Figure 6.2b show that the magnitude of the electrophoretic mobility of TiO_2 and MWCNTs increases

with [AOT] and have maximum magnitude between 10 – 50 mM AOT. As the concentration of AOT increases beyond a peak value, AOT counterions overcrowd and screen the surface leading to a decrease in the surface charge.[70]

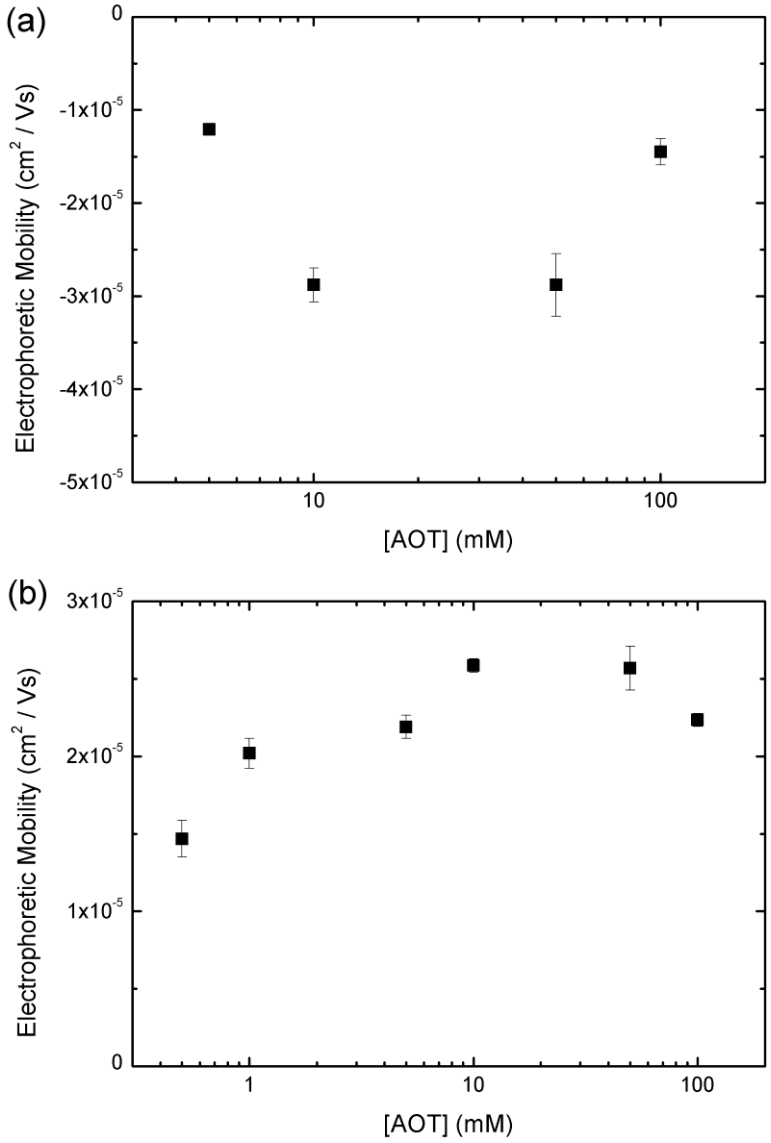

Figure 6.2. Electrophoretic mobility of dispersed (a) MWCNTs and (b) TiO_2 as a function of [AOT] present in toluene solution. Error bars represent standard deviations of three measurements. TiO_2 particles acquire a positive charge whereas MWCNTs become negatively charged in AOT/Toluene.

6.3.2 Heteroaggregation of MWCNT and TiO_2 in Toluene

To test for the existence of attractive interactions between oppositely charged particles, MWCNTs and TiO_2 in AOT/toluene solution were mixed together in a 1:1 ratio in a similar manner to the test carried out in *Chapter 3*. The mixture begins to quickly aggregate and eventually becomes clear overnight as shown below in Figure 6.3. The heteroaggregation of oppositely charged MWCNTs and TiO_2 strongly suggests the existence of attractive forces in this non–polar medium thus making this system useful for LbL.

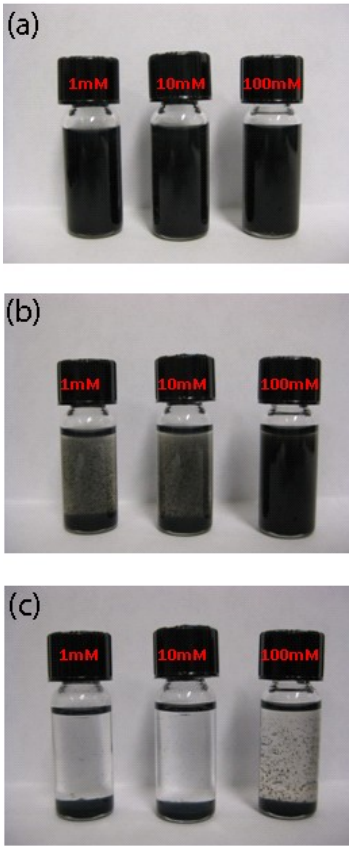

Figure 6.3. Heteroaggregation of charged MWCNTs and TiO_2 in toluene at (a) time = 0, (b) time = 5 mins and (c) time = 24 hours. The concentration of AOT in each mixture is indicated

6.3.3 Layer–by–Layer Assembly of Charged MWCNT and TiO_2 in Toluene

LbL assembly of MWCNTs and TiO_2 suspended in a wide range of AOT concentration is performed on glass slides to generate MWCNT/TiO_2 nanocomposite thin films. These nanocomposite films became darker with increasing number of deposited bilayers as shown in Figure 6.4a. UV–Vis absorbance measurements (Figure 6.4b) also show that the absorbance of the films increases with the number of bilayers. The increase in absorbance as a function of deposited bilayers is linear for each assembly condition, indicating that the incorporation of MWCNTs within the film increases linearly. Such linear growth is often observed for LbL assembly of oppositely charged materials in aqueous solutions.[155] The slope of the absorbance as a function of deposited bilayers is also seen to vary with the concentration of AOT in solution. This dependence indicates that changing the concentration of AOT is a convenient method of controlling film growth and composition during LbL assembly in non–polar media, a direct analogy to controlling the pH and/or ionic strength of aqueous solutions.[12]

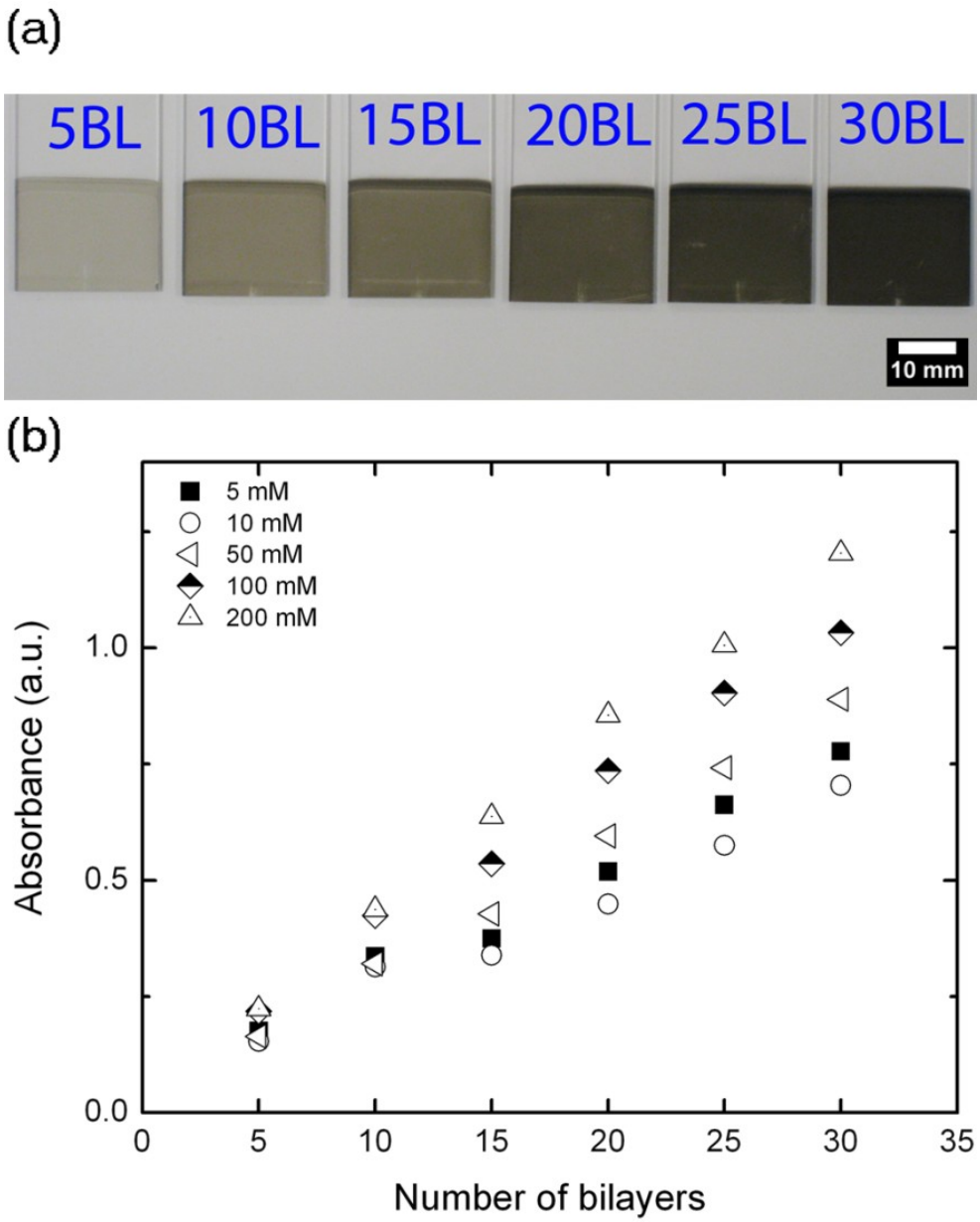

Figure 6.4. (a) Picture of MWCNT/TiO_2 films assembled on glass slides with 50 mM AOT in MWCNT and TiO_2 solutions. The blue text on glass slide represents the number of bilayers (e.g. 5BL = 5 bilayers). (b) Absorbance (measured at 500 nm) of MWCNT/TiO_2 films on glass slides as a function of the number of bilayers.

The morphology of MWCNT/TiO_2 nanocomposite films was investigated using scanning electron microscopy (Figure 6.5). These images reveal that the surface coverage of MWCNT/TiO_2 films increases with the number of deposited bilayers. For 5– and 10–bilayer films (Figure 6.5a,b), MWCNT and TiO_2 particles are seen to cluster into isolated domains on the surface. These isolated clusters of TiO_2 and MWCNTs continue to grow laterally until, a contiguous film is formed as seen in Figure 6.5c. Since the Debye length of charged species in AOT/toluene solutions is very large due to the low dielectric constant of the solution,[73] the long–ranged electrostatic repulsion between particles with the same charge likely plays a significant role in the formation of particle domains on the surface. Similar transitions in film morphology have been observed for LbL assembly of oppositely charged nanomaterials in aqueous media[12] as well as in LbL assembly of oppositely charged carbon black and alumina in toluene as discussed in *Chapter 3*.[123]

Figure 6.5c,d illustrates the porous nature of these MWCNT/TiO_2 films. High film porosities are particularly advantageous for catalysis applications. Previous studies based on the LbL assembly of oppositely charged nanoparticles have also shown that porous structures are useful for controlling the wetting and optical properties of surfaces.[22, 58] A high magnification image of a 30–bilayer film (Figure 6.5d) shows that MWCNTs are homogeneously dispersed in the film, maximizing the contact area between MWCNTs and TiO_2. Homogeneous dispersion of MWCNTs within the film is important for forming a continuous network for electron transport and for preventing the recombination of photogenerated electron–hole pairs.

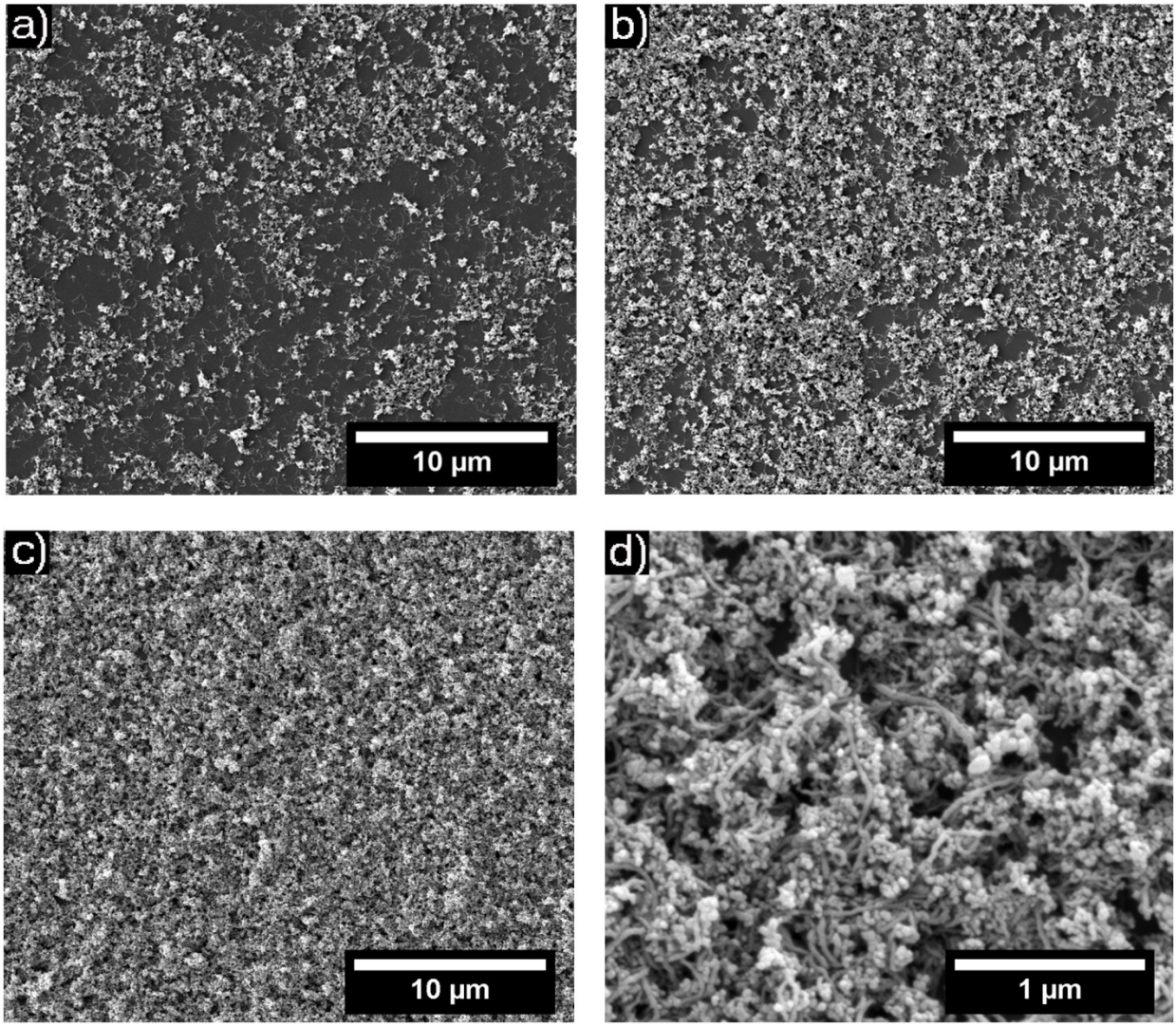

Figure 6.5. SEM images comparing the morphology of MWCNT/TiO_2 films for (a) 5 bilayers, (b) 10 bilayers, (c) and (d) 30 bilayers. MWCNT/TiO_2 films are generated using particles suspended in 50 mM AOT/toluene solutions.

6.3.4 Film Composition

UV–Vis absorbance measurements show that the absorbance of the nanocomposite films depends on [AOT], suggesting that the composition of the films is changing. To confirm this observation, the mass fractions of AOT, MWCNTs and TiO_2 in films assembled from solutions with varying [AOT] are quantified by using thermogravimetric analysis (TGA). The composition of films obtained from TGA thermograms are summarized in Table 6.1. The results show that the [AOT] affects the composition of films fabricated from different assembly conditions. The increase in mass fraction of MWCNTs due to changing assembly conditions, albeit small, suggests that the [AOT] can be used to tune film composition.

Table 6.1. Composition of MWCNT/TiO_2 films assembled with different [AOT].

[AOT] (mM)	AOT (%)	MWCNT (%)	TiO_2 (%)
50	6.0	12.1	81.9
100	7.4	13.1	79.5
200	7.5	13.8	78.7

6.3.5 Conductivity of MWCNT/TiO_2 Films

CNT/TiO_2 nanocomposites have shown great promise for their application in photocatalysis and photovoltaics. This is primarily because the conjugated structure of CNTs enables them to act as excellent carriers through which electrons can transport efficiently. This property is especially attractive for generating working electrodes for dye–sensitized solar cells (DSSCs) since the continuous pathway for electron transport

ensures an efficient collection of photogenerated electrons produced by TiO_2 nanoparticles.[132] In addition to this application, conductive films could have useful roles for applications such as capacitors and batteries.[156, 157]

The effect of MWCNTs on the conductivity of our nanocomposite films is studied by taking sheet resistance measurements as a function of the number of deposited bilayers as shown in Figure 6.6. The observed decrease in sheet resistance (Figure 6.6a) with increasing number of deposited bilayers indicates that the MWCNT/TiO_2 films become more conductive. This increase in conductivity is attributed to an increase in MWCNTs in the films and, more importantly, to the increased percolation of MWCNTs within the nanocomposite film as more bilayers are deposited. As the isolated domains of TiO_2 and MWCNTs on the substrate begin to merge, they form contiguous films as seen in morphological transitions in Figure 6.5.

The results from thermogravimetric analysis (TGA) of the MWCNT/TiO_2 composite films (Table 6.1) show that AOT is incorporated within the nanocomposite films during LbL assembly. It is likely that AOT forms thin layers on MWCNTs and TiO_2, which could influence the conductivity of the nanocomposite thin film. Although AOT is an insulator, the nanocomposite films are, nevertheless, conductive. Other studies that generate LbL composite films containing CNTs have shown that the films are conductive despite the presence of insulating organic materials.[150] It also has been reported that the conductivity in nanocomposites does not necessarily require uninterrupted electrical contact between MWCNTs, but rather needs sporadic ohmic connections between MWCNTs.[153] Electron transport from TiO_2 to MWCNTs could

occur based on a similar mechanism. Interestingly, attempts to selectively remove AOT via thermal treatment at 400 °C under inert condition led to a negligible change in the conductivity of MWCNT/TiO_2 nanocomposite thin films.

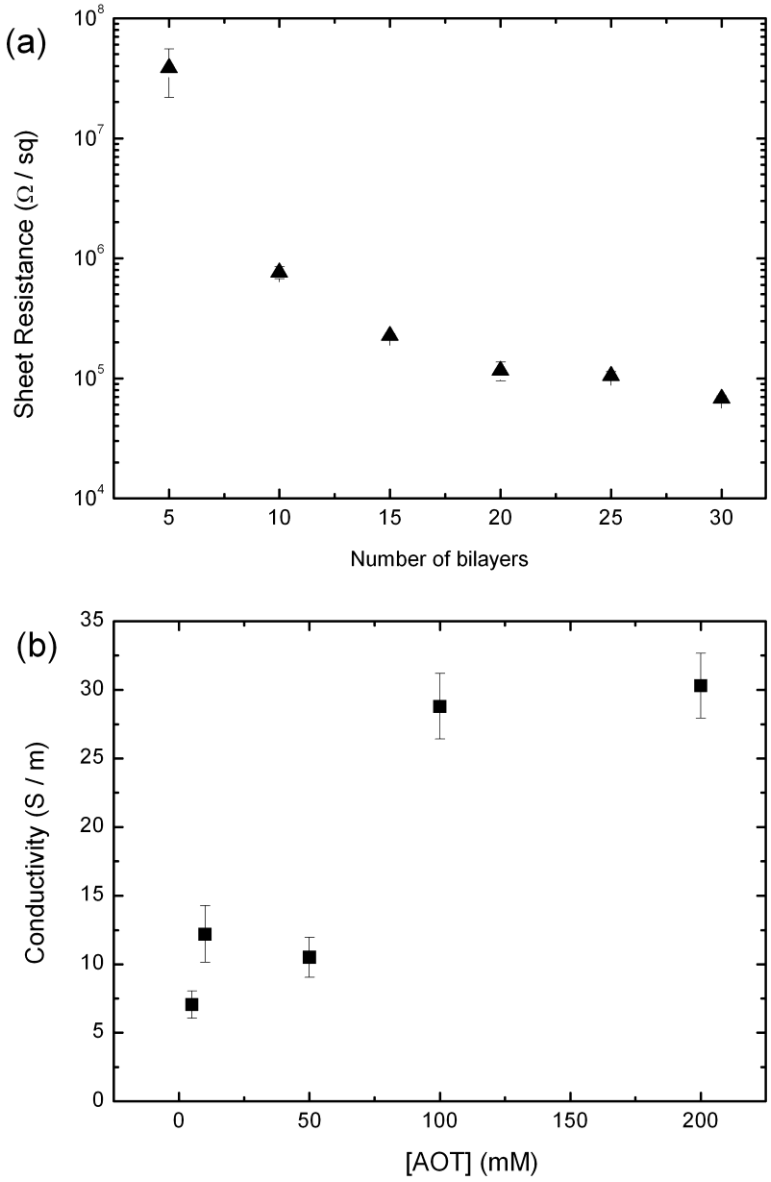

Figure 6.6. (a) Sheet resistance measurements as a function of number of desposited bilyaers for MWCNT/TiO_2 films fabricated from 200 mM AOT suspensions. (b) Conductivity of 30–bilayer MWCNT/TiO_2 films as a function of [AOT]. Error bars indicate standard deviations for 10 measurement.

The effect of assembly conditions (i.e., the concentration of AOT) on the conductivity of MWCNT/TiO_2 films is illustrated by conductivity values for 30–bilayer films as shown in Figure 6.6b. Here, the conductivity of the LbL films increases with the [AOT]. This observed trend is likely a result of an increase in MWCNT loading in the films as the [AOT] is increased. This hypothesis is supported by the fact that as the concentration of AOT is increased, UV–Vis and TGA measurements show a corresponding increase in MWCNTs within the film.

Figure 6.6b also shows that the conductivity of 30–bilayer MWCNT/TiO_2 films lies in two distinct groups. The conductivity of 5, 10 and 50 mM samples are comparable, but smaller than 100 and 200 mM samples. The higher conductivity of 100 and 200 mM films is ascribed to the dense network of MWCNTs within these films. SEM images of 20–bilayer MWCNT/TiO_2 nanocomposite films assembled at different AOT concentrations highlight the differences in film morphology for a fixed number of bilayers. While films assembled with 5, 10 and 50 mM AOT solutions are seen to have non–uniform surface coverage (Figure 6.7a–c), those generated in 100 and 200 mM AOT solutions form a homogeneous network of MWCNT/TiO_2 nanocomposite (Figure 6.7d,e).

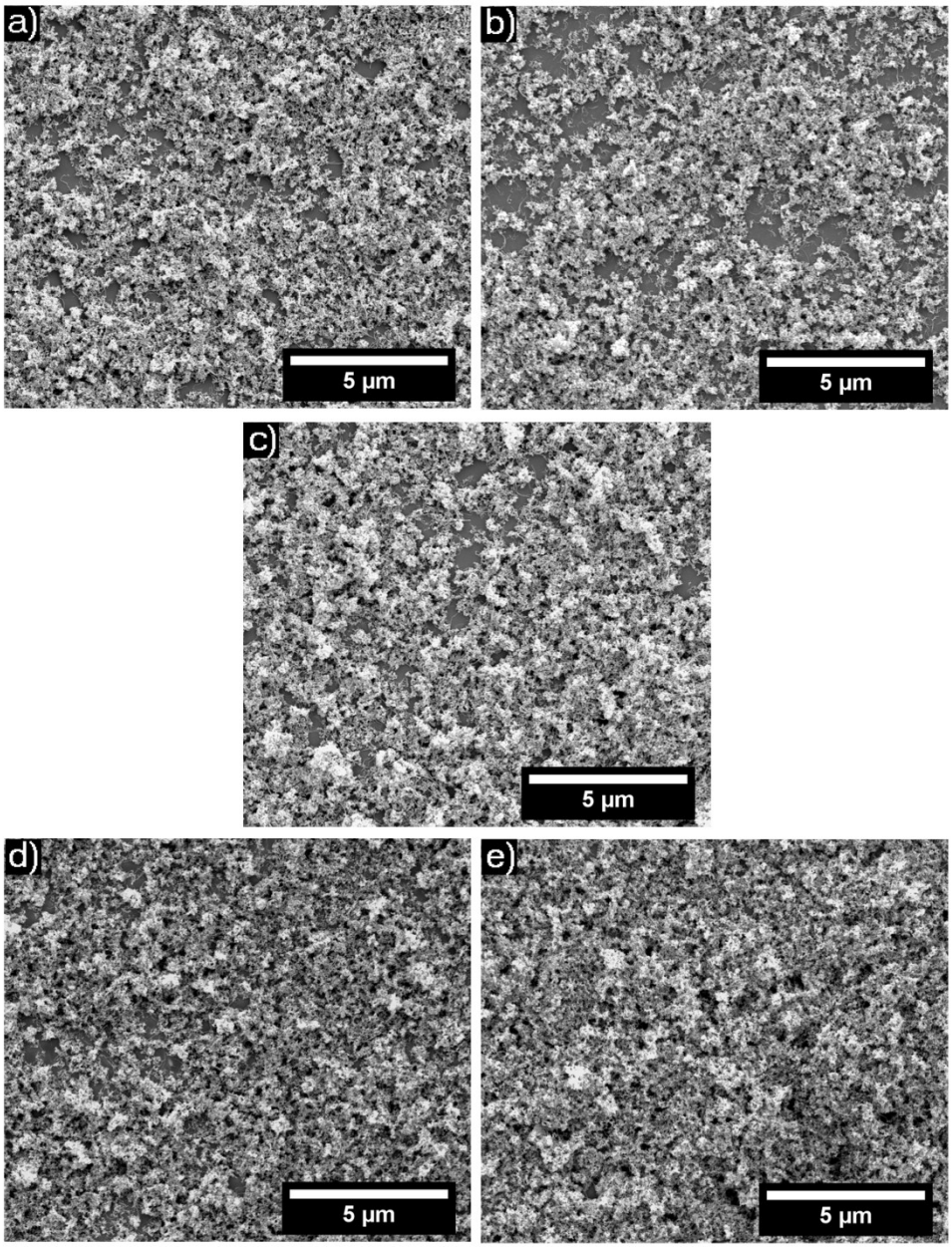

Figure 6.7. SEM images for 20–bilayer MWCNT/TiO_2 films composed with (a) 5 mM, (b) 10 mM, (c) 50 mM, (d) 100 mM and (e) 200 mM AOT.

The surface coverage of 20–bilayer films, quantified as seen in Figure 6.8, confirms that the surface coverage of films indeed lie in two distinct groups. 100 and 200 mM samples are seen to have comparable surface coverage, which are larger than the surface coverage

of 5, 10 and 50 mM samples. This result clearly indicates that by changing the assembly condition, it is also possible to control the physical properties of MWCNT/TiO_2 nanocomposite thin films.

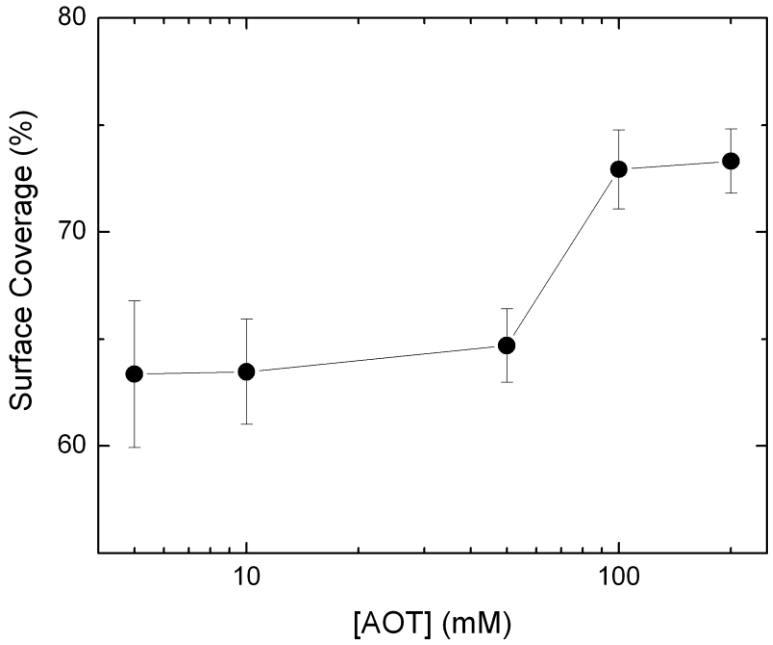

Figure 6.8. Surface coverage of 20–bilayer MWCNT/TiO_2 films as a function of concentration of AOT.

6.3.6 Enhanced Photocatalytic Activity of MWCNT/TiO_2 Films

As previously mentioned, the excellent electron accepting properties of CNTs could aid in suppressing the recombination of photogenerated electron–hole pairs. Furthermore, CNTs within nanocomposites increase the specific area available for adsorption of pollutants.[131] As a result of these effects, CNT/TiO_2 nanocomposite structures are expected to have enhanced photocatalytic activity compared to single–component TiO_2 structures.[131] The enhancement effect of MWCNTs is studied by comparing the

photocatalytic activity of 30–bilayer TiO_2 thin films assembled from 50 mM AOT suspension with and without MWCNTs. Single component TiO_2 thin films are prepared by removing MWCNTs from the MWCNT/TiO_2 nanocomposite films through high temperature calcination at 600°C for 1 hour. The characterization of calcined films using UV–Vis spectroscopy and scanning electron microscopy showed that MWCNTs are completely removed (See Figure 6.9 and Figure 6.10). In addition, the calcination of TiO_2 nanoparticles at 600°C for 1 hour showed little influence on the crystal structure and size of TiO_2 nanoparticles (see Figure 6.11 for X–ray diffraction of TiO_2). By removing MWCNTs via calcination, it is possible directly assess the effect of MWCNTs on the photocatalytic activity of TiO_2 nanoparticle thin films.**

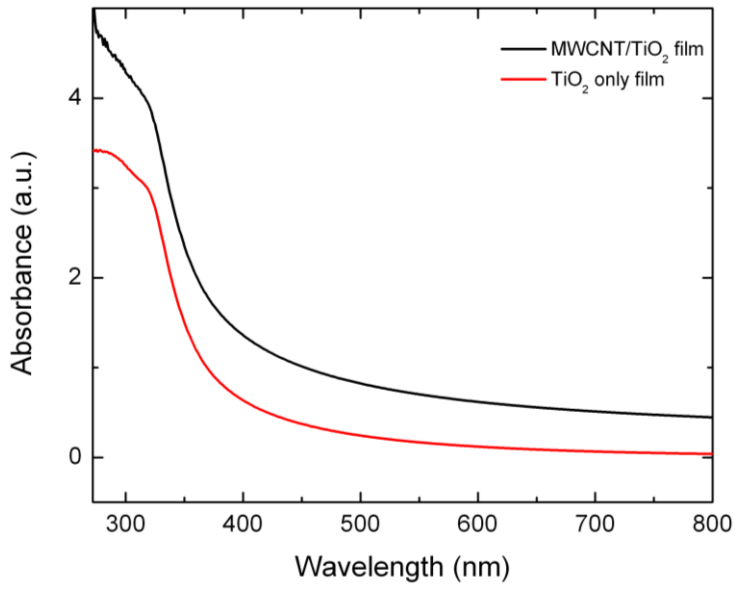

Figure 6.9. UV–Vis absorbance spectra for MWCNT/TiO_2 film (black line) and TiO_2 only film (red line)

** Although it would be desirable to compare the specific area of MWCNT/TiO_2 films to single–component TiO_2 films, MWCNT/TiO_2 LbL films with over 4000–bilayers (impractically large number of bilayers) would be required to determine the surface area of these films using the BET method

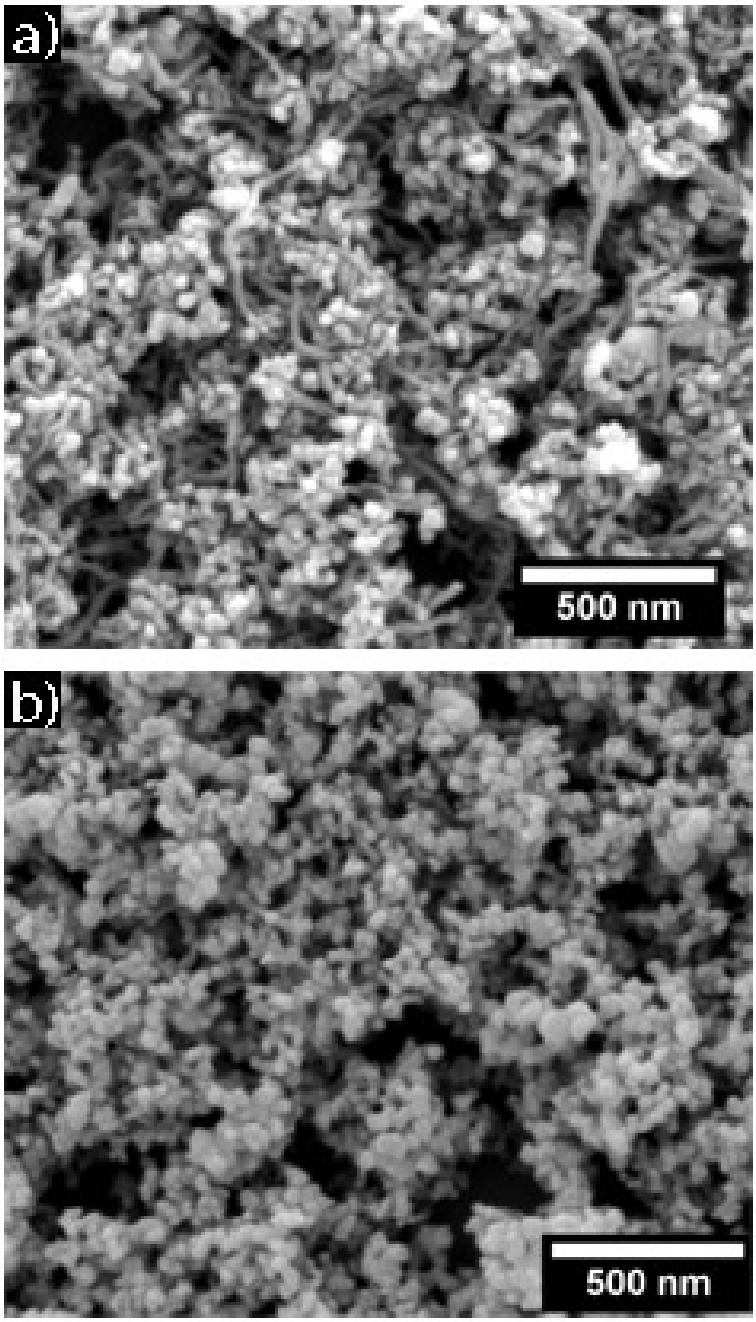

Figure 6.10. SEM images showing topography of (a) MWCNT/TiO_2 and (b) TiO_2 films.

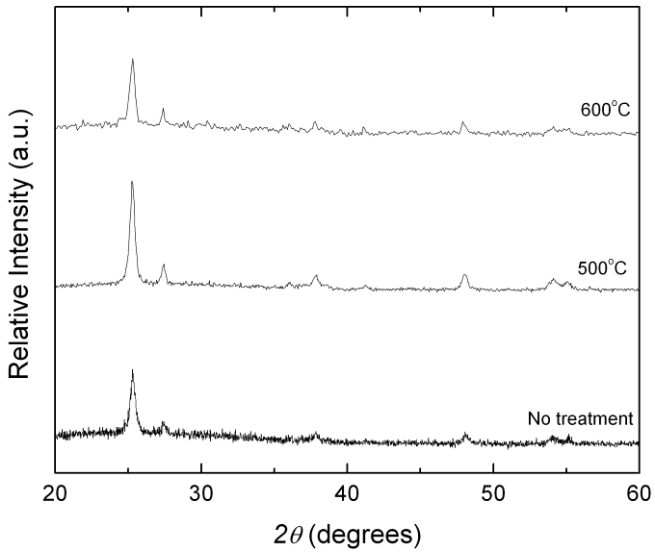

Figure 6.11. XRD pattern for (a) TiO_2–P25 calcined at 600°C for 1 hour and (b) untreated TiO_2–P25

The decomposition of a model contaminant (an organic dye, Porcion Red) by MWCNT/TiO_2 nanocomposite thin films under UV irradiation was monitored using UV–Vis spectroscopy. The photodegradation results shown in Figure 6.12 clearly show that the incorporation of un−oxidized MWCNTs enhances the photocatalytic activity of TiO_2 nanoparticle thin films. The kinetic analysis of dye decomposition under UV irradiation using a Langmuir–Hinshelwood model[158] indicates that the incorporation of MWCNTs leads to approximately two–fold increase in the pseudo–first order rate constant. It is possible that the residual AOT could adversely influence the photocatalytic activity of as–assembled MWCNT/TiO_2 films. Selective removal of AOT via thermal treatment at 400 °C under N_2, however, leads to a slight decrease in the rate constant compared to as–assembled MWCNT/TiO_2 films. This result could be due to a small loss of MWCNTs during the thermal treatment. Residual AOT in MWCNT/TiO_2 films undergoes

degradation during photocatalysis as evidenced by Fourier transform infrared spectroscopy (FTIR) results as shown in Figure 6.13.

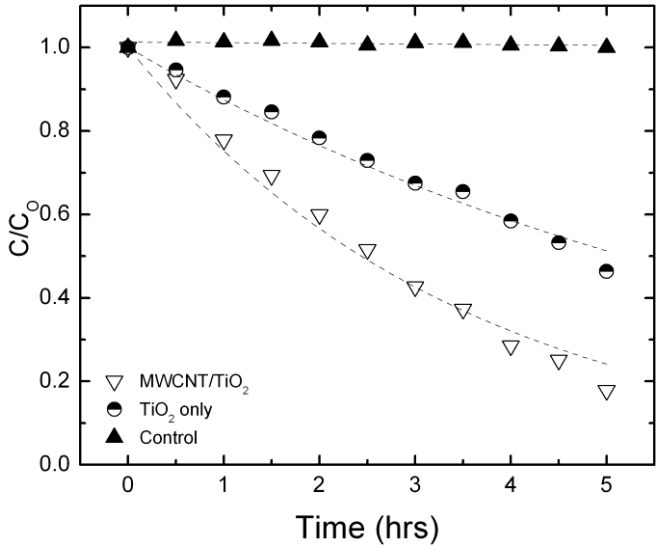

Figure 6.12. Comparison of photocatalytic activity for 30–bilayer 50 mM TiO_2 films with and without MWCNTs.

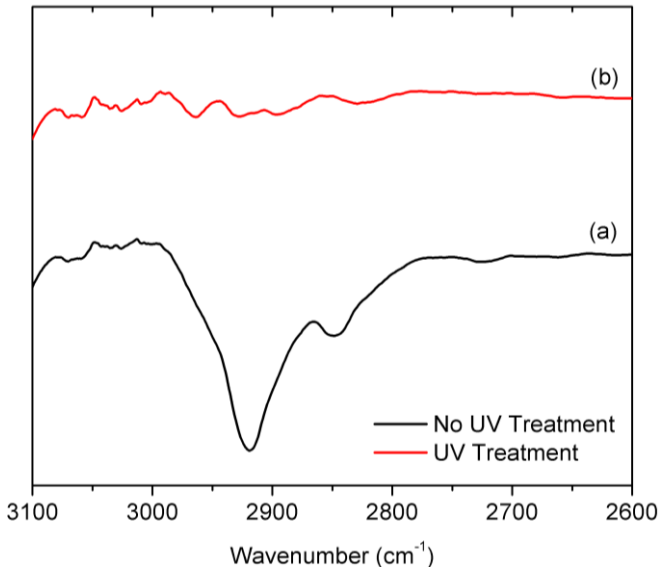

Figure 6.13. FTIR spectra for (a) MWCNT/TiO_2 nanocomposite before UV treatment (black) and (b) after UV treatment (red). Peaks between 3000 and 2800 cm^{-1} represent alkane groups of AOT.

The effect of assembly conditions on the photocatalytic activity of MWCNT/TiO_2 nanocomposite thin films was also investigated. The photocatalytic rate constants (k) for 25–bilayer MWCNT/TiO_2 nanocomposite thin films fabricated at different assembly conditions are summarized in Table 6.2. The results show that, in general, the photocatalytic activity of the nanocomposite films increases as a function of [AOT], which indicates that a positive correlation exists between the composition, conductivity and photocatalytic activity of these nanocomposite thin films. These results again illustrate that the properties of MWCNT/TiO_2 nanocomposite thin films assembled in non–polar media can be tuned by varying the assembly condition (i.e., the concentration of AOT).

Table 6.2. Rate constants of photocatalytic reactions using 25–bilayer MWCNT/TiO_2 films assembled with different [AOT]

[AOT] (mM)	***k*** (hrs^{-1})
5	0.42
50	0.52
100	0.53
200	0.58

6.4 Conclusions

In conclusion, conductive and photocatalytic MWCNT/TiO_2 nanocomposite thin films can be created by using LbL assembly in a non–polar solvent. LbL assembly in toluene is achieved by using the method developed in *Chapter 3* which involves using a charge–inducing agent, AOT, to impart a negative surface charge on MWCNTs and a positive surface charge on TiO_2. An advantage of this new approach in the generation of MWCNT/TiO_2 nanocomposites is that oxidation of MWCNTs is not necessary, thus preserving the efficacy of MWCNTs as an electron transporter. The incorporation of MWCNTs in these thin films significantly enhanced the photocatalytic activity of TiO_2 while the physicochemical properties of MWCNT/TiO_2 could also be varied by controlling the assembly condition.

Chapter 7. Electrophoretic Deposition of Nanomaterials from Non–Polar Media

7.1 Introduction

In *Chapters 3* and *6*, nanocomposite films were fabricated via LbL assembly of oppositely charged species in a non–polar solvent toluene. However, a drawback to using LbL assembly for fabricating nanocomposite films is the slow processing speed. For example, the assembly of ~ 1 μm MWCNT/TiO_2 films typically takes over 12 hours. Although the spray–assisted LbL assembly method could alleviate the slow processing speed, the choice of toluene as a working solvent poses as a health hazard since dispersions have to be sprayed onto the substrate as a fine mist. The spin–assisted LbL assembly, a combination of conventional LbL assembly and spin–coating routine, offers significantly faster assembly speeds than the conventional dip LbL assembly but is however limited to small substrates (~ cm^2).[159] In addition, both spin– and spray–LbL assembly methods tend to waste material.

The electrophoretic deposition (EPD) technique addresses the challenge faced with creating nanoparticle films via LbL assembly by offering a means to rapidly fabricate thick films over relatively large areas. EPD takes advantage of electrophoresis, the motion of charged colloids in dispersions under the influence of a dc electric field and deposition, the coagulation of particles to a dense mass.[160] The EPD process has been extensively used to generate coatings, shape freestanding objects, and for infiltration into

matrices.[161, 162] Advantages of EPD over other film fabrication techniques include its scalability, site–selectivity and control over deposition kinetics.[163] EPD is typically performed in solvents in which particles readily acquire charge such as water, alcohols and ketones.[162] EPD in non–polar solvents would be an advantageous process as electrolysis of the suspension solvent, especially in the case of water can be avoided. In addition, the absence of charged species in the solvent makes non–polar EPD a low current process therefore reducing ohmic heating.[161] A small number of reports have demonstrated EPD of nanocrystals in which organic ligands added during synthesis promotes charging in non–polar solvents.[163] These, nanocrystals charged by ligands can gain positive and negative charges, resulting in the deposition of materials on both electrodes.[164-166] This deposition on both electrodes is disadvantageous for the fabrication of complicated configurations such as tubes and helices in which the electrode configuration is not parallel.

One possible strategy to overcome this limitation of organic ligands is to use surfactant Aerosol–OT (AOT). AOT is shown in *Chapters 3, 4, 5* and *6* to better control the sign and magnitude of particle charge in non–polar solvents. In this present chapter, it will be shown that common particles charged with AOT and other amphiphiles can be used to fabricate nanocomposite films via EPD since these dispersions fulfill the basic prerequisites for EPD – charge stabilization, homogeneity and electrophoretic mobility.[162] In addition, the challenges faced with this new non–polar EPD will be discussed.

7.2 Experimental Section

7.2.1 Materials

Multi–walled carbon nanotubes (MWCNTs), carbon black (Conductex 7055 Ultra) and TiO_2 (P25) are obtained from Cheap Tubes Inc., Columbian Chemicals and Degussa respectively. PHSA–stabilized PMMA particles in decalin are purchased from Andrew Schofield (University of Edinburgh). Toluene, methanol and concentrated sulfuric acid are purchased from Fisher Scientific while Aerosol–OT (AOT), acetic anhydride, dichloromethane and thymol blue are purchased from Sigma–Aldrich. Polystyrene (MW ~ 190,000) is purchased from Scientific Polymer Products Inc.

7.2.2 Synthesis of Partially Sulfonated Polystyrene

Partially sulfonated polystyrene is prepared according to procedures described in literature.[167] Briefly, concentrated sulfuric acid combined with excess acetic anhydride in dichloromethane is used to synthesize acetyl sulfate. Appropriate amount of acetyl sulfate is added slowly into polystyrene in dichloromethane under gentle stirring at 40 ^{o}C. The sulfonation reaction proceeds for 4 hours followed by termination of the reaction by addition of methanol. The addition of methanol is used to precipitate the polymer after which the precipitated polymer is washed multiple times with DI water. The polymer is dried in a vacuum oven around the glass transition temperature (T_g). The sulfonic acid content is determined by titration with a standard solution of NaOH with thymol blue as indicator.

7.2.3 Preparation of Particle Dispersions

0.5 wt. % TiO_2 and MWCNTs are prepared in AOT/toluene and sonicated for 1 hour to obtain fine suspensions. To formulate MWCNT/TiO_2 dispersions, a set volume of MWCNTs is added to TiO_2 to obtain MWCNT volume contents ranging from 0.5 – 5 %. The mixture is sonicated with a probe sonicator for 20 minutes to get homogenous dispersions. Carbon black in SPS dispersions are prepared by firstly sonicating 1 wt % carbon black in pure toluene for 1 hour. Next, 400 mM of SPS in toluene is prepared followed by dilution to 200, 100, and 20 mM SPS/toluene. A set volume of the 1 wt % carbon black suspensions is vigorously shaken to disperse the particles, and then mixed with an equal volume of each SPS/toluene solution to yield 0.5 wt. % CB dispersions in SPS/toluene. PMMA particles in decalin are transferred into pure dodecane through multiple centrifugation and redispersion steps. A set volume of dodecane containing PMMA particles is transferred directly into AOT/dodecane to obtain the desired volume fraction.

7.2.4 Solution and Particle Characterization

Electrophoretic mobility and particle size measurements are performed with a Beckman Coulter Delsa Nano–C. Electrophoretic mobility measurement are made for each suspension using a flow cell at an electric field of 85.2 V/cm. The solution conductivity of AOT/toluene and SPS/toluene is measured with a handheld conductivity meter (D–2 Inc. model JF–1A–HH).

7.2.5 Electrophoretic Deposition

EPD is performed inside a glass cuvette 4 cm wide and with a 1 cm path length. Two conducting fluorine–doped tin oxide (FTO) electrodes (Hartford Glass Co. Inc.) are connected to the negative and positive terminals of a high voltage dc power supply unit (Stanford Research Systems, model PS350). The dispersion for EPD is filled into the cuvette after which the power supply unit is switched on to the desired voltage. The power supply unit is turned off after the desired time and a syringe pump (Harvard Instruments, model PhD Ultra) is used to withdraw the dispersion from the cuvette at a set withdrawal rate. The electrode is subsequently removed from the cuvette and allowed to dry in air. EPD on insulating plastic sheets is performed by fixing the plastic sheet onto a stainless steel electrode followed by repetition of the aforementioned procedure.

7.2.6 Sedimentation Image Analysis

Two stainless steel electrodes 1 cm wide are placed on the opposite walls of a plastic cuvette 1 cm wide after which 3 mL of PMMA dispersion is added into the cuvette. A dark background is placed behind the cuvette as well as on both sides of the cuvette in order to improve the contrast between sediment and supernatant. The two stainless steel electrodes are connected to the positive and negative terminals of the high–voltage power supply unit. Parafilm is wrapped around the top of the cuvette and connecting leads in order to minimize interference within the dispersion from air. A digital camera is used to record the sedimentation process over a 15–minute interval. The recorded video files are converted to multiple image files, which provide a snapshot of the sedimentation process

at different time points. ImageJ is used to crop each image at the mid–point of the cuvette (see dashed line in Figure 7.4) to a new image one pixel wide. ImageJ is subsequently used to vertically stack each single pixel image to form an image montage of the sedimentation process. The change in sedimentation height with time is tracked by adjusting the threshold of each single pixel image with ImageJ to give two distinct regions corresponding to the sediment and supernatant. Since the image file is one pixel wide, the area fraction of the sediment region (as calculated with ImageJ) corresponds to the height of the sediment.

7.2.7 Film Characterization

Scanning electron microscopy (SEM) images of films are taken using an FEI 600 Quanta FEG ESEM at 5 kV and at a working distance of 10 mm. Thickness measurements are made with a Zygo NewView 6K series optical profilometer. To get an averaged film thickness, height profiles along a line segment are integrated and normalized with the length of the profile. TGA measurements are taken with a TA Instruments SDT Q600. Samples for TGA are prepared by scraping off films into a platinum TGA pan. The pan temperature is ramped from room temperature to 1000 ^{o}C at a ramp rate of 10 ^{o}C/min.

7.3 Results and Discussion

7.3.1 EPD of Surfactant Stabilized Particles from Non–Polar Solvent for the Generation of MWCNT/TiO_2 Nanocomposite Films

In *Chapter 6* of this thesis, the charge of TiO_2 was shown to be positive for all AOT concentrations, (Figure 6.2b) thus making these dispersions favorable for EPD. EPD of TiO_2 dispersions in 10 mM AOT/toluene at 300 V/cm is found to form ~ 3.5 μm TiO_2 films exclusively on the negative FTO electrode within 20 seconds. MWCNT/TiO_2 will be used as a model system to demonstrate the viability of the non–polar EPD technique for creating nanocomposite films. To create such nanocomposite films, dispersions of TiO_2 in AOT/toluene containing different weight fractions of MWCNTs ranging from 0 – 5 vol % are formulated. These dispersions are relatively stable for hours, unlike those used for heteroaggregation tests in *Chapter 6* (Figure 6.3). In that instance, the volume ratio of MWCNTs to TiO_2 was 1:1. The EPD of the MWCNT/TiO_2 dispersions with varying concentration of MWCNTs gives ~ 6 μm films with increasing darkness, indicative of the MWCNT content (Figure 7.1). Scanning electron microscopy (SEM) images reveal that the films formed are highly porous (Figure 7.2), furthermore, the MWCNTs are homogenously dispersed throughout the bulk of the film, making them advantageous for energy conversion devices such as dye–sensitized solar cells (DSSCs). The utility of using this non–polar EPD method for creating nanocomposite films is that thick films can be rapidly cast on a substrate. Furthermore, unlike in aqueous EPD, MWCNTs do not need to undergo harsh chemical oxidation treatment for charge stabilization,[168, 169] in turn, preserving the unique electronic properties of the MWCNTs.

In addition, this method offers a means of incorporating more than two components within the film by simply changing the dispersion composition.

.

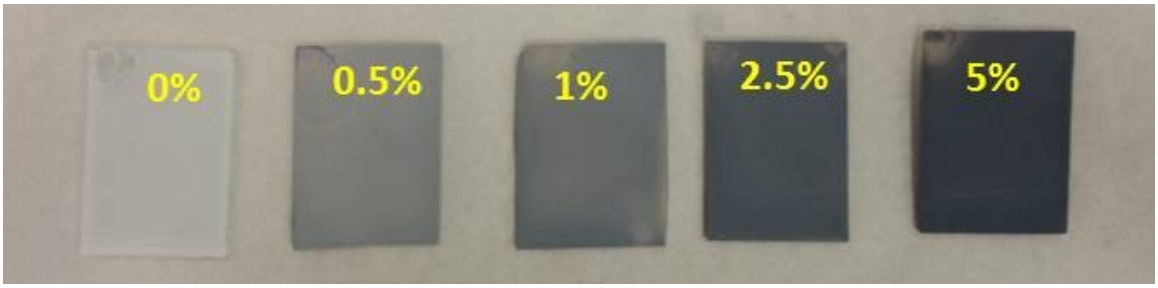

Figure 7.1. MWCNT/TiO_2 films formed by EPD of dispersions in AOT/toluene

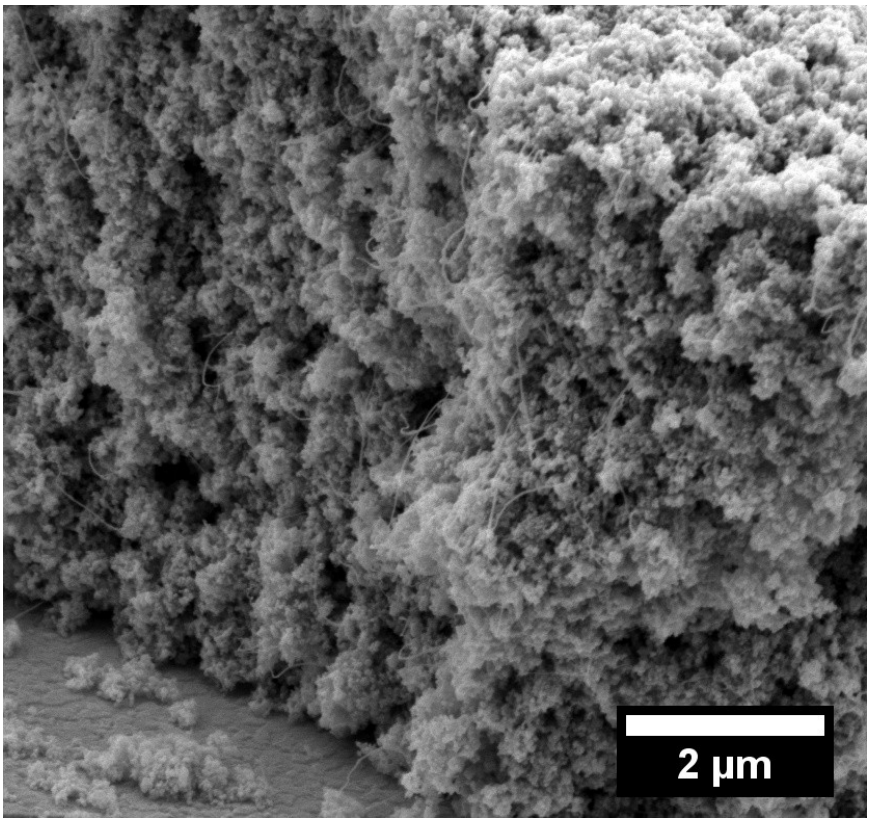

Figure 7.2. Cross–section SEM image of MWCNT/TiO_2 films formed via EPD

Although the non–polar EPD approach resolves the third limitation of nanoparticle LbL presented in the thesis *Introduction*, the thickness of the films formed is found to vary significantly from the top to bottom of the electrode. To test if the change in thickness is specific to the amphiphile used, AOT, a different amphiphile, OLOA (polyisobutylene succinimide) is used. The long polyisobutylene tail allows OLOA to act as a steric stabilizer in addition to a charge control agent.[72] Figure 7.3 shows that the thickness nevertheless increases down the electrode for EPD films formed from TiO_2 in OLOA/toluene. This non–uniformity is undesirable for most applications of nanocomposite films since thickness influences the performance of the film. The next section will probe the origin of the thickness increase.

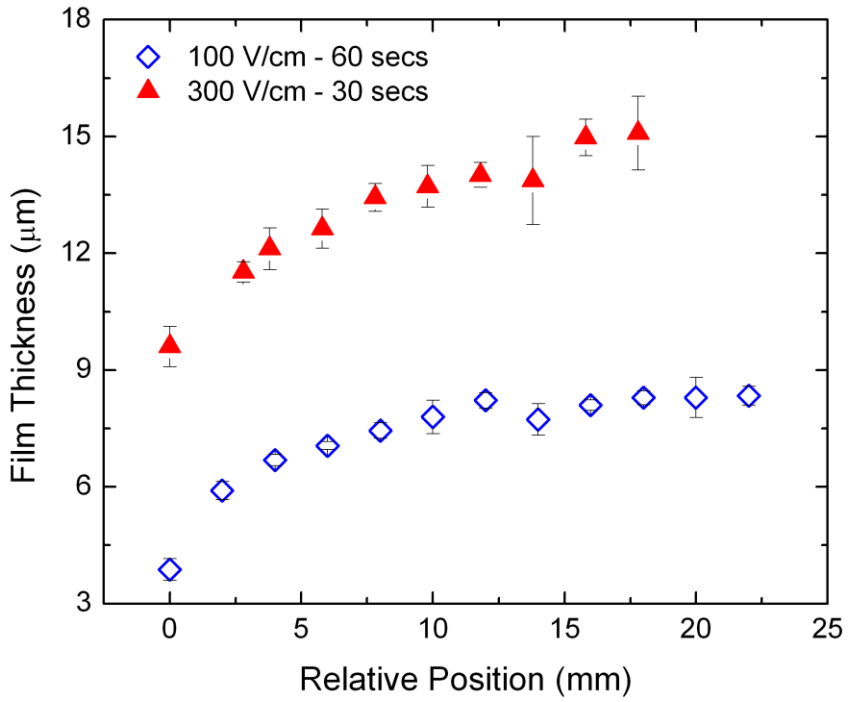

Figure 7.3. Change in film thickness vs. relative position for electrophoretic deposition (EPD) of TiO_2 dispersed in OLOA/toluene. The relative position is the distance from the topmost part of the film denoted by zero.

7.3.2 Field–Induced Sedimentation of Charged Particles in Non–Polar Solvents

To probe the origin of EPD film non–uniformity, a model system of charged PMMA particles in AOT/dodecane in a dc electric field is used. In the experimental setup used (Figure 7.4) a dc electric field E is generated by applying a constant voltage V across two parallel stainless steel electrodes ~ 1 cm apart. Upon turning on the dc electric field, PMMA particles dispersed in AOT/dodecane within the cuvette begin to sediment rapidly with time. The sedimentation of PMMA particles is tracked by recording videos of the process with a standard digital camera. From these videos, the midpoint pixel line (dashed line in Figure 7.4) between two electrodes is used to create the sedimentation montages shown in Figure 7.5.

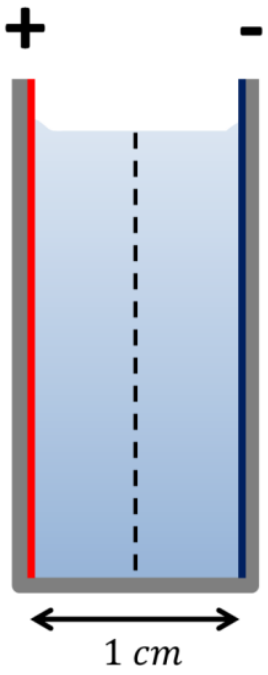

Figure 7.4. Illustration of the experimental setup used in this study showing PMMA dispersion in 1 cm wide plastic cuvette, electrodes placed next to cuvette walls and single pixel line (dashed line) used for image analysis.

Figure 7.5a shows a typical montage created from the recorded videos. From this montage, it is clear that the PMMA particles are sedimenting over the 15–minute interval used. Multiple control experiments are performed to probe the origin of the sedimentation behavior. The first experiment involves using short electrodes one–third the size of the electrodes used in Figure 7.5a (the length of electrodes are depicted by red lines). Figure 7.5b shows that upon turning on the dc field, sedimentation only occurs for parts of the dispersion within the dc field formed by the short electrodes. The sharp end to sedimentation at the bottom of the short electrodes implies that the dc field does not extend beyond this area. Next, a long electrode with the dc field on for 5 minutes is used. The sedimentation of particles immediately halts after turning off the dc field (Figure 7.5c), leaving the dispersion stable. In Figure 7.5d, the dc field is intermittently turned on–and–off after 5–minute intervals. This result, along with those from Figure 7.5b,c imply that the applied dc field induces the observed sedimentation behavior. The role of AOT in this process is probed by applying a dc field (formed by a long electrode) to dispersions without AOT. In this case, the PMMA particles are found to undergo negligible sedimentation as shown in Figure 7.5e. In fact, these dispersions are almost as stable as PMMA particles in pure dodecane with no applied dc electric field (Figure 7.5f). Overall, the sedimentation behavior observed in Figure 7.5a is a result of two effects: (1) the applied dc electric field and (2) the presence of AOT in the dispersion.

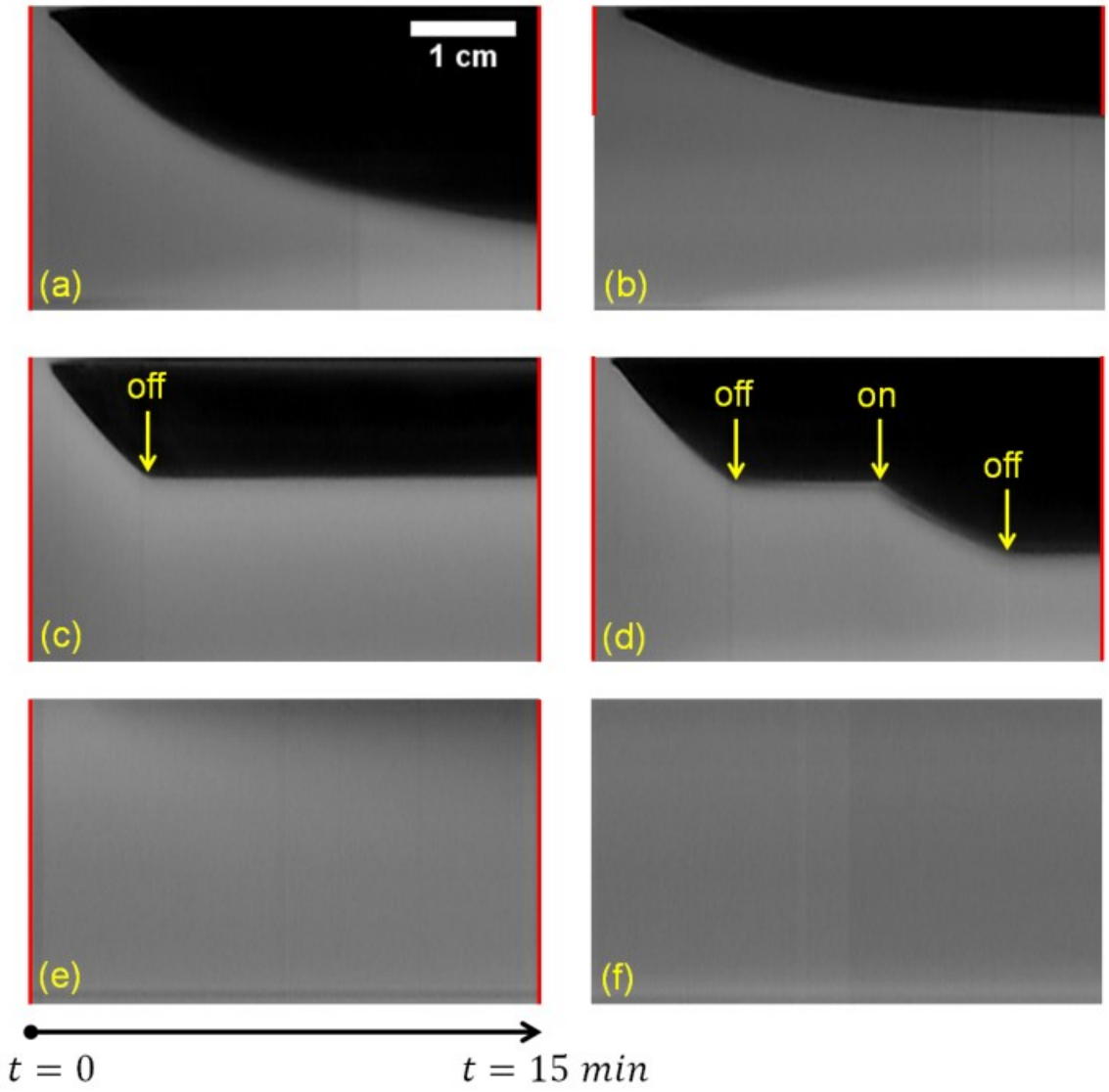

Figure 7.5. Time lapse montages of 0.5 wt% PMMA particles in 100 mM AOT/dodecane with an applied dc electric field of 300 V/cm on for 15 minutes using (a) long and (b) short electrodes. In (c), the dc field is on for 5 mins and (d) intermittentally on–off–on–off after 5 min intervals. In (e) and (f), PMMA particles are in pure dodecane with 300 V/cm dc field and no applied dc field respectively. The parrallel vertical red lines depict the length of electrodes used.

7.3.2.1 Effect of Concentration of AOT and Particles on the Sedimentation Profile

In the previous section, it was observed that particle sedimentation does not take place in the absence of AOT. This section investigates the effect of AOT concentration ([AOT]) on the sedimentation behavior of particles. In addition, the effect of PMMA particle concentration (ϕ) on the sedimentation profiles is explored. Figure 7.6a summarizes the types of sedimentation profiles observed for different combinations of [AOT] and ϕ. These can be classified as follows: (1) "slow" as shown by the red region and as exemplified by Figure 7.6b, (2) "moderately diffuse" as shown by the green region and as exemplified by Figure 7.6c, and (3) "sharp" as shown by the blue region and as exemplified by Figure 7.6d. For a constant ϕ, the sedimentation profile changes from negligible in the absence of AOT (Figure 7.5e) to slow to moderately diffuse and finally to sharp. Likewise, similar transitions in the sedimentation profiles are observed for dispersions with constant [AOT] and increasing ϕ.

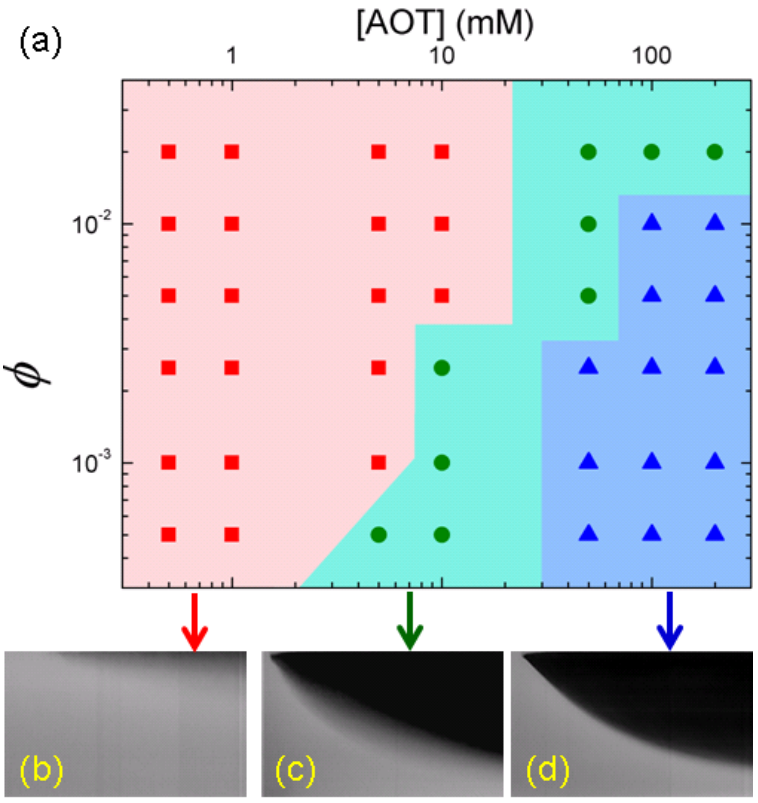

Figure 7.6. (a) Sedimentation profiles of PMMA particles for different combinations of [AOT] and ϕ. The red region is characterized by diffuse/slow sedimentation as shown in (b), green by moderately diffuse sedimentation front as shown in (c) and blue by sharp sedimentation front as shown in (d). The dc field is kept at 300 V/cm.

To compare the effect of [AOT] or ϕ on particle sedimentation, the image analysis procedure described in the Experimental Section is used to convert the sedimentation montages to normalized heights (*H/Ho*) vs. time (*t*) plots. Here, *H* represents the interface height at a specified time *t* and *Ho* represents the initial height at time $t = 0$. The analysis procedure is performed for sharp sedimentation conditions (blue region in Figure 7.6a) since the sedimentation interface is well defined and can be tracked with high reliability. The normalized heights *H/Ho* in Figure 7.7a show that for a fixed dc field strength of 300 V/cm and ϕ=0.005, the concentration of AOT has little effect on the sedimentation

profile of the dispersions with time. Furthermore, the overlapping data points at all times imply that the average sedimentation rate, defined as *(H–Ho)/t*, remains constant for all [AOT]. Likewise, the overlapping data points at early times in Figure 7.7b also suggests that the initial sedimentation rates are comparable for conditions in which ϕ varies while the dc field strength is fixed at 300 V/cm and [AOT] at 100 mM. However, at longer times, *H/Ho* begins to deviate for different ϕs'. Specifically, at a fixed time point (for example, 800 seconds), *H/Ho* begins to decrease with ϕ. This implies that the average sedimentation rate decreases with ϕ.

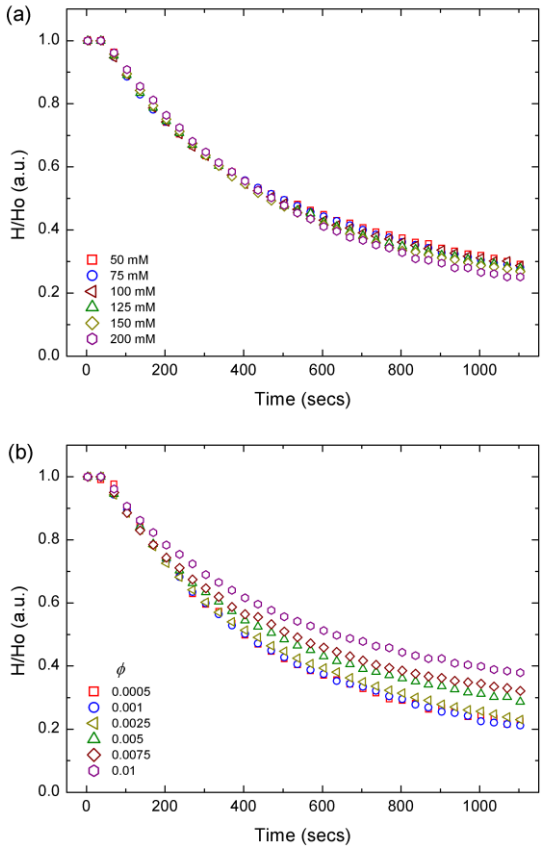

Figure 7.7. Change in normalized sedimentation height with time (a) for 0.5 wt % PMMA particles in DC field of 300 V/cm and variable [AOT] and (b) increasing ϕ for PMMA particles in 100 mM AOT/dodecane in DC field of 300 V/cm.

7.3.2.2 Effect of Processing Parameters on Sedimentation Height

Given that the dispersion conditions used ([AOT] and ϕ) can have an effect on the sedimentation profile, it is plausible that the processing parameters, specifically applied electric field strength E can also influence the sedimentation behavior of PMMA particles. Figure 7.8a confirms that the *H/Ho* vs. time profile for a fixed [AOT] and ϕ indeed changes with the applied dc field strength E. In general, the initial sedimentation velocity (Figure 7.8b) as determined by the slope of H vs. time for short times, scales linearly with E. For longer times, the differences in *H/Ho* at a fixed time point suggests that the average sedimentation rate increases with applied field strength for $E \leq 300$ V/cm and becomes comparable for 400 and 500 V/cm conditions. Furthermore, the induction time (i.e. the time elapsed before sedimentation begins for particles located at the single pixel image processing line shown by the dashed line in Figure 7.4), rapidly decreases and plateaus as E increases from 50 to 500 V/cm (Figure 7.8c).

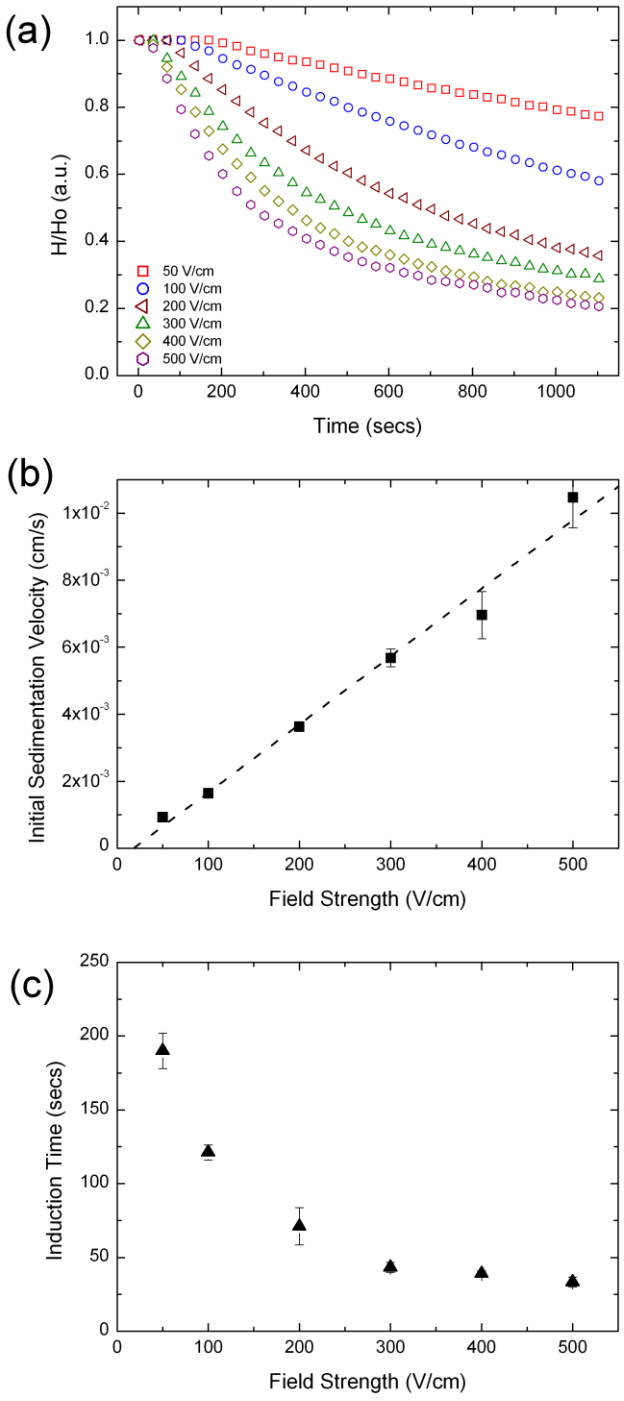

Figure 7.8. Change in (a) normalized sedimentation height with time, (b) initial sedimentation velocity with applied dc field strength and (c) induction time with dc field strength. Samples are 0.5 wt % PMMA particles in 100 mM AOT/dodecane. Error bars represent standard deviations of three measurements.

7.3.2.3 Proposed Mechanism for Field Induced Sedimentation

To identify the origin of the rapid sedimentation behavior observed, the dimensionless Péclet number of a spherical particle $Pe = \frac{4\pi a^4 g(\rho_c - \rho)}{3k_B T}$ (i.e. the ratio between two energy terms – energy gained due to settling and thermal energy) is examined.[170] Here, a represents the particle radius while g is the gravitational acceleration, ρ the density of the fluid and ρ_c the density of the sphere. Based on this balance between settling and thermal energy, it follows that particles should sediment (the non–Brownian limit) when $Pe >> 1$. For the PMMA particles dispersed in AOT/dodecane, $a \sim 85$ nm yielding a $Pe << 1$, hence Brownian diffusion dominates and particles do not settle and remain stable for prolonged times as shown in Figure 7.5f. However, the rapid sedimentation of PMMA particles in the presence of the dc field suggests that $a \gtrsim 0.7\mu m$, the critical radius into the non–Brownian regime (i.e. where $Pe \sim 1$). This calculation suggests that particle aggregates form within the applied dc field leading to their sedimentation.

To show such aggregation, optical microscopy is used to observe larger (~3μm) PMMA particles dispersed in 100 mM AOT/dodecane within a dc field. Figure 7.9a shows that at early times, particles are initially well dispersed in AOT/dodecane, however, particles begin to move towards the positive electrode and form linear aggregates as shown in Figure 7.9b,c. In fact, the formation of columns of particles for suspensions within high dc fields is well studied and has been utilized as electrorheological (ER) fluids.[171, 172] In such systems, particles are polarized by the applied electric field resulting in an effective dipole moment for each particle. The induced dipole–dipole moment between particles results in their linear aggregation along

the electric field lines as seen in Figure 7.9b,c.[172] Close examination of Figure 7.9c shows that not all linear aggregates comprise of the same number of particles, instead, there is a distribution in the number of particles forming linear aggregates. These linear aggregates formed most likely increases the hydrodynamic radius of the aggregates and eventually lead to the rapid sedimentation of PMMA dispersions in dc fields.

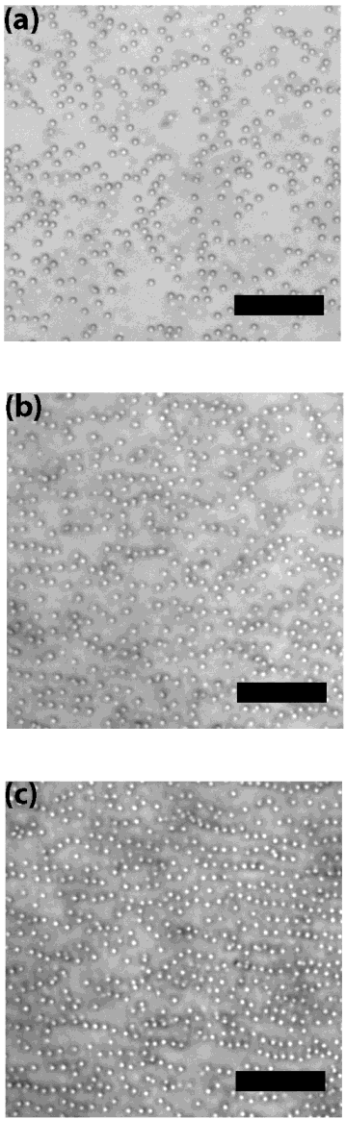

Figure 7.9. Optical microscopy images of ~3 μm PMMA particles in 100 mM AOT/dodecane in a dc field after (a) 1 sec, (b) 60 secs and (d) 80 secs. The scale bar is 40 μm.

To understand the formation of linear aggregates within the dc field, the conductivity of AOT/dodecane solutions as well as the electrophoretic mobility (a measure of particle charge) of PMMA particles dispersed in AOT/dodecane is measured for different dispersion conditions. Pure dodecane is highly insulating, however, the conductivity of AOT/dodecane solution is believed to arise from the presence of charged reverse micelles formed through the spontaneous disproportionation process whereby two neutral micelles form oppositely charged micelles ($2M^o \leftrightarrow M^+ + M^-$). Although only a tiny fraction (~ 10^{-5}) of neutral micelles become charged through this process, the overall increase in the number of charged reverse micelles with the amount of added AOT (i.e. [AOT]) results in the increase in solution conductivity with [AOT] shown in Figure 7.10a. In Figure 7.10b, the electrophoretic mobility of PMMA particles is found to be invariant for ϕ = 0.005 and with relatively high [AOT] between 50 – 200 mM as shown by the black symbols and bottom axis. This result agrees with previous studies that have shown high charge for polymeric particles at low CCA concentrations followed by a gradual plateau in the charge at higher CCA concentrations.[112, 114] In addition, for a fixed [AOT] of 100 mM, the electrophoretic mobility of PMMA particles does not vary significantly for ϕ up to 0.0075 as shown be the red symbols and top axis in Figure 7.10b. The decrease in the magnitude of electrophoretic mobility for ϕ = 0.01 is possibly due to double–layer overlap[173] which occurs as the distance between two colloids approaches the screening length κ^{-1}.

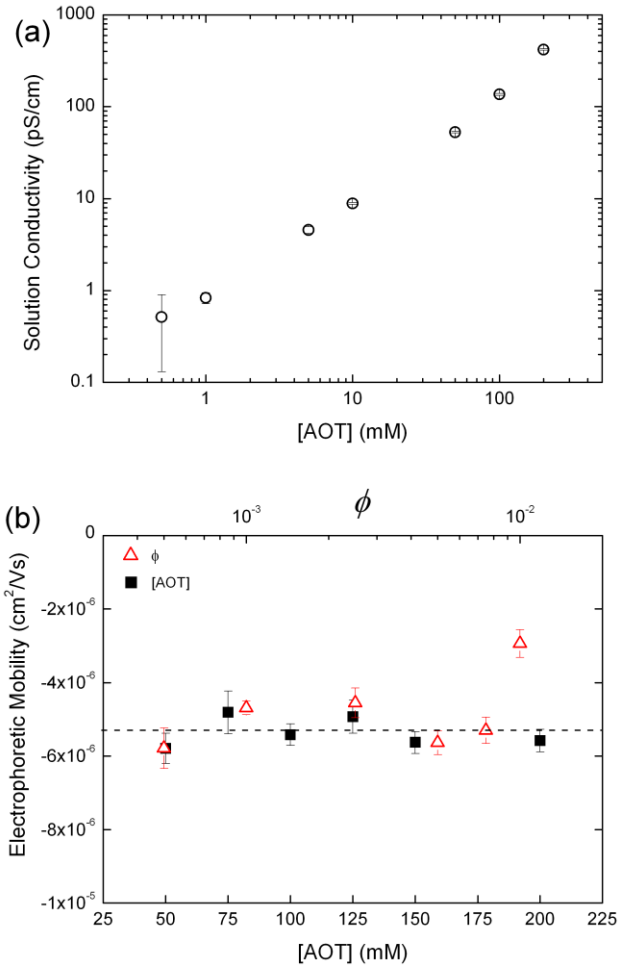

Figure 7.10. (a) Change in solution conductivity of AOT/dodecane for increasing [AOT] and **(**b**)** Electrophoretic mobility of 0.5 wt% PMMA particles for variable [AOT] (bottom axis) and for variable concentration ϕ of PMMA particles in 100 mM AOT/dodecane (top axis). Error bars represent standard deviations of three measurements for (a) and six measurements for (b).

As previously mentioned, the sedimentation of PMMA particles occurs only for dispersions doped with AOT. This result agrees with a finding in which sterically stabilized particles of PMMA in oil were found to be ineffective as ER fluids when free of moisture or surfactants.[171] In fact, additives such as surfactants are often added to ER formulations to promote particle polarization. These additives are believed to mediate ionization, and polarization ascribed to distortion of the double–layer by electric fields[171]

or to increase the conductivity on particles and thus enhance interfacial polarization.[174] In turn, the ER response is dependent on ion content and particle surface area.[175] In the system used in this study, the AOT reverse micelles formed in solution yield a double–layer, which can be polarized under the influence of the electric field leading to the linear aggregation of particles. The ratio of reverse micelles to particle surface area is found to affect the nature of the sedimentation front as shown in Figure 7.6. In general, for a fixed ϕ, the sharpest sedimentation front occurs for high [AOT] in which more charged reverse micelles are present (as implied by the increase in solution conductivity with [AOT] in Figure 7.10a), thus facilitating the polarization and linear aggregation process. The electrophoretic mobility (Figure 7.10b), however, has minimal influence on the sedimentation process; for example, dispersions with $5 \times 10^{-4} \leq \phi \leq 5 \times 10^{-3}$ have comparable electrophoretic mobilities and yet have different average sedimentation velocities as shown in Figure 7.7b.

The aggregation kinetics of colloids in a dc field is helpful for understanding the changes in sedimentation rate for different dispersions (i.e., [AOT] and ϕ) and processing conditions (dc field strength E). For three–dimensional systems, the average size s of linear aggregates scales as $s \propto E\phi^{0.5}t^{0.5}$.[176] The scaling of $s \propto E$ implies that larger linear aggregates will form with increasing applied field strength E. Hence, this increase in aggregate size with E will translate to an increase in the initial sedimentation velocity as well as average sedimentation rate as observed in Figure 7.8a,b. The scaling of $s \propto \phi^{0.5}$ also implies that larger linear aggregates should form with increasing ϕ. One would expect that the average sedimentation velocity should increase with ϕ (i.e. at a fixed time

point, the normalized sedimentation height *H/Ho* should decrease with ϕ), however, the opposite effect whereby the average sedimentation velocity decreases with ϕ is rather observed. This decrease in average sedimentation velocity is most likely a result of hydrodynamic/crowding effects retarding the sedimentation process as ϕ increases .[177]

7.3.2.4 Effect of Electric Field – Induced Sedimentation on Electrophoretic Deposition of Charged Colloids in Non–Polar Media

The non–uniformity in non–polar EPD films formed as shown in Figure 7.3 can be attributed to the rapid field–induced sedimentation of charged particles during the EPD process. As sedimentation proceeds with time, a concentration gradient forms down the dispersion such that the bottom portion is more concentrated than the top at any given time. Since the particle concentration increases down the dispersion container, the number of particles capable of depositing will also increase down the electrode thus resulting in non–uniform EPD films. Figure 7.7b showed that the sedimentation rate slows with increasing ϕ, therefore, a possible way to circumvent this problem would involve increasing the EPD dispersion concentration. Furthermore, stirring could be used to gain homogenous dispersions although the stirring rate would affect the deposition kinetics.[178]

7.3.3 EPD of Polymer Stabilized Particles

The majority of this thesis has used an amphiphile AOT to charge and stabilize particles in non–polar solvents, however, an acid co–polymer, partially sulfonated polystyrene (SPS) with a ~3 % sulfonation level (henceforth denoted as SPS3) has also been found to be an excellent dispersant for particles in non–polar solvents. In fact, SPS3 tends to charge carbon black such that the charge is negative below a 1 mM concentration and positive above this concentration as shown below in Figure 7.11. At this point, the charging mechanism of SPS is unclear; however, it is quite plausible that particles remain dispersed by both electrostatic repulsion and steric stabilization.

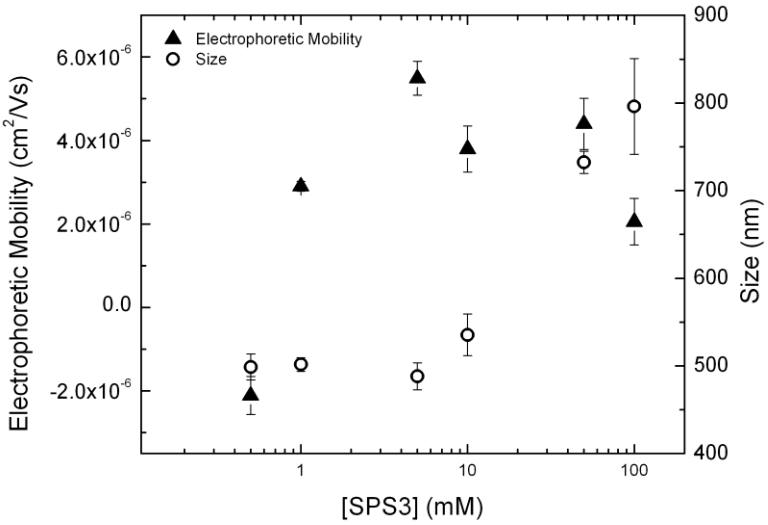

Figure 7.11. Change in electrophoretic mobility (left axis – triangle symbols) and size (right axis – circle symbols) of carbon black particles dispersed in SPS3/toluene.

The charged CB dispersed in SPS3/toluene is used for EPD on a conducting FTO electrode. In the EPD process, the mass of deposited particles (which is proportional to the thickness) scales with time t, applied potential E and particle zeta potential ζ.[162] Figure 7.12 shows that these three parameters can indeed be used to control the thickness

of CB/SPS3 films. For example, in Figure 7.12a, the thickness of films formed increases monotonically with time, which is typical in polar EPD.[160] Furthermore, for fixed deposition times, an increase in the applied field strength *E* from 200–400 V/cm systematically increases the thickness of films. Figure 7.12b shows that the charge of particles, as controlled by [SPS3] (see Figure 7.11) can also be used to control the thickness of the CB/SPS3 films.

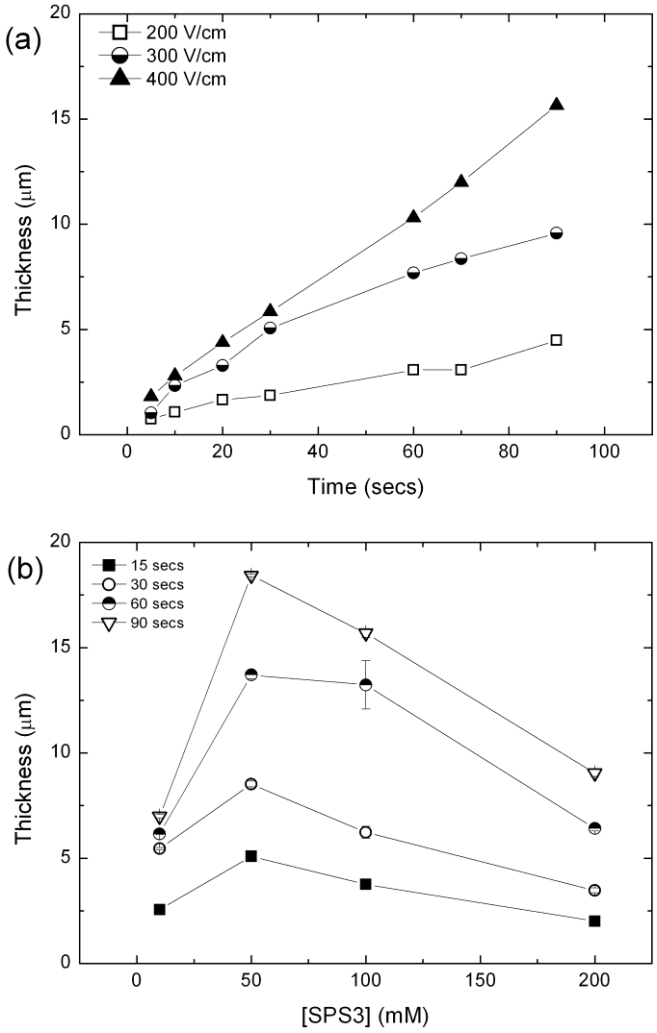

Figure 7.12. Change in film thickness (a) with time for carbon black dispersed in 10 mM SPS3/toluene and at different dc field strengths and (b) with SPS3 concentration for different deposition times and a dc field strength of 400 V/cm.

Scanning electron microscopy (SEM) images of the CB/SPS3 films formed (Figure 7.13) reveal that the films are highly porous. SPS3 appears to form a conformal layer over CB particles rather than fill the void space between CB particles. This can be attributed to the low composition of SPS3 within the film, ranging from ~ 8 – 17 wt % with increasing [SPS3] as shown in Figure 7.14.

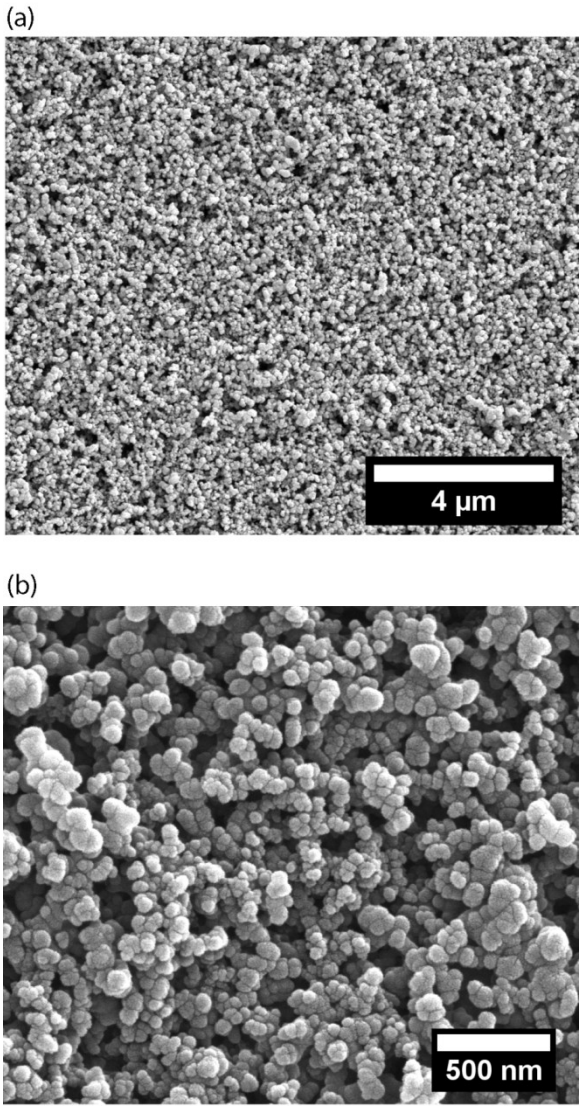

Figure 7.13. SEM image of CB/SPS films formed using 10 mM SPS.

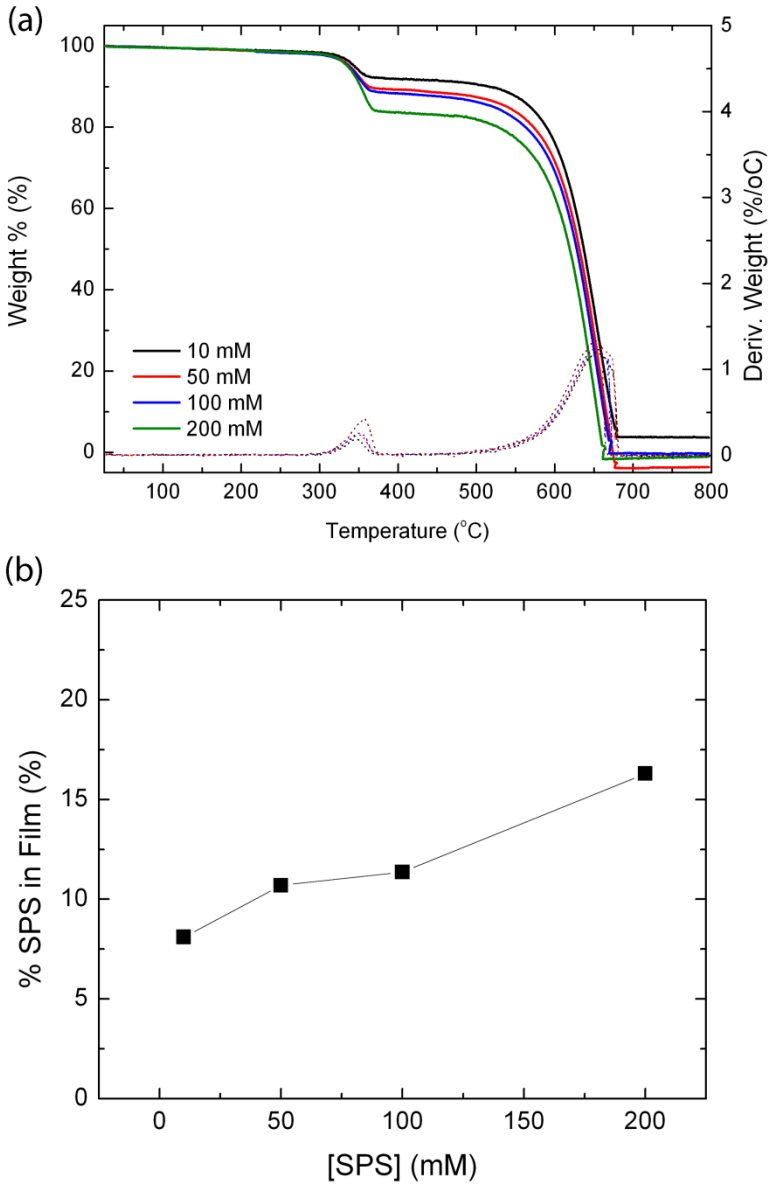

Figure 7.14. (a) TGA thermogram of CB/SPS film. The solid lines represent weight % change with temperature (left axis) while the dashed line represents the derivative of weight with respect to temperature (right axis). (b) Change in composition of CB/SPS films with concentration of SPS in CB/SPS dispersions.

The deposition of materials via EPD is typically performed on conductive substrates. EPD on non–conducting surfaces has been performed on porous supports in which a "conductive path" forms between the pores of the non–conducting substrate.[179] EPD on

polymer surfaces has been limited to deposition on ultra–thin layers of co–polymers[180] or conductive plastic substrates which are typically expensive.[181] However, SPS3–stabilized particles in toluene are found to deposit well on thick insulating polymer sheets, for example, Figure 7.15 shows CB/SPS3 deposited on Saran™ wrap. While the plain sheet is insulating (Figure 7.15a), the sheet covered with CB/SPS3 is found to be highly conductive (Figure 7.15b) due to percolation of the conductive CB particles. Furthermore, the sheet retains some degree of its original flexibility (Figure 7.15c).

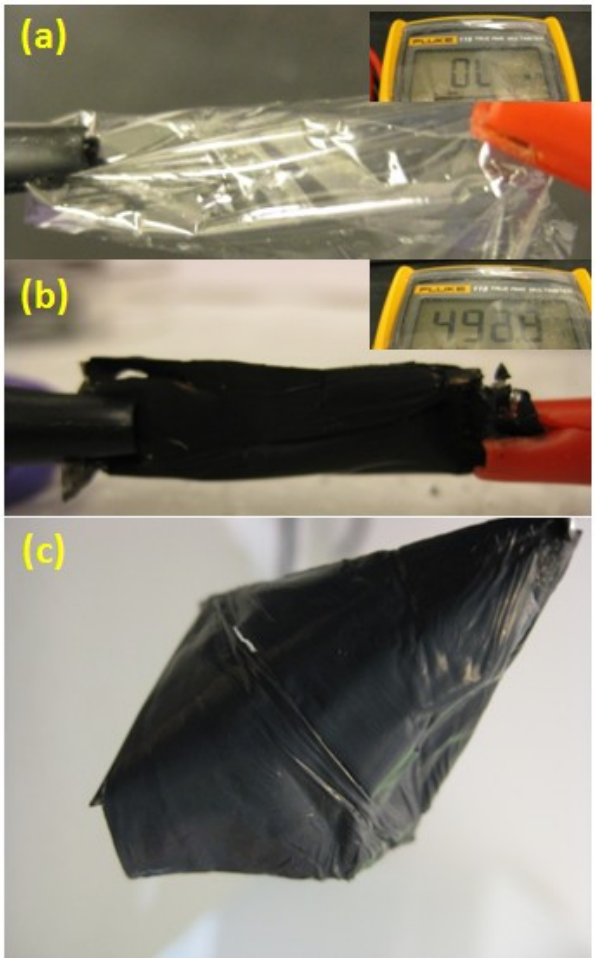

Figure 7.15. Photograph of Saran™ wrap (a) with insert showing sheet is not conductive, (b) coated with CB/SPS with insert showing that the sheet is conductive and (c) close up picture of Saran™ wrap coated with CB/SPS.

Although the exact mechanism leading to deposition on insulating surfaces remains unclear, it is more than likely that the absence of charge carriers, as noted by the low solution conductivity of SPS/toluene compared to AOT/toluene (Figure 7.16) plays a critical role in the deposition process.

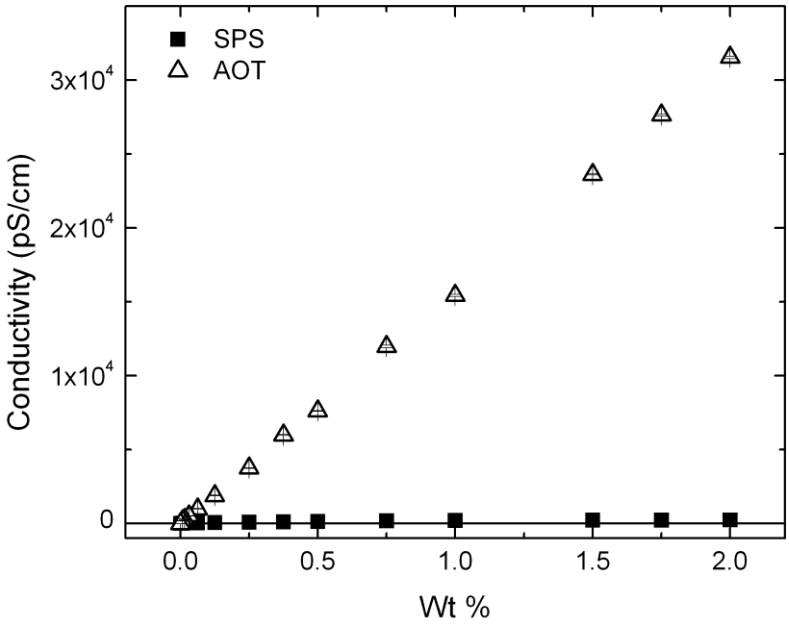

Figure 7.16. Comparison between conductivity of SPS/toluene and AOT/toluene solutions.

7.4 Conclusions

In conclusion, the limitation of nanoparticle LbL to slow speeds is addressed in this chapter by using an alternative film fabrication technique, EPD, to fabricate nanocomposite films. EPD is achieved by using surfactant AOT to charge and disperse TiO_2 and MWCNT/TiO_2 in a non–polar solvent toluene. However, the films formed via EPD are characterized by significant film thickness gradient from the top to bottom of the

electrode. This non–uniformity in film thickness is shown to be a result of field–induced sedimentation of particles within the dc field. An acid co–polymer, partially sulfonated polystyrene with a ~3 % sulfonation level (SPS3) is also shown to be a promising dispersant for particles in non–polar solvents. Furthermore, CB particles charged by SPS3 could be used for EPD on insulating polymer sheets. This new non–polar approach to EPD will undoubtedly broaden the range of materials to be incorporated as well as the types of substrates on which films can be cast.

Chapter 8. Conclusions and Outlook

8.1 Conclusions

In *Chapter 1* of this thesis, the limitations of nanoparticle layer–by–layer (LbL) assembly to a narrow processing window, aqueous solution and slow processing speeds were presented. It was shown that these limitations could be addressed by using amphiphiles as summarized in the following paragraphs.

Chapter 2 addressed the limitation of aqueous nanoparticle LbL assembly to a narrow processing window. Here, a small amphiphilic molecule, hexylamine (HA), was used to widen the processing window of all–nanoparticle TiO_2/SiO_2 LbL assembled thin films. The growth of TiO_2/SiO_2 films was shown to significantly increase compared to a prior study within the same pH range. The increase in the growth of films was shown to be a result of complete charge inversion of the surface, enabling the adsorption of negatively charged SiO_2 nanoparticles. This new approach of using short amphiphilic molecules to enhance the growth of nanoparticle LbL assembled thin films will be helpful for performing LbL assembly of oppositely charged nanomaterials in a broad pH range.

Chapter 3 demonstrated that LbL assembly of oppositely charged materials can be performed in a non–polar solvent, toluene, thus resolving the limitation of nanoparticle LbL assembly to aqueous solution. A surfactant, AOT, was used to induce negative and positive surface charge on carbon black (CB) and Al_2O_3, respectively such that that LbL

assembly of CB/Al_2O_3 films could be performed on glass slides. *Chapter 4* examined the role of moisture content and surface chemistry (as controlled by thermal treatment) on the charge of model particles, silica in AOT/toluene. Both parameters were found to have a significant effect on the charge of silica particles in AOT/toluene. The results gathered emphasize the importance of carefully controlling the surface chemistry and water content in particle dispersions in order to enhance the reproducibility of electrophoretic mobility measurements in non–polar media. Furthermore, water content and surface chemistry, in addition to the concentration of the charge–inducing agent, provide a new means to control the charging of colloids in non–polar media. Meanwhile, *Chapter 5* linked *Chapters 3* and *4* by showing that relative humidity affects the growth and quality of LbL assembled CB/Al_2O_3 films. In general, for a fixed [AOT] the thickness of CB/Al_2O_3 films was found to increase as relative humidity decreases, thus emphasizing the importance of controlling the water content in particle dispersions used during LbL assembly in non–polar solvents.

Chapter 6 applied the non–polar LbL assembly technique developed in *Chapter 3* to fabricate conductive and photocatalytic MWCNT/TiO_2 films. An advantage of the non–polar LbL assembly approach in the generation of MWCNT/TiO_2 nanocomposites is that oxidation of MWCNTs is not required, thus preserving the electron conducting properties of MWCNTs. The incorporation of MWCNTs in these thin films significantly enhanced the photocatalytic activity of TiO_2 while the physicochemical properties of MWCNT/TiO_2 films could be varied by controlling the assembly condition used (i.e. [AOT]).

Electrophoretic deposition (EPD) of MWCNT/TiO_2 from non–polar solvent was shown in *Chapter 7* to be a viable means of speeding up the assembly of nanocomposites. However, a drawback to the non–polar EPD approach is that non–uniform films are formed due to field–induced sedimentation of particles. EPD in non–polar solvents with partially sulfonated polystyrene (SPS) as a dispersant was shown in *Chapter* 7 to be viable means of forming coatings on insulating surfaces such as polymer sheets.

8.2 Suggestions for Future Research

8.2.1 Fundamental Studies

8.2.1.1 Effect of Selected Amphiphilic Molecule on Widening the LbL Assembly Processing Window

The work covered in *Chapter 2* was based on only one amphiphile, hexylamine. Work done in this group has shown that another amphiphile hexadecyl trimethyl ammonium bromide (HTAB) can screen the surface charge of silica as well as increase the LbL assembly film growth as shown in Figure 8.1 and Figure 8.2 respectively. Therefore, future studies could involve studying the effect of the selected amphiphilic molecules (i.e., the chemical structure of the head group, the length of hydrophobic tail etc.) on the growth behavior and structure (i.e. porosity and composition) of all–nanoparticle LbL assembled thin films.

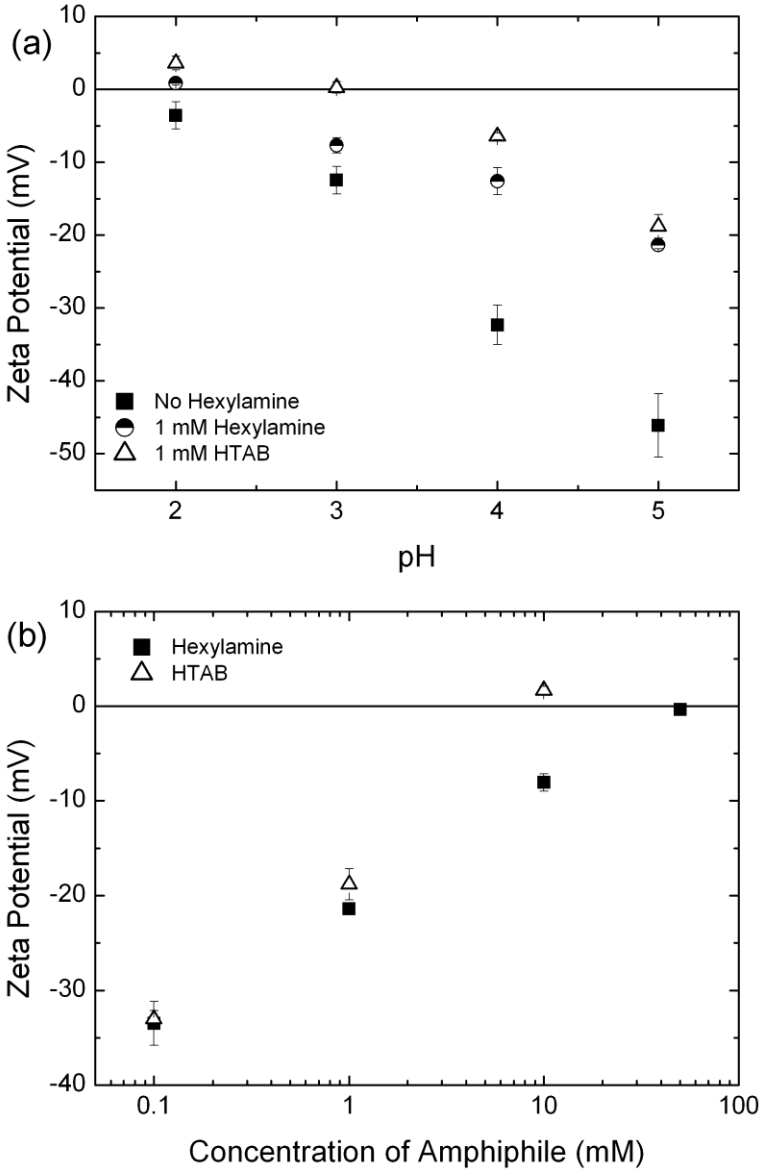

Figure 8.1. Zeta potential of SiO_2 nanoparticles as a function of (a) pH for: no amphiphile added, 1 mM hexylamine and 1 mM HTAB added to SiO_2 nanoparticle dispersions (b) concentration of amphiphile at pH 5.0. Error bars represent standard deviation of three measurements. Data courtesy of Jeanne W. Ho.

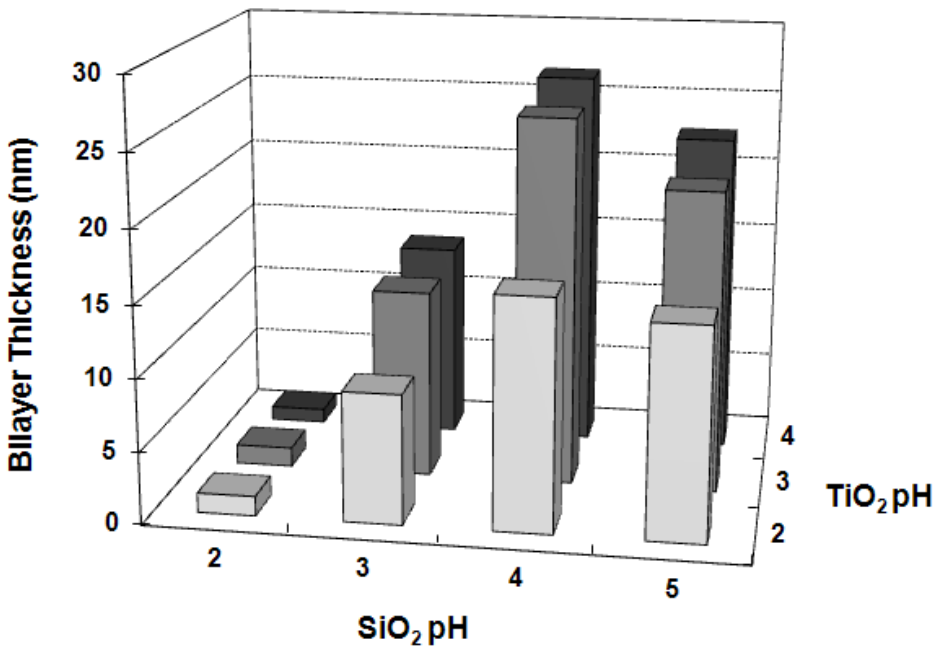

Figure 8.2. pH matrix for TiO_2/SiO_2 LbL thin films with 1 mM HTAB in SiO_2 nanoparticle suspensions. Data courtesy of Jeanne W. Ho.

8.2.1.2 The Nature of Charged Particle Interactions in Non-Polar Solvents

While the experimental results shown in *Chapters 3, 5* and *6* suggest that electrostatic interactions could play a key role during LbL assembly in non–polar solvents, the relative significance of electrostatic interactions compared to other attractive forces such as van der Waals and depletion interactions was not established and warrants further study. Electrostatic interactions, protonation events and hydrogen bonding generally result in strongly exothermic binding, whereas associations giving rise to the release of counterions are entropic in nature. Isothermal Titration Calorimetry (ITC) could be used to study the heteroaggregation of oppositely charged particles in non–polar solvents. The thermodynamic results gathered from ITC measurements will provide new insight into whether heteroaggregation in non–polar solvents is electrostatic (i.e. enthalpic) or

involves release of counterions (i.e. entropic) in nature.[182] This result can then be used to deduce the nature of the attractive forces between charged particles in non–polar solvents during non–polar LbL assembly. Furthermore, the effect of increasing moisture content on the nature of attractive forces between particles would be helpful for a deeper understanding on the findings presented in *Chapter 5*.

To complement ITC measurements, atomic force microscopy (AFM) could be used to determine if particle–surface interactions are electrostatic, and if so, whether they are constant potential (CP), constant charge (CC) or charge regulated (CR) in nature.[183] An advantage of using AFM for these force measurements lies in the fact that the measurements can be performed in liquid phase. Furthermore, both repulsive and attractive forces can be measured with AFM.

8.2.1.3 Acidity in Non–Polar Media

Adsorbed water was found to make the surface of as–received and dehydroxylated silica more basic; however, the exact mechanism of charge reversal warrants further study. Future work could involve using the Hammett indicator method to directly quantify the acid–base properties of as–received and thermally treated silica, and AOT micelles in toluene.[121] Furthermore, the Hammett indicator method can be extended to a broad range of common particles in order to establish a relationship between the Hammett acidity of the particles in non–polar solvent and the acquired charge.

8.2.2 Fabrication of Functional Materials

The simplicity of the non–polar LbL assembly and EPD procedure is advantageous for creating nanocomposite thin films of ceramics and conductive materials. Future studies could involve assembling composite structures composed of carbon and metal oxides since these have been investigated for various applications such as catalysts,[184] adsorbents[185] and conductive nano–powders.[186] Furthermore, other functional materials such as magnetic nanoparticles, quantum dots and conjugated polymers synthesized in non–polar solvents could potentially be charged and incorporated into nanocomposite thin films based on non–polar LbL assembly or EPD. Such possibility will enable these films to be used as electrodes in power generation and storage devices as outlined below.[187-189]

8.2.2.1 Dye–sensitized Solar Cells (DSSCs)

The MWCNT/TiO_2 composite films generated in *Chapter 7* are excellent candidates for dye–sensitized solar cells (DSSCs). Preliminary attempts at using MWCNT/TiO_2 films formed via EPD for DSSCs have not been successful. For example, Figure 8.3 shows that the maximum current produced, known as the short circuit current I_{sc} (the current produced at zero voltage), for MWCNT/TiO_2 films used as DSSC electrodes is much smaller compared to TiO_2 only films used as electrodes. This is attributed to poor adhesion between the film and conducting working electrode and could be resolved by using atomic layer deposition (ALD) of TiO_2 since previous studies in our group have shown that ALD enhances the mechanical properties of LbL assembled films.[26]

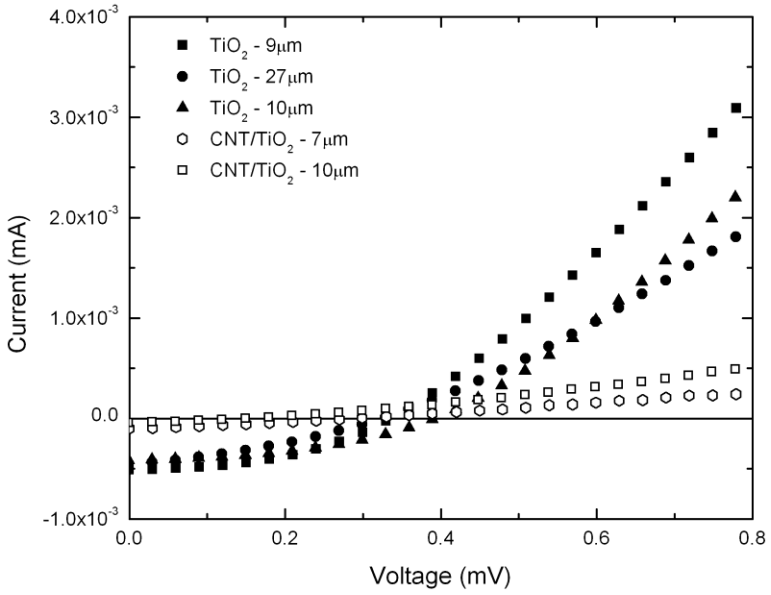

Figure 8.3. Current–voltage (*I–V*) curves for TiO_2 only and CNT/TiO_2 nanocomposite films of varying thicknesses.

In addition, a conformal TiO_2 layer around the MWCNT/TiO_2 composite could facilitate charge transport within the film. Future studies could also utilize in situ polymerization via initiated chemical vapor deposition (iCVD) to deposit polymeric electrolytes within the MWCNT/TiO_2 film.[190] Furthermore, EPD offers an added advantage of control over the layering sequence, e.g. a MWCNT film can be deposited atop TiO_2 layer (Figure 8.4) to improve charge transfer between the TiO_2 film and the working electrode.

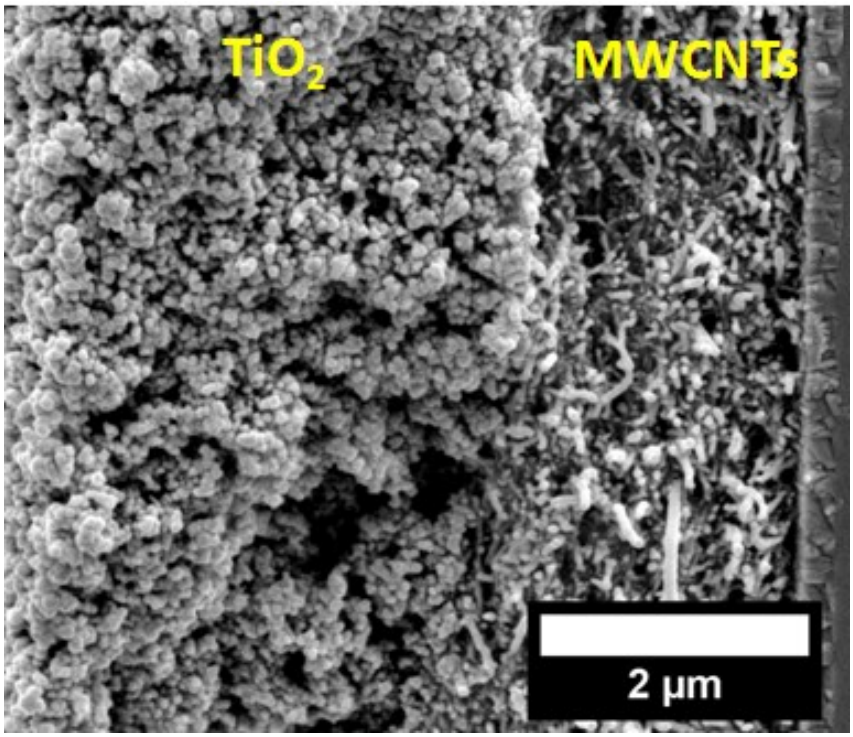

Figure 8.4. SEM image of nanostructured layered TiO_2/MWCNT film fabricated via EPD from AOT/toluene.

8.2.2.2 Photogenerated Water–Splitting

Prior studies have shown that the CNT/TiO_2 films are also excellent for hydrogen generation during photogenerated water–splitting,[191] however preliminary results for the degradation of water/methanol solution with 10 μg platinum as a co–catalyst shows that incorporation of SWCNTs does not increase hydrogen production (Figure 8.5). Future studies could attempt to resolve this discrepancy by varying the SWCNT content within the films, platinum co–catalyst loading, thickness of films as well as type of CNTs used (i.e. SWCNTs vs. MWCNTs).

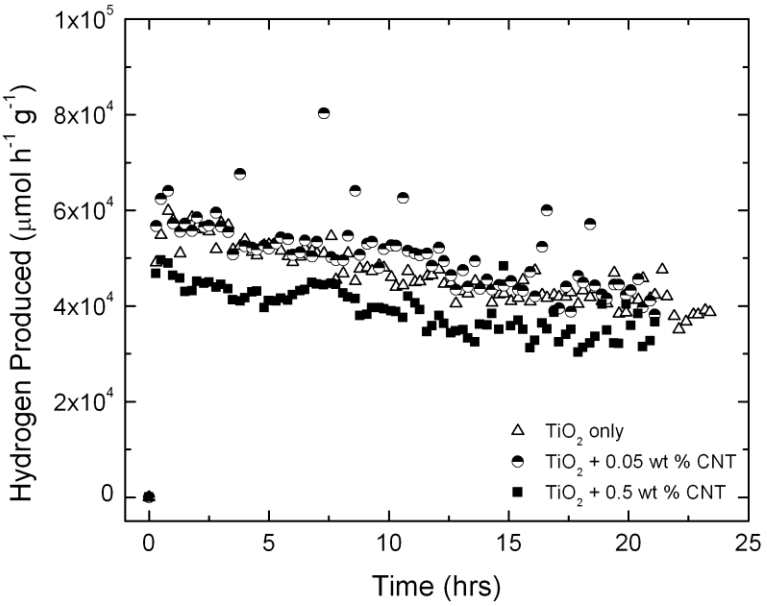

Figure 8.5. Hydrogen produced versus time for TiO_2 only EPD film and SWCNT/TiO_2 films with 0.05 and 0.5 wt % SWCNT content for photogeneration of water/methanol solution with 10 μg platinum co–catalyst.

8.2.2.3 Fuel Cell Membranes

Fuel cells such as proton exchange membrane (PEM) fuel cells often use ion–conducting polymers (ionomers) such as Nafion to transport protons within the cell. Nafion could potentially be substituted with sulfonated polystyrene (SPS), thus the nanostructured CB/SPS films formed via EPD could be excellent candidates as polymer electrolyte membrane (PEM) fuel cell electrodes since these films would have both electron– and proton–conducting properties.

Chapter 9. Bibliography

1. A. Moser, K. Takano, D. T. Margulies, M. Albrecht, Y. Sonobe, Y. Ikeda, S. Sun and E. E. Fullerton, *Journal of Physics D: Applied Physics*, 2002, 35, R157.

2. Y. Jin, Y. Shen and S. Dong, *The Journal of Physical Chemistry B*, 2004, 108, 8142-8147.

3. D. S. Kommireddy, S. M. Sriram, Y. M. Lvov and D. K. Mills, *Biomaterials*, 2006, 27, 4296-4303.

4. P. T. Hammond, *Advanced Materials*, 2004, 16, 1271-1293.

5. K. Ariga, J. P. Hill and Q. Ji, *Physical Chemistry Chemical Physics*, 2007, 9, 2319-2340.

6. G. Decher, *Science*, 1997, 277, 1232-1237.

7. F. Caruso, R. A. Caruso and H. Mohwald, *Science*, 1998, 282, 1111-1114.

8. F. Caruso, E. Donath and H. Mohwald, *J. Phys. Chem. B*, 1998, 102, 2011-2016.

9. E. Donath, G. B. Sukhorukov, F. Caruso, S. A. Davis and H. Mohwald, *Angew. Chem. Int. Ed.*, 1998, 37, 2202-2205.

10. G. B. Sukhorukov, E. Donath, H. Lichtenfeld, E. Knippel, M. Knippel, A. Budde and H. Mohwald, *Colloids Surf., A*, 1998, 137, 253-266.

11. D. Wang, A. L. Rogach and F. Caruso, *Nano Lett*, 2002, 2, 857-861.

12. G. Decher and J. B. Schlenoff, *Multilayer thin films : sequential assembly of nanocomposite materials*, Wiley-VCH, Weinheim, 2003.

13. Y. Wang, A. S. Angelatos and F. Caruso, *Chemistry of Materials*, 2007, 20, 848-858.

14. D. M. Dotzauer, J. H. Dai, L. Sun and M. L. Bruening, *Nano Lett*, 2006, 6, 2268-2272.

15. C. Y. Jiang, S. Markutsya, Y. Pikus and V. V. Tsukruk, *Nat Mater*, 2004, 3, 721-728.

16. A. L. Hillberg and M. Tabrizian, *Biomacromolecules*, 2006, 7, 2742-2750.

17. Y. Lvov, G. Decher and H. Mohwald, *Langmuir*, 1993, 9, 481-486.

18. W. Kong, X. Zhang, M. L. Gao, H. Zhou, W. Li and J. C. Shen, *Macromol. Rapid Commun.*, 1994, 15, 405-409.

19. Y. Lvov, K. Ariga, I. Ichinose and T. Kunitake, *J. Am. Chem. Soc.*, 1995, 117, 6117-6123.

20. J. Lang and M. H. Lin, *J. Phys. Chem. B*, 1999, 103, 11393-11397.

21. H. Hattori, *Adv Mater*, 2001, 13, 51-54.

22. D. Lee, M. F. Rubner and R. E. Cohen, *Nano Lett*, 2006, 6, 2305-2312.

23. S. Huang, X. Cen, H. Peng, S. Guo, W. Wang and T. Liu, *The Journal of Physical Chemistry B*, 2009, 113, 15225-15230.

24. N. Krasteva, I. Besnard, B. Guse, R. E. Bauer, K. Müllen, A. Yasuda and T. Vossmeyer, *Nano Lett*, 2002, 2, 551-555.

25. Z. Y. Tang, N. A. Kotov, S. Magonov and B. Ozturk, *Nature Mater.*, 2003, 2, 413-U418.

26. M. I. Dafinone, G. Feng, T. Brugarolas, K. E. Tettey and D. Lee, *ACS Nano*, 2011, 5, 5078-5087.

27. T. J. Dawidczyk, M. D. Walton, W.-S. Jang and J. C. Grunlan, *Langmuir*, 2008, 24, 8314-8318.

28. J. Hiller, J. D. Mendelsohn and M. F. Rubner, *Nature Mater.*, 2002, 1, 59-63.

29. F. Ã. Cebeci, Z. Wu, L. Zhai, R. E. Cohen and M. F. Rubner, *Langmuir*, 2006, 22, 2856-2862.

30. B.-S. Kim, R. e. C. Smith, Z. Poon and P. T. Hammond, *Langmuir*, 2009, 25, 14086-14092.

31. D. Mertz, C. Vogt, J. Hemmerle, J. Mutterer, V. Ball, J. C. Voegel, P. Schaaf and P. Lavalle, *Nature Mater.*, 2009, 8, 731-735.

32. K. C. Krogman, J. L. Lowery, N. S. Zacharia, G. C. Rutledge and P. T. Hammond, *Nature Mater.*, 2009, 8, 512-518.

33. R. K. Iler, *Journal of Colloid and Interface Science*, 1966, 21, 569-594.

34. G. Decher and J.-D. Hong, *Makromolekulare Chemie. Macromolecular Symposia*, 1991, 46, 321-327.

35. G. Decher and J. D. Hong, *Berichte der Bunsengesellschaft für physikalische Chemie*, 1991, 95, 1430-1434.

36. G. Decher, J. D. Hong and J. Schmitt, *Thin Solid Films*, 1992, 210â€“211, Part 2, 831-835.

37. G. Laufer, F. Carosio, R. Martinez, G. Camino and J. C. Grunlan, *Journal of Colloid and Interface Science*, 356, 69-77.

38. J. Kim, S. W. Lee, P. T. Hammond and Y. Shao-Horn, *Chem. Mat.*, 2009, 21, 2993-3001.

39. S. W. Lee, B. S. Kim, S. Chen, Y. Shao-Horn and P. T. Hammond, *J. Am. Chem. Soc.*, 2009, 131, 671-679.

40. D. Lee, Z. Gemici, M. F. Rubner and R. E. Cohen, *Langmuir*, 2007, 23, 8833-8837.

41. S. Beyer, W. C. Mak and D. Trau, *Langmuir*, 2007, 23, 8827-8832.

42. V. K. Kamineni, Y. M. Lvov and T. A. Dobbins, *Langmuir*, 2007, 23, 7423-7427.

43. X. L. Tuo, D. Chen, H. Cheng and X. G. Wang, *Polym. Bull.*, 2005, 54, 427-433.

44. G. S. Roberts, R. Sanchez, R. Kemp, T. Wood and P. Bartlett, *Langmuir*, 2008, 24, 6530-6541.

45. T. Hyeon, *Chem. Commun.*, 2003, 927-934.

46. C. B. Murray, C. R. Kagan and M. G. Bawendi, *Annu. Rev. Mater. Sci.*, 2000, 30, 545-610.

47. J. Roncali, *Chem. Rev.*, 1992, 92, 711-738.

48. Y. Yin and A. P. Alivisatos, *Nature*, 2005, 437, 664-670.

49. S. Hirsjarvi, L. Peltonen and J. Hirvonen, *Colloids and Surfaces B-Biointerfaces*, 2006, 49, 93-99.

50. W. D. Mulhearn, D. D. Kim, Y. L. Gu and D. Lee, *Soft Matter*, 2012, 8, 10419-10427.

51. M. Michel, V. Toniazzo, D. Ruch and V. Ball, *ISRN Materials Science*, 2012, 13.

52. M. Gargaud and R. Amils, *Encyclopedia of astrobiology*, Springer, Berlin.

53. C. Peng, Y. S. Thio and R. A. Gerhardt, *J. Phys. Chem. C* 2010, 114, 9685-9692.

54. J. W. Ostrander, A. A. Mamedov and N. A. Kotov, *J. Am. Chem. Soc.*, 2001, 123, 1101-1110.

55. U. T. Gonzenbach, A. R. Studart, E. Tervoort and L. J. Gauckler, *Angew. Chem., Int. Ed.*, 2006, 45, 3526-3530.

56. I. Akartuna, A. R. Studart, E. Tervoort, U. T. Gonzenbach and L. J. Gauckler, *Langmuir*, 2008, 24, 7161-7168.

57. U. T. Gonzenbach, A. R. Studart, E. Tervoort and L. J. Gauckler, *J. Am. Ceram. Soc.*, 2007, 90, 16-22.

58. D. Lee, D. Omolade, R. E. Cohen and M. F. Rubner, *Chem. Mater.*, 2007, 19, 1427-1433.

59. D. C. Patel and W. I. Higuchi, *J. Colloid Interface Sci.*, 1980, 74, 211-219.

60. S. Mori and H. Okamoto, *J. Flotation Res. Assoc. Jpn.* , 1980, 27, 117-126.

61. A. Kampes and B. Tieke, *Mater. Sci. Eng., C* 1999, 8-9, 195-204.

62. M. Watanabe, S. Kawaguchi and K. Nagai, *Colloid Polym. Sci.*, 2006, 285, 305-314.

63. J. Depasse, *J. Colloid Interface Sci.*, 1999, 220, 174-176.

64. B. P. Binks and S. O. Lumsdon, *Phys. Chem. Chem. Phys.* , 1999, 1, 3007-3016.

65. R. K. Iler, *Chemistry of Silica - Solubility, Polymerization, Colloid and Surface Properties and Biochemistry*, John Wiley & Sons, New York, 1979.

66. M. R. Böhmer, E. A. van der Zeeuw and G. J. M. Koper, *J. Colloid Interface Sci.*, 1998, 197, 242-250.

67. M. Semmler, E. K. Mann, J. RicÌŒka and M. Borkovec, *Langmuir*, 1998, 14, 5127-5132.

68. C. A. Johnson and A. M. Lenhoff, *J. Colloid Interface Sci.*, 1996, 179, 587-599.

69. M. F. Hsu, E. R. Dufresne and D. A. Weitz, *Langmuir*, 2005, 21, 4881-4887.

70. R. I. Keir, Suparno and J. C. Thomas, *Langmuir*, 2002, 18, 1463-1465.

71. P. G. Smith, M. N. Patel, J. Kim, T. E. Milner and K. P. Johnston, *J. Phys. Chem. C*, 2007, 111, 840-848.

72. S. K. Sainis, V. Germain, C. O. Mejean and E. R. Dufresne, *Langmuir*, 2008, 24, 1160-1164.

73. S. K. Sainis, J. W. Merrill and E. R. Dufresne, *Langmuir*, 2008, 24, 13334-13347.

74. I. D. Morrison, *Colloid Surface A*, 1993, 71, 1-37.

75. S. Poovarodom and J. C. Berg, *J. Colloid Interface Sci.*, 2010, 346, 370-377.

76. G. N. Smith and J. Eastoe, *Physical Chemistry Chemical Physics*, 2013, 15, 424-439.

77. A. Kitahara, S. Karasawa and H. Yamada, *J. Colloid Interface Sci.*, 1967, 25, 490-495.

78. R. Kemp, R. Sanchez, K. J. Mutch and P. Bartlett, *Langmuir*.

79. A. M. Islam, B. Z. Chowdhry and M. J. Snowden, *Adv. Colloid Interface Sci.*, 1995, 62, 109-136.

80. V. R. Damerell and R. Mattson, *J. Phys. Chem.*, 1944, 48, 134-141.

81. G. A. van Ewijk and A. P. Philipse, *Langmuir*, 2001, 17, 7204-7209.

82. S. Poovarodom, S. Poovarodom and J. C. Berg, *Journal of Colloid and Interface Science*, 2010, 351, 415-420.

83. M. Gacek, G. Brooks and J. C. Berg, *Langmuir*, 2012, 28, 3032-3036.

84. A. S. Dimitrov and K. Nagayama, *Langmuir*, 1996, 12, 1303-1311.

85. J. W. Ostrander, A. A. Mamedov and N. A. Kotov, *J. Am. Chem. Soc.*, 2001, 123, 1101-1110.

86. S. S. Shiratori and M. F. Rubner, *Macromolecules*, 2000, 33, 4213-4219.

87. P. M. Nguyen, N. S. Zacharia, E. Verploegen and P. T. Hammond, *Chem. Mater.*, 2007, 19, 5524-5530.

88. M. Chipara, K. Lozano, A. Hernandez and M. Chipara, *Polym. Degrad. Stab.*, 2008, 93, 871-876.

89. R. L. Menchavez, M. Fuji and M. Takahashi, *Adv. Mater.*, 2008, 20, 2345-+.

90. J. P. Rives and B. I. Lee, *Colloids and Surfaces*, 1991, 56, 45-58.

91. C. A. Malbrel and P. Somasundaran, *Langmuir*, 1992, 8, 1285-1290.

92. M. Gacek, D. Bergsman, E. Michor and J. C. Berg, *Langmuir*, 2012, 28, 11633–11638.

93. W. Stöber, A. Fink and E. Bohn, *Journal of Colloid and Interface Science*, 1968, 26, 62-69.

94. P. Van Der Voort, I. Gillis-D'Hamers and E. F. Vansant, *Journal of the Chemical Society, Faraday Transactions*, 1990, 86, 3751-3755.

95. S. Ek, A. Root, M. Peussa and L. Niinistö, *Thermochim. Acta*, 2001, 379, 201-212.

96. R. Mueller, H. K. Kammler, K. Wegner and S. E. Pratsinis, *Langmuir*, 2002, 19, 160-165.

97. J.-P. Gallas, J.-M. Goupil, A. Vimont, J.-C. Lavalley, B. Gil, J.-P. Gilson and O. Miserque, *Langmuir*, 2009, 25, 5825-5834.

98. L. Greenspan, *Journal of Research of the National Bureau of Standards Section a-Physics and Chemistry*, 1977, 81, 89-96.

99. L. T. Zhuravlev, *Colloids and Surfaces A: Physicochemical and Engineering Aspects*, 2000, 173, 1-38.

100. R. K. Iler, *The chemistry of silica : solubility, polymerization, colloid and surface properties, and biochemistry*, Wiley, New York, 1979.

101. J. Nawrocki, *Journal of Chromatography A*, 1997, 779, 29-71.

102. S. Ong, X. Zhao and K. B. Eisenthal, *Chemical Physics Letters*, 1992, 191, 327-335.

103. Y. Dong, S. V. Pappu and Z. Xu, *Analytical Chemistry*, 1998, 70, 4730-4735.

104. C. D. Lorenz, P. S. Crozier, J. A. Anderson and A. Travesset, *The Journal of Physical Chemistry C*, 2008, 112, 10222-10232.

105. H. Zhang, D. R. Dunphy, X. Jiang, H. Meng, B. Sun, D. Tarn, M. Xue, X. Wang, S. Lin, Z. Ji, R. Li, F. L. Garcia, J. Yang, M. L. Kirk, T. Xia, J. I. Zink, A. E. Nel and C. J. Brinker, *Journal of the American Chemical Society*, 2012, 134, 15790–15804.

106. M. Fowkes F, H. Jinnai, A. Mostafa M, W. Anderson F and J. Moore R, in *Colloids and Surfaces in Reprographic Technology*, American Chemical Society, 1982, pp. 307-324.

107. R. J. Pugh, T. Matsunaga and F. M. Fowkes, *Colloids and Surfaces*, 1983, 7, 183-207.

108. E. J. Stancik and G. G. Fuller, *Langmuir*, 2004, 20, 4805-4808.

109. S. Reynaert, P. Moldenaers and J. Vermant, *Langmuir*, 2006, 22, 4936-4945.

110. P. G. Smith, M. N. Patel, J. Kim, T. E. Milner and K. P. Johnston, *The Journal of Physical Chemistry C*, 2006, 111, 840-848.

111. M. N. Patel, P. G. Smith Jr, J. Kim, T. E. Milner and K. P. Johnston, *Journal of Colloid and Interface Science*, 2010, 345, 194-199.

112. R. Kemp, R. Sanchez, K. J. Mutch and P. Bartlett, *Langmuir*, 2010, 26, 6967-6976.

113. M. M. Gacek and J. C. Berg, *Langmuir*, 2012, 28, 17841-17845.

114. Q. Guo, J. Lee, V. Singh and S. H. Behrens, *J. Colloid Interface Sci.*, 2013, 392, 83-89.

115. Q. Guo, V. Singh and S. H. Behrens, *Langmuir*, 2009, 26, 3203-3207.

116. M. Zulauf and H. F. Eicke, *The Journal of Physical Chemistry*, 1979, 83, 480-486.

117. A. Kitahara, M. Amano, S. Kawasaki and K. Kon-no, *Colloid & Polymer Science*, 1977, 255, 1118-1121.

118. C. E. Espinosa, Q. Guo, V. Singh and S. H. Behrens, *Langmuir*, 2010, 26, 16941-16948.

119. M. E. Parent, J. Yang, Y. Jeon, M. F. Toney, Z.-L. Zhou and D. Henze, *Langmuir*, 2011, 27, 11845-11851.

120. F. M. Fowkes, D. N. L. McGown, G. D. Parfitt, L. A. Romo, A. Breeuwsma, B. H. Bijsterbosch, E. Matijevic, R. E. Day, F. J. Micale, E. J. W. Verwey and D. W. J. Osmond, *Discussions of the Faraday Society*, 1966, 42, 243-247.

121. H. A. Benesi, B. H. C. Winquist, H. P. D.D. Eley and B. W. Paul, in *Advances in Catalysis*, Academic Press, 1979, pp. 97-182.

122. L. T. Zhuravlev, *Langmuir*, 1987, 3, 316-318.

123. K. E. Tettey, M. Q. Yee and D. Lee, *Langmuir*, 2010, 26, 9974-9980.

124. K. Tettey and D. Lee, *Soft Matter*.

125. P. Podsiadlo, S. Paternel, J.-M. Rouillard, Z. Zhang, J. Lee, J.-W. Lee, E. Gulari and N. A. Kotov, *Langmuir*, 2005, 21, 11915-11921.

126. A. Heller, *Acc. Chem. Res.*, 1995, 28, 503-508.

127. M. R. Hoffmann, S. T. Martin, W. Y. Choi and D. W. Bahnemann, *Chem. Rev.*, 1995, 95, 69-96.

128. J. C. Ireland, P. Klostermann, E. W. Rice and R. M. Clark, *Appl. Environ. Microbiol.*, 1993, 59, 1668-1670.

129. K. Sunada, Y. Kikuchi, K. Hashimoto and A. Fujishima, *Environ. Sci. Technol.*, 1998, 32, 726-728.

130. M. A. Fox and M. T. Dulay, *Chem. Rev.*, 1993, 93, 341-357.

131. K. Woan, G. Pyrgiotakis and W. Sigmund, *Adv. Mater.*, 2009, 21, 2233-2239.

132. S. Muduli, W. Lee, V. Dhas, S. Mujawar, M. Dubey, K. Vijayamohanan, S. H. Han and S. Ogale, *ACS Appl. Mater. Interfaces*, 2009, 1, 2030-2035.

133. A. Kongkanand, R. M. Dominguez and P. V. Kamat, *Nano Lett.*, 2007, 7, 676-680.

134. K. Byrappa, A. S. Dayananda, C. P. Sajan, B. Basavalingu, M. B. Shayan, K. Soga and M. Yoshimura, *J. Mater. Sci.*, 2008, 43, 2348-2355.

135. Y. S. Luo, J. P. Liu, X. H. Xia, X. Q. Li, T. Fang, S. Q. Li, Q. F. Ren, J. L. Li and Z. Jia, *Mater. Lett.*, 2007, 61, 2467-2472.

136. Y. C. Wu, X. L. Liu, M. Ye, T. Xie and X. M. Huang, *Acta Phys.-Chim. Sin.*, 2008, 24, 97-102.

137. L. Chen, B. L. Zhang, M. Z. Qu and Z. L. Yu, *Powder Technol.*, 2005, 154, 70-72.

138. L. C. Jiang and W. D. Zhang, *Electroanalysis*, 2009, 21, 988-993.

139. S. Aryal, C. K. Kim, K.-W. Kim, M. S. Khil and H. Y. Kim, *Mater. Sci. Eng., C*, 2008, 28, 75-79.

140. A. Hirsch, *Angew. Chem., Int. Ed.*, 2002, 41, 1853-1859.

141. T. H. Kim and B. H. Sohn, *Appl. Surf. Sci.*, 2002, 201, 109-114.

142. Y. Lvov, K. Ariga, M. Onda, I. Ichinose and T. Kunitake, *Langmuir*, 1997, 13, 6195-6203.

143. K. C. Krogman, J. L. Lowery, N. S. Zacharia, G. C. Rutledge and P. T. Hammond, *Nat. Mater.*, 2009, 8, 512-518.

144. J. A. Lee, K. C. Krogman, M. L. Ma, R. M. Hill, P. T. Hammond and G. C. Rutledge, *Adv. Mater.*, 2009, 21, 1252- 1256.

145. K. C. Krogman, N. S. Zacharia, D. M. Grillo and P. T. Hammond, *Chem. Mater.*, 2008, 20, 1924-1930.

146. A. A. Mamedov, N. A. Kotov, M. Prato, D. M. Guldi, J. P. Wicksted and A. Hirsch, *Nat. Mater.*, 2002, 1, 190-194.

147. J. H. Rouse and P. T. Lillehei, *Nano Lett.*, 2003, 3, 59-62.

148. M. A. Correa-Duarte, A. Kosiorek, W. Kandulski, M. Giersig and L. M. Liz-Marzan, *Chem. Mater.*, 2005, 17, 3268-3272.

149. C. E. Hamilton, J. R. Lomeda, Z. Sun, J. M. Tour and A. R. Barron, *Nano Lett.*, 2009, 9, 3460-3462.

150. Y. T. Park, A. Y. Ham and J. C. Grunlan, *J. Phys. Chem. C*, 2010, 114, 6325-6333.

151. H. Paloniemi, T. Ääritalo, T. Laiho, H. Liuke, N. Kocharova, K. Haapakka, F. Terzi, R. Seeber and J. Lukkari, *J. Phys. Chem. B*, 2005, 109, 8634-8642.

152. H. Paloniemi, M. Lukkarinen, T. Ääritalo, S. Areva, J. Leiro, M. Heinonen, K. Haapakka and J. Lukkari, *Langmuir*, 2005, 22, 74-83.

153. M. K. Gheith, V. A. Sinani, J. P. Wicksted, R. L. Matts and N. A. Kotov, *Adv. Mater.*, 2005, 17, 2663-2670.

154. P. C. Hiemenz and R. Rajagopalan, *Principles of colloid and surface chemistry*, Marcel Dekker, New York, 1997.

155. G. Decher, J. D. Hong and J. Schmitt, *Thin Solid Films*, 1992, 210, 831-835.

156. E. Frackowiak and F. Beguin, *Carbon*, 2001, 39, 937-950.

157. E. Frackowiak and F. Beguin, *Carbon*, 2002, 40, 1775-1787.

158. Y. Yu, J. C. Yu, J. G. Yu, Y. C. Kwok, Y. K. Che, J. C. Zhao, L. Ding, W. K. Ge and P. K. Wong, *Appl. Catal., A*, 2005, 289, 186-196.

159. E. Kharlampieva, V. Kozlovskaya, J. Chan, J. F. Ankner and V. V. Tsukruk, *Langmuir*, 2009, 25, 14017-14024.

160. P. Sarkar and P. S. Nicholson, *J. Am. Ceram. Soc.*, 1996, 79, 1987-2002.

161. O. O. Van der Biest and L. J. Vandeperre, *Annual Review of Materials Science*, 1999, 29, 327-352.

162. L. Besra and M. Liu, *Prog. Mater. Sci.*, 2007, 52, 1-61.

163. J. H. Dickerson and A. R. Boccaccini, *Electrophoretic deposition of nanomaterials*, Springer Science+Business Media, New York.

164. A. J. Krejci, I. Gonzalo-Juan and J. H. Dickerson, *ACS Applied Materials & Interfaces*, 2011, 3, 3611-3615.

165. I. Gonzalo-Juan, A. J. Krejci and J. H. Dickerson, *Langmuir*, 2012, 28, 5295-5301.

166. S. V. Mahajan and J. H. Dickerson, *Nanotechnology*, 2011, 21, 145704.

167. N. C. Zhou, C. Xu, W. R. Burghardt, R. J. Composto and K. I. Winey, *Macromolecules*, 2006, 39, 2373-2379.

168. B. J. C. Thomas, A. R. Boccaccini and M. S. P. Shaffer, *J. Am. Ceram. Soc.*, 2005, 88, 980-982.

169. A. Fraczek-Szczypta, E. Dlugon, A. Weselucha-Birczynska, M. Nocun and M. Blazewicz, *Journal of Molecular Structure*, 2013, 1040, 238-245.

170. J. T. Padding and A. A. Louis, *Phys. Rev. E*, 2008, 77, 11.

171. H. Block and J. P. Kelly, *Journal of Physics D: Applied Physics*, 1988, 21, 1661.

172. A. P. Gast and C. F. Zukoski, *Adv. Colloid Interface Sci.*, 1989, 30, 153-202.

173. T. Vissers, A. Imhof, F. l. Carrique, Ã. n. V. Delgado and A. van Blaaderen, *J. Colloid Interface Sci.*, 2011, 361, 443-455.

174. Y. Kim and D. Klingenberg, *Korean Journal of Chemical Engineering*, 1997, 14, 30-36.

175. Y. Kim and D. Klingenberg, *Korean Journal of Chemical Engineering*, 1997, 14, 23-29.

176. H. See and M. Doi, *J. Phys. Soc. Jpn.*, 1991, 60, 2778-2782.

177. A. P. Philipse, *Current Opinion in Colloid & Interface Science*, 1997, 2, 200-206.

178. M. Gonzalez-Cuenca, P. M. Biesheuvel and H. Verweij, *Aiche Journal*, 2000, 46, 626-631.

179. L. Besra, C. Compson and M. Liu, *Journal of Power Sources*, 2007, 173, 130-136.

180. S. A. Hasan, D. W. Kavich and J. H. Dickerson, *Chemical Communications*, 2009, 0, 3723-3725.

181. H.-W. Chen, C.-P. Liang, H.-S. Huang, J.-G. Chen, R. Vittal, C.-Y. Lin, K. C. W. Wu and K.-C. Ho, *Chemical Communications*, 2011, 47, 8346-8348.

182. J. Ladbury and M. Doyle, *Biocalorimetry 2: applications of calorimetry in the biological sciences*, Wiley, 2004.

183. I. Popa, P. Sinha, M. Finessi, P. Maroni, G. Papastavrou and M. Borkovec, *Phys. Rev. Lett.*, 2010, 104, 4.

184. E. Lopez-Salinas, J. G. Espinosa, J. G. Hernandez-Cortez, J. Sanchez-Valente and J. Nagira, *Catal. Today*, 2005, 109, 69-75.

185. F. Villieras, R. Leboda, B. Charmas, F. Bardot, G. Gerard and W. Rudzinski, *Carbon*, 1998, 36, 1501-1510.

186. F. Inam, H. X. Yan, D. D. Jayaseelan, T. Peijs and M. Reece, *J. Eur. Ceram. Soc.*, 2010, 30, 153-157.

187. M. Michel, A. Taylor, R. Sekol, P. Podsiadlo, P. Ho, N. Kotov and L. Thompson, *Adv. Mater.*, 2007, 19, 3859-3864.

188. A. S. Arico, P. Bruce, B. Scrosati, J. M. Tarascon and W. Van Schalkwijk, *Nature Mater.*, 2005, 4, 366-377.

189. P. G. Bruce, B. Scrosati and J. M. Tarascon, *Angewandte Chemie-International Edition*, 2008, 47, 2930-2946.

190. S. Nejati and K. K. S. Lau, *Nano Letters*, 2011, 11, 419-423.

191. K. Dai, T. Peng, D. Ke and B. Wei, *Nanotechnology*, 2009, 20, 125603.